

NERVA IRRADIATION PROGRAM

**Mapping of the Radiation Field
Within the In-Pile Tube
of the Aerospace Systems Test Reactor**

Prepared for
Space Nuclear Properties
of the
Aeronautics and Space
Administration
Cleveland, Ohio

NUCLEAR AEROSPACE RESEARCH FACILITY

TECHNICAL DOCUMENT CENTER
Nuclear Rocket Operations

DOC. NO. *1482*

AGCS 0120-48

FZK-343
15 November 1967

NUCLEAR AEROSPACE RESEARCH FACILITY

NERVA IRRADIATION PROGRAM

Mapping of the Radiation Field
Within the In-Pile Tube
of the Aerospace Systems Test Reactor

J. H. Lewis
R. E. Bullock
J. S. Kunselman

Prepared for
Space Nuclear Propulsion Office
of the
National Aeronautics and Space Administration
Cleveland, Ohio

Contract No. AF 29(601)-7077

Supplement 10

GENERAL DYNAMICS
Fort Worth Division

NOTICE
This report was prepared as an account of work sponsored by the Federal Government in the United States and is the property of the Federal Government. It is loaned to your organization and is not to be distributed outside your organization. It is to be returned to the Federal Government upon request. It is not to be reproduced, stored in a retrieval system, or transmitted, in any form or by any means, electronic, mechanical, photocopying, recording, or by any information storage and retrieval system, without prior written permission from the Federal Government.

DISSEMINATION STATEMENT: UNCLASSIFIED

FOREWORD

The work described in this document was performed at the Nuclear Aerospace Research Facility (NARF) of the Fort Worth Division of General Dynamics for the Space Nuclear Propulsion Office, Cleveland, Ohio (SNPO-C) under Statement of Work No. 6 (Attachment J), Contract AF29(601)-7077, SA No. 10.

This test was performed to support the Transducer Irradiation Experiment sponsored by the Aerojet-General Corporation, Sacramento, California. The transducer experiment was one of a series of NERVA irradiation tests performed at NARF and was the first to be conducted in the In-Pile Tube of the Aerospace Systems Test Reactor. The results of the transducer test will be reported in GD Fort Worth Division Report FZK-344.

The authors wish to acknowledge the contribution of W. E. Dungan for the computation of the neutron spectrum.

SUMMARY

The core of the 10-MW Aerospace Systems Test Reactor has been modified to provide an in-core irradiation facility. This facility consists of a tube with an inside diameter of 3.75 in. This in-pile tube occupies a former fuel-element position near the center of the core and extends completely through the core. It is plugged at one end and extends through the forward pressure plate of the reactor. The tube is completely sealed so as to provide a dry irradiation volume in the high-flux region within the reactor core.

To provide data on the radiation field within the in-pile tube for use in planning radiation-effects experiments, an extensive mapping of the neutron and gamma-ray fields has been conducted. The primary effort was the axial mapping of the heating rate by means of a pedestal-type aluminum calorimeter. Additional data on the gamma field were obtained by means of a 4-cc ion chamber and gamma dosimeters (cobalt glass and thermoluminescent). Neutron fluxes were measured with foils of various types.

Data were obtained with the calorimeter at several reactor power levels ranging from 0.273 to 6.78 MW; corresponding differential temperatures measured across the stem of the calorimeter ranged from 4.13 to 93.33°F. A set of profile measurements was obtained at 1.89 MW by positioning the calorimeter (by means of a traversing mechanism) at various locations over the length (24 in.) of the core. The maximum measured heating rate in the aluminum calorimeter was found to be 0.265 W/g Al-MW at a point approximately 2 in. above the center of the core. The corresponding computed heating rate in carbon is 0.283 W/g C-MW. The estimated uncertainty is 9.6% at the 95% confidence level.

The ion chamber was used to measure the gamma dose rate at a number of power levels from zero to 165 kW; an accurate profile was obtained by traversing the detector through the core several times at each power level. After making a small correction for the neutron contribution, the maximum dose rate in the in-pile tube (2 in. above the center of the core) was found to be 1.10×10^6 R/h-MW, with an estimated uncertainty of 11.3% at the

95% confidence level. Conversion of the heating rates measured with the calorimeter to dose rates resulted in values in close agreement with the ion-chamber data.

Foils and/or gamma dosimeters were irradiated at power levels of zero, 44.5 W, 455 W, and 1.65 kW (3 irradiations). The gamma dose rates obtained from cobalt glass are in reasonable agreement with the ion-chamber values. Thermoluminescent dosimeters - which were provided, read-out, and the data analyzed by Aercjet-General Corporation - gave results somewhat higher than the other methods.

The maximum fast-neutron flux measured with sulfur pellets is 1.36×10^{12} n/cm²-sec-MW; conversion to flux above 1 MeV gives 3.8×10^{12} n/cm²-sec-MW. The peak thermal-neutron flux is 5.5×10^{12} n/cm²-sec-MW.

An extensive theoretical development for the calorimeter is presented, along with an analysis of the heat losses and the calibration of the calorimeter with an electric heater. The experimental apparatus and procedures are detailed.

TABLE OF CONTENTS

	<u>Page</u>
FOREWORD	iii
SUMMARY	v
LIST OF FIGURES	xi
LIST OF TABLES	xiii
1. INTRODUCTION	1
2. METHODS	3
2.1 Calorimeter	3
2.1.1 Theory	3
2.1.2 Corrections to the Theory	7
2.1.3 Calibration	15
2.2 Ion Chamber	22
2.2.1 Characteristics	22
2.2.2 Neutron Sensitivity	23
2.2.3 Calibration	23
2.3 Dosimeters	24
2.3.1 Cobalt Glass	24
2.3.2 Thermoluminescent	24
2.4 Foils	25
2.4.1 Types	25
2.4.2 Calibration	26
3. EXPERIMENTAL EQUIPMENT	31
3.1 Aerospace Systems Test Reactor	31
3.2 ASTR In-Pile Tube	31
3.3 Calorimeter	34

TABLE OF CONTENTS (cont'd)

	<u>Page</u>
3.4 Ion Chamber	37
3.5 Traversing Mechanism	41
3.6 Foil and Dosimeter Fixtures	41
4. IRRADIATION PROCEDURE	47
4.1 Foils and Dosimeters	47
4.2 Ion Chamber	47
4.3 Calorimeter	48
5. RESULTS	51
5.1 Calorimeter	51
5.1.1 Nuclear Heating Rate	51
5.1.2 Gamma Dose Rate	59
5.1.3 Error Analysis	62
5.2 Ion Chamber	64
5.2.1 Gamma Dose Rate	64
5.2.2 Gamma Background	68
5.2.3 After-Shutdown Dose Rate	68
5.2.4 Error Analysis	71
5.3 Gamma Dosimeters	72
5.3.1 Cobalt Glass	72
5.3.2 Thermoluminescent Dosimeters	75
5.4 Neutron-Detecting Foils	75
5.4.1 Fast-Neutron Flux	75
5.4.2 Thermal-Neutron Flux	75
5.4.3 Neutron Spectrum	82

TABLE OF CONTENTS (cont'd)

	<u>Page</u>
APPENDIX A - Calorimeter Measurements of Nuclear Heating Rates	89
APPENDIX B - Least-Squares Curve Fits to Data	97
APPENDIX C - Ion-Chamber Data	103
REFERENCES	109
BIBLIOGRAPHY	110
DISTRIBUTION	111

BLANK PAGE

LIST OF FIGURES

<u>Figure</u>		<u>Page</u>
1	Pedestal-Type Calcrimeter	4
2	Sketch of Calcrimeter in Calibration Configuration	15
3	Measured and Calculated Calcrimeter Calibration Curves	17
4	In-Pile Tube Inserted in Reactor Grid Plate	32
5	In-Pile Tube Extending Through Forward Pressure Plate	33
6	Calorimeter with Vacuum Dome Used in Irradiation	35
7	Sketch Showing Details of Calcrimeter	36
8	Chromel-Alumel Thermocouple Error Curve	38
9	Calorimeter with Calibration Heater Installed	39
10	Calcrimeter Calibration Setup	40
11	Ion Chamber in Irradiation Configuration	42
12	Sketch of Foil and Dosimeter Fixture	43
13	Sketch of Perturbation Fixture	45
14	Sketch Showing Orientation of Foil and Dosimeter Fixtures in the Reactor Core	46
15	Heating Rate in Aluminum as a Function of Reactor Power Level	55
16	Heating-Rate Profile Through the ASTR Core	57
17	Gamma-Dose-Rate Profile as Determined from Calcrimeter Data	61

LIST OF FIGURES (cont'd)

<u>Figure</u>		<u>Page</u>
18	Final Gamma-Dose-Rate Profile for the ASTR Core	66
19	Background Gamma Dose Rate in the In-Pile Tube	69
20	After-Shutdown Gamma Dose Rate in the In-Pile Tube	70
21	Gamma-Dose-Rate Profile as Determined from Cobalt-Glass Dosimeters	74
22	Gamma-Dose-Rate Profile as Determined from Average AGC Mapping Data	77
23	Fast-Neutron-Flux Profile as Determined from Sulfur-Pellet Data	79
24	Thermal-Neutron-Flux Profile as Determined from Copper-Foil Data	81
25	Thermal-Neutron-Flux Profile as Determined from the Average AGC Mapping Data	83
26	Approximate Neutron Spectrum in the ASTR In-Pile Tube	84
A-1	Equivalent Heat Probes at Steady State	95

LIST OF TABLES

<u>Table</u>		<u>Page</u>
1	Estimated Radiation Heat Losses from the Probe at Various Power Levels	9
2	Heat Losses in Initial Calibration of the Calorimeter	19
3	Heat Losses in Final Calibration of the Calorimeter	21
4	Summary of Data for Neutron Detectors	27
5	Foil Calibration Method	29
6	Maximum External Calorimeter Temperatures	49
7	Calorimeter ΔT Data	52
8	Nuclear Heating Rates in Aluminum	53
9	Nuclear Heating Rates in Carbon	58
10	Gamma Dose Rates Computed from Calorimeter Data	60
11	Gamma Dose Rates Measured with Ion Chamber	65
12	Gamma Dose and Dose Rate from Cobalt-Glass Dosimeters	73
13	AGC Thermoluminescent-Dosimeter Data	76
14	Neutron Flux from Sulfur and Aluminum Detectors	78
15	Copper-Foil Saturated Activities	80
16	Resonance-Neutron Spectral Functions	86
B-1	Least-Squares Coefficients for Heating and Dose Rates in the ASTR	100

LIST OF TABLES (cont'd)

<u>Table</u>		<u>Page</u>
B-2	Dose Rates Through the ASTR Core	101
C-1	Gamma Dose Rates Measured with the Ion Chamber, Top-to-Bottom Traverses	106
C-2	Gamma Dose Rates Measured with the Ion Chamber, Bottom-to-Top Traverses	107

1. INTRODUCTION

The core of the Aerospace Systems Test Reactor (ASTR) has been modified by the installation of an in-pile-tube irradiation facility. This tube occupies a former fuel-element position near the center of the core and extends completely through the reactor core, terminating outside the reactor pressure vessel. Access to the tube is easily gained, either by use of a clamp-on extension tube or by removal and re-insertion of the in-pile tube in a simple mechanical operation.

The ASTR is a 10-MW, water-moderated reactor located at the Nuclear Aerospace Research Facility operated by the Fort Worth Division of General Dynamics. The ASTR is used in radiation-effects and shielding experiments in support of various government-sponsored programs. One of these experiments involved the irradiation of pressure transducers of the type used on the XE-1 nozzle of the NERVA engine (Ref. 1); the in-pile tube was used for this test.

The successful performance of the transducer irradiation test required accurate knowledge of the nuclear heating rate within the in-pile tube. Because this radiation field had not been extensively mapped, an experiment was planned for the purpose of measuring not only the heating rate but the neutron and gamma-ray fields as well. Although the primary purpose of the mapping experiment was to obtain data needed for the transducer test, it was also desirable to obtain data of general applicability to any irradiation tests to be performed in the in-pile tube. To achieve these objectives, the mapping experiment was divided into three main parts:

1. Spatial mapping with foils and gamma dosimeters.
2. Axial mapping of the gamma dose rate with a 4-cc carbon ion chamber.
3. Axial mapping of the nuclear heating rate with an aluminum calorimeter.

Experimental conditions were adjusted to meet the requirements of the various detectors used. Six irradiations, at a maximum power level of 1.65 kW, were made to complete the

spatial mapping; one irradiation, at power levels from 0 to 165 kW, was made to perform the axial mapping with the ion chamber; and one irradiation, at power levels from 286 kW to 7 MW, was made to obtain the heating rate with the calorimeter.

Aerojet General Corporation, Sacramento, California, as sponsor of the transducer irradiation test, participated in the mapping experiments by providing a large number of gamma dosimeters (mostly of the thermoluminescent type). These dosimeters were returned to AGC for readout and data reduction and analysis. Only that portion of the AGC data pertaining directly to the experiment objectives are presented in this report, i.e., gamma doses; details concerning the readout of the dosimeters and the analysis of the data will be reported by AGC.

In addition to discussing the experimental procedures and presenting the results of the measurements, the errors in the measurements are analyzed, and the gamma dose, gamma dose rate, and heating-rate measurements are correlated. Data presentation includes plots of the spatial distribution of the radiation field of the ASTR in-pile tube.

2. METHODS

2.1 Calorimeter

The pedestal-type calorimeter shown in Figure 1 is one of the devices used to measure the radiation field in the ASTR core. By measuring the steady-state temperature differential between two points near the ends of the stem, one can calculate the heating rate associated with this temperature difference and, from this, calculate the gamma dose rate.

The calorimeter was designed to produce large temperature differences over short path lengths, resulting in greater accuracy of measurement, particularly at low heating rates. The calorimeter is made of aluminum and consists, essentially, of a target (bob), a stem, and a heat sink. The entire probe is enclosed in a thin-walled aluminum dome evacuated to a pressure of about 30 microns. The rarefied air surrounding the probe virtually eliminates heat losses through air convection and conduction.

If radiation losses are disregarded for the moment, all heat generated in the probe at thermal equilibrium will essentially be lost through one-dimensional heat flow along the stem of the probe. This heat loss can be calculated very accurately for high-purity 2S aluminum, which has a relatively constant thermal conductivity of $k = 0.57 \text{ cal/cm-sec-}^{\circ}\text{C}$ from 0° to 300°C (Ref. 2). Heat probes similar to this one have been successfully used to measure high dose rates in nuclear reactors (Ref. 3).

2.1.1 Theory

Assuming that the penetrating radiation in the reactor will produce heat uniformly throughout the small probe at a rate of $q \text{ cal/cm}^3\text{-sec}$, one can write the steady-state temperature equation for one-dimensional heat flow (Ref. 4) along the stem of the probe as

$$\frac{d^2T}{dx^2} = - \frac{q}{k} \quad (1)$$

Now if the thermocouples are separated by a distance of L anywhere along the stem of the probe having a cross-sectional area A , and if V' is the volume of aluminum (upstream from $x = 0$) from which heat will flow through the volume $V = LA$ between the thermocouples, then the boundary conditions for solving Equation 1 are:

$$\begin{aligned} T(x) &= T_1 \quad \text{at } x = 0 \\ T(x) &= T_2 \quad \text{at } x = L \\ \phi &= \frac{qV'}{A} = -k \left(\frac{dT}{dx} \right)_{x=0} \end{aligned} \quad (2)$$

where ϕ is the flux of heat into the end of the stem at $x = 0$ due to nuclear heating in the volume V' .

As shown in Appendix A, the solution of the boundary-value problem above gives the relationship between the heating rate per unit volume, q , and the temperature differential, ΔT , between the thermocouples on the stem of the probe. This relationship is

$$q = \frac{2k A}{L} \frac{\Delta T}{2V' + V} \quad (3)$$

Using the dimensions given in Figure 1 (which were measured to the nearest 0.001 in. on a traveling microscope), one obtains the following values:

$$\begin{aligned} V' &= 1.362 \text{ cm}^3 & A &= 0.0979 \text{ cm}^2 \\ V &= 0.182 \text{ cm}^3 & L &= 1.862 \text{ cm} \end{aligned}$$

Substitution of these values into Equation 3 yields

$$q = 1.146 \Delta T \times 10^{-2} \text{ cal/cm}^3\text{-sec} \quad (4)$$

where ΔT is in $^{\circ}\text{F}$ in all equations that follow and k is in compatible units.

The nuclear heating rate per unit mass, q^* , which is found by dividing Equation 4 by the density of the aluminum probe ($\rho = 2.71 \text{ g/cm}^3$), is

$$\begin{aligned}
 q^* &= 4.23 \quad \Delta T \times 10^{-3} \text{ cal/g Al-sec} \\
 &= 1.77 \quad \Delta T \times 10^{-2} \text{ watt/g Al}
 \end{aligned}
 \tag{5}$$

This gives the actual heating rate per gram of aluminum in the probe. However, it is conventional to refer energy absorptions in all materials to an equivalent absorption in a carbon standard. If it is assumed that the entire heating rate above is due to gamma rays, as most of it will be, and that the gamma energy absorbed per target electron is the same for a gram of aluminum and carbon, then the ratio of the atomic number over the atomic mass for carbon and aluminum gives an equivalence of

$$1 \text{ watt/g Al} = 1.038 \text{ watt /g C}$$

Hence, the gamma heating rate per gram is about the same for aluminum and carbon, and as a first approximation the nuclear heating rate of Equation 5 for aluminum will convert into a carbon rate of

$$q_c^* = 1.84 \quad \Delta T \times 10^{-2} \text{ watt/g C} \tag{6}$$

where ΔT is still measured in $^{\circ}\text{F}$ on the aluminum probe.

In order to obtain direct comparisons with the ion chamber and other measurements, q^* can be converted into a gamma dose rate in roentgen per hour through the equivalence of

$$1 \text{ cal/g Al-sec} = 1.782 \times 10^9 \text{ R/h}$$

if one assumes that a dosage of 1 R is equivalent to the absorption of 87.6 ergs of gamma energy in a gram of air, regardless of the energy of the gammas involved, and that the energy absorbed per target electron is the same for air and aluminum. Here, the ratio of the atomic number over the atomic mass for aluminum and air gives an electron per gram ratio of 0.965 to make 1 R equivalent to an energy absorption of 84.5 ergs/g of aluminum or 87.7 ergs/g of carbon. Hence, again considering heating in the reactor to be due exclusively to gammas, q^* in terms of dose rate is

$$q_d^* = 7.54 \quad \Delta T \times 10^6 \text{ R/h} \tag{7}$$

This equation gives the gamma dose rate for a given reactor power in terms of the measured temperature difference in $^{\circ}\text{F}$ between thermocouples on the stem of the calorimeter probe when an equilibrium condition has been reached in which temperatures are not varying with time. If one assumes that steady-state conditions are essentially satisfied when ΔT reaches 99% of its infinite-time value, then (as derived in Appendix A) the time required to approach equilibrium will be given by

$$t = \frac{-C_p \Delta T}{q^*} \ln(0.01) = 139 \text{ sec} = 2.3 \text{ min}$$

where $C_p = 0.23 \text{ cal/g } ^{\circ}\text{C}$ is the specific heat of aluminum. Thus, equilibrium will be set up rather quickly after a change in the reactor power level, and the time required will essentially be independent of the initial temperature differential over the probe when the power is changed.*

2.1.2 Corrections to the Theory

2.1.2.1 Heat Losses

The theory of the previous section requires all of the heat generated in the probe at equilibrium to be conducted out through its stem. To make this a good assumption, the probe was positioned inside an evacuated dome and attached to its water-cooled base. There will still be some heat loss through radiation upstream from the thermocouples, however, and this can be estimated from the Stefan-Boltzmann law (Ref. 4) as

$$Q_r = 1.374 \epsilon S (\bar{T}_b^4 - \bar{T}_d^4) \times 10^{-12} \text{ cal/sec} \quad (8)$$

Here, Q_r is the net rate of heat loss in the radiation exchange between the hotter bob (target) of the probe and its surrounding dome, which have average absolute temperatures of \bar{T}_b and \bar{T}_d , respectively, and $\epsilon = 0.1$ is the emissivity of the semi-polished bob of the probe, which has a surface area of $S = 7.13 \text{ cm}^2$.

*The initial ΔT would begin to have more and more influence on t if the quasi-equilibrium condition of 99% of the final ΔT were steadily relaxed to lower percentages. In practice, the equilibrium time was determined by the heat sink.

The maximum temperature measured on the target end of the calorimeter stem during the highest level of reactor operation (7 MW, was 240°F , and the maximum temperature at the mid-height of the dome was 170°F . The temperature differential over the bob of the probe should be only about 10°F here, so that the average temperature of the bob will be about 245°F . Calculations show that the very tip of the dome should be about twice as hot as its lower rim and that the midpoint should have roughly the average temperature of the two extremes. Hence, the 170°F temperature at mid-height should approximate the average dome temperature at this power level, and tip-to-tip temperatures should vary from about 230°F to 115°F with the water-cooled base of the dome having a temperature of about 90°F .

The net rate of heat loss from the bob of the probe, at $T_b = 392^{\circ}\text{K}$ (or 245°F), to the dome, at $T_d = 350^{\circ}\text{K}$ (or 175°F), can then be estimated from Equation 8 as

$$Q_r = 9.8 (2.36 - 1.50) \times 10^{-3} = 8.4 \times 10^{-3} \text{ cal/sec} \quad (9)$$

Therefore, instead of having a steady-state heat flux of $\dot{Q} = qV'/A$ into the stem of the probe, as in Equation 2, one will actually have $(qV - Q_r)/A$. This will require the term $2Q_r/(2V' + V)$ to be added onto the right-hand side of Equation 2 to give

$$q = (1.146 \Delta T + 0.58) \times 10^{-2} = 1.07 \text{ cal/cm}^2\text{-sec} \quad (10)$$

where the measured ΔT for this power level is 9.6°F . Thus, the percentage error introduced by neglecting radiation losses is estimated to be

$$\frac{100 Q_r}{q \left(V' + \frac{V}{2} \right)} = \frac{59 \left(T_b^4 - T_d^4 \right) \times 10^{-10}}{\Delta T}$$

which, for the case above, gives an error of $0.58/1.07 \approx 0.5\%$.

This radiation calculation is very rough, of course, since temperature distributions and geometries are largely ignored but one has only a 4.5% error in the worst imaginable case: an oxidized probe (with $\epsilon = 0.3$) that radiates to the dome and

a dome that radiates only to its water-cooled base. In this worst case, the first term of Equation 9 is multiplied by a factor of 3 and the second term drops out completely. This is no doubt an overestimate, and it is very unlikely that the heat loss through radiation could amount to more than 2 or 3% for this highest level of reactor operation. The fraction of heat lost through radiation will decrease for lower power levels (Table 1) and will essentially disappear for reactor operation below 1 MW, when the probe and dome will be maintained at about the same temperature.

Table 1

ESTIMATED RADIATION HEAT LOSSES FROM
THE PROBE AT VARIOUS POWER LEVELS

Power Level (MW)	$\Delta T(^{\circ}\text{F})$	$\bar{T}_b(^{\circ}\text{K})$	$\bar{T}_d(^{\circ}\text{K})$	$Q_r \times 10^3$	Loss (%)
0.273	4.1	307	307	0	0
0.455	7.0	310	310	0	0
0.909	13.4	316	316	0	0
1.890	28.0	328	322	0.74	0.17
4.520	63.9	362	344	3.14	0.29
6.780	93.4	392	350	8.40	0.54

In summary, heat losses from the probe are thought not to exceed 2 or 3% for any reactor power, and corrections can be made for these losses by adding an additional term to Equation 5, as shown below:

$$\begin{aligned}
 q^* &= 4.23 \Delta T \times 10^{-3} + 0.254 C Q_r \text{ cal/g Al-sec} \\
 &= 1.77 \Delta T \times 10^{-2} + 1.062 C Q_r \text{ watt/g Al}
 \end{aligned}
 \tag{11}$$

where C is a parameter that corrects the Q_r of Equation 8 for temperature distributions and geometrical considerations; it is

thought not to exceed a value of 2. The Q_r 's for various reactor powers are listed in Table 1 for an emissivity of $\epsilon = 0.1$.

The corresponding heating rate in carbon, corrected for heat losses but still uncorrected for neutron heating, is obtained from the second expression of Equation 11 as

$$\begin{aligned} q_c^* &= 1.038 q^* \text{ watt/g C} \\ &= 1.84 \Delta T \times 10^{-2} + 1.10 CQ_r \text{ watt/g C} \end{aligned} \quad (12)$$

Likewise, the gamma dose rate, corrected for heat losses, is obtained from the first expression of Equation 11 as

$$\begin{aligned} q_d^* &= 1.782 q^* \times 10^9 \text{ R/h} \\ &= (7.54 \Delta T + 453 CQ_r) \times 10^6 \text{ R/h} \end{aligned} \quad (13)$$

2.1.2.2 Neutron Heating

Before converting the nuclear heating rate into a gamma dose rate through Equation 13, one should also make a correction for neutron heating. There are two significant mechanisms for neutron heating in the aluminum probe: elastic scattering and neutron capture. The higher-energy neutrons in a reactor spectrum cause heating mainly through elastic scattering, while those near thermal energies cause heating through neutron capture.

The rate of energy absorption in the aluminum probe through isotropic scattering of neutrons is given by

$$E_a = 2.46 \times 10^{-9} \int_0^{\infty} E \sigma_{el}(E) f(E) dE \text{ erg/g-sec} \quad (14)$$

where $\sigma_{el}(E)$ is the elastic scattering cross section, in barns, for neutrons of energy E , in MeV, and $f(E)$ is the differential neutron flux incident on the probe. If one assumes that the differential flux in the in-pile tube has the shape of Watt's fission spectrum, normalized to make its maximum value equal to unity, then Equation 14 can be numerically evaluated to give

$$E_a = 2.8k \times 10^{-8} \text{ erg/g-sec} \quad (15)$$

where k is the normalization factor required to make the fission spectrum agree with the measured ASTR spectrum.

The neutron flux above 1 MeV has been measured with sulfur detectors to give the flux per unit power level P as

$$\frac{1}{P} \int_1^{\infty} f(E) dE = 3.8 \times 10^6 = \frac{k}{P} \int_1^{\infty} f_s(E) dE \quad (16)$$

The normalized fission spectrum $f_s(E)$ has been numerically integrated above 1 MeV to give a flux of 2.2 neutrons/cm²-sec, so that

$$\frac{k}{P} = \frac{3.8 \times 10^6}{2.2} = 1.73 \times 10^6 \text{ watt}^{-1}$$

Therefore, the rate of energy absorption from elastic scattering in each gram of the probe per unit reactor power will be, from Equation 15,

$$\frac{E_a}{P} = 4.85 \times 10^{-2} \text{ erg/g-sec-watt} \quad (17)$$

Now 1 R/h is equivalent to an energy absorption in aluminum of 2.35×10^{-2} erg/g-sec, so that Equation 13 can be rewritten in terms of a heating rate as

$$q^* = (1.77 \Delta T + 106.2 CQ_T) \times 10^5 \text{ erg/g-sec} \quad (18)$$

At the centerline of the reactor core, where ΔT was measured to be 28°F for a power level of $P = 1.89$ MW, the heating rate per unit power level is

$$\frac{q^*}{P} = 2.64 \text{ erg/g-sec-watt} \quad (19)$$

Hence, the percentage contribution of heating from neutron scattering to the total nuclear heating rate in the probe is, from Equations 17 and 19,

$$\frac{100 E_a}{q^*} = \frac{4.85}{2.64} = 1.84\% \quad (20)$$

Energy is absorbed from (n, γ) reactions in the aluminum probe in two stages. The excited compound nucleus formed by thermal-neutron capture will first decay to its ground state through the emission of prompt gammas having energies of 7.7 MeV. The radioactive aluminum-28 nucleus will then have a half-life of 2.3 min for undergoing beta decay accompanied by a 8-MeV gamma ray. The upper-point energy for this beta decay is 2.87 MeV; but all lower energies can be carried off, depending on how the disintegration energy is shared with accompanying neutrinos. Thus, the capture of a neutron having essentially no kinetic energy will make available an energy of about 12.4 MeV, a good fraction of which will be absorbed and will go into heating the probe.

The (n, γ) cross section, $\sigma_{n\gamma}$ (in barns), is appreciable only for the near-thermal neutrons, so that if the average beta energy is \bar{E}_β MeV and if these electrons are always stopped in the probe, then the energy absorbed only from the beta particles produced in a thermal-neutron flux of Φ_{th} is

$$E_a = 3.56 \sigma_{n\gamma} \Phi_{th} \bar{E}_\beta \times 10^{-8} \text{ erg/g-sec} \quad (21)$$

The thermal-neutron flux per unit power level in the ASTR tube was determined from the activation of bare and cadmium-covered copper samples to be $\Phi_{th}/P = 5 \times 10^6 \text{ n/cm}^2\text{-sec-watt}$, and the thermal cross section for the (n, γ) reaction in aluminum-27 is 0.21 barn, so that for an average beta energy of 1 MeV,

$$E_a/P = 3.74 \times 10^{-2} \text{ erg/g-sec-watt} \quad (22)$$

If one assumes that the average path length \bar{x} of a gamma in escaping from the probe is 0.75 cm, that gammas will on the average give up half of their energies to electrons in Compton collisions, and that the average Compton cross section σ_c for an aluminum atom is 1.5 barns, then the energy absorbed from gammas once an (n, γ) reaction takes place is roughly approximated by

$$0.03 \bar{x} \sigma_c \sum E_{\gamma i} = 0.32 \text{ MeV/reaction}$$

Such reactions will be taking place at the rate of $2.23 \times 10^{-2} \sigma_{n\gamma} \Phi_{th}$ reaction/g-sec to give

$$E_a = 1.14 \sigma_{n\gamma} \Phi_{th} \times 10^{-8} \text{ erg/g-sec}$$

or

$$E_a/P = 1.2 \times 10^{-2} \text{ erg/g-sec-watt} \quad (23)$$

The rate of energy absorption from all exit particles of (n,γ) reactions is now given by combining Equations 22 and 23 to obtain

$$\begin{aligned} E_a/P &= 3.74(1 + 0.32) \times 10^{-2} \\ &= 4.94 \times 10^{-2} \text{ erg/g-sec-watt} \end{aligned} \quad (24)$$

The percentage contribution to the total nuclear heating rate from (n,γ) reactions in the probe is then given, as in Equation 20, by

$$\frac{100 E_a}{q^*} = \frac{4.94}{2.64} = 1.87\% \quad (25)$$

which is almost exactly the same as the elastic-scattering contribution. Finally, combining Equations 20 and 25, the total contribution from neutron heating in the probe is estimated to be

$$\frac{100}{q^*} [E_a(e^+) + E_a(n, \gamma)] = 3.7\% \quad (26)$$

Now having broken down the nuclear heating rate in aluminum into contributions from gammas and neutrons, and having further divided the neutron heating into equal contributions from elastic scattering and capture reactions, one can make better estimates for the heating rate in carbon and for the gamma dose rate than those of Equations 12 and 13. The counterpart of Equation

14 for the rate of energy absorption in carbon through isotropic scattering is given by

$$\begin{aligned}
 E_a &= 1.14 \times 10^{-6} \int_0^{\infty} E \sigma_{ef}(E) f(E) dE \\
 &= 9.8k \times 10^{-8} \text{ erg/g-sec}
 \end{aligned}
 \tag{27}$$

Hence, according to Equations 15 and 27, the heating rate from elastic scattering is 3.5 times as great in carbon as in aluminum for the same neutron flux.

Therefore, since gamma heating is 1.038 times as great in carbon as in aluminum and since neutron capture in carbon is negligible, the ASTR heating rate in aluminum, q^* , will transform into an equivalent heating rate in carbon of

$$\begin{aligned}
 q_c^* &= [0.963 (1.038) + 0.6184 (3.5)] q^* \\
 &= 1.064 q^*
 \end{aligned}
 \tag{28}$$

Using the corrected heating rate in aluminum from Equation 11, this final formula for the heating rate in carbon becomes

$$q_c^* = 1.88 \Delta T \times 10^{-2} + 1.13 CQ_T \text{ watt/g C}
 \tag{29}$$

as compared to Equation 12, where neutron heating was ignored, and to Equation 6, where both neutron heating and heat losses were ignored.

That part of the nuclear heating rate in aluminum due only to gamma rays is given by $q_\gamma^* = 0.963 q^* \text{ cal/g-sec}$, so that the gamma dose rate in the ASTR is

$$q_d^* = 1.782 q_\gamma^* \times 10^9 = 1.716 q^* \times 10^9 \text{ R/h}
 \tag{30}$$

According to Equation 11, this final form for the dose rate becomes

$$q_d^* = (7.26 \Delta T + 435.2 CQ_T) \times 10^6 \text{ R/h}
 \tag{31}$$

as opposed to Equation 15, where no neutron correction was made, and to Equation 7, where no corrections at all were made. This same result is obtained from the gamma heating rate in carbon, of course, which is given by the first term of Equation 28, where

$$q_d^* = 1.718 q_v^* \times 10^9 = 1.718 q^* \times 10^9 \text{ R/h}$$

if 1 R is equivalent to an energy absorption of 87.7 ergs/g of carbon. Here, the gamma heating in carbon is almost exactly equal to the nuclear heating in aluminum for the ASTR.

2.1.3 Calibration

The calorimeter probe was checked out in the laboratory before the actual reactor test to verify the calculated relationship between heat input and the steady-state temperature differential along the stem of the probe. A cylindrical electric heating element of the same diameter as the bob of the probe was placed against the end of the bob and a hollow aluminum cylinder was tightly fitted over the heating element and the bob to join them together (Fig. 2). The probe was then fitted into the water-cooled base of an evacuated aluminum cylinder which had insulated feedthroughs for connecting the heater wires.

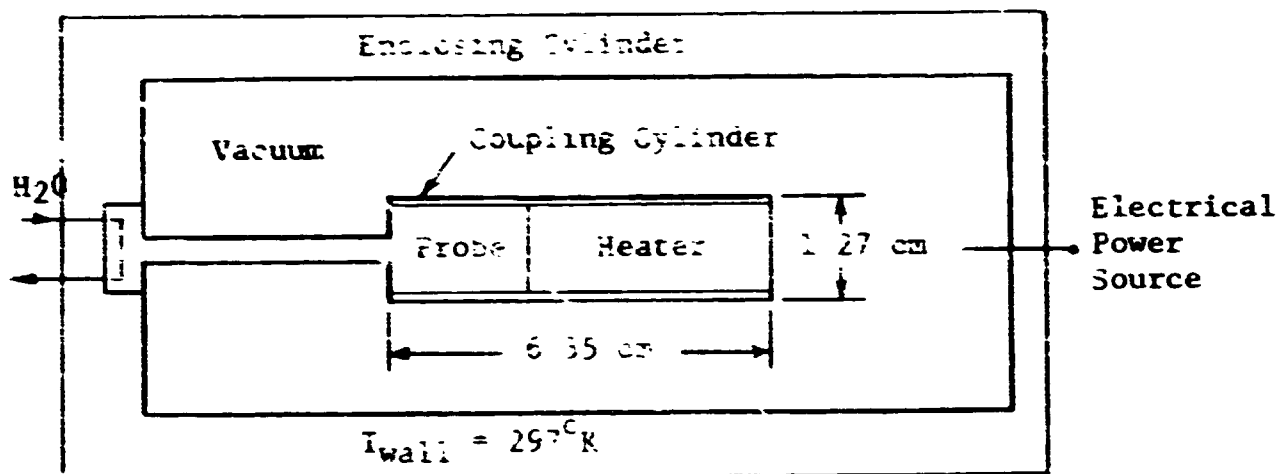


Figure 2 Sketch of Calorimeter in Calibration Configuration

By supplying a known amount of electrical power to the heater, one can measure the steady-state temperature differential between thermocouples on the stem of the probe and compare this measurement with the calculated value obtained from

$$\Delta T = 0.43 \frac{P_c L}{k A} = 14.35 P_o \quad (32)$$

where ΔT is in $^{\circ}\text{F}$, P_c is the electrical power in watts, L is the separation distance between the thermocouples on the stem of the probe, A is the cross-sectional area of the stem, and k is the thermal conductivity of the aluminum. This equation is obtained by setting $q = 0$ in Equation 1, since there is no heat generated in the stem of the probe, and by setting the flux of heat down the stem of the probe equal to $\phi = 0.239 P_o/A$ cal/cm²-sec in Equation 2, so that it applies for simple conduction with no heat losses.

Now, one could measure ΔT for various electrical powers and plot a curve of ΔT vs P_o (Fig. 3) so that if the heat losses were the same in both cases, this could be used as a calibration curve for the reactor test. For example, one could read P_o from the curve for a given ΔT and calculate a nuclear heating rate in the $\pi = 3.94$ g of effective aluminum mass upstream of the thermocouples as

$$q_d^* = \frac{0.239}{m} P_o \frac{\text{cal}}{\text{g-sec}} = 1.082 P_o \times 10^8 \text{ R/h} \quad (33)$$

Here, $m = \rho(V' + V/2)$ is the mass of an imaginary aluminum bob which, when uniformly heated at a rate of q , would give the same ΔT when attached to the actual stem as would the same uniform heating rate of q throughout the bob and stem of the real probe. (Appendix A). Thus, the use of an effective mass corrects for the different distribution of heat generation from electrical and nuclear power.

The assumption of equal heat losses in the laboratory calibration and in the reactor test is far from valid, however, because the heating element provides additional surface area for heat losses in the laboratory and the containing cylinder is not heated, as is the dcme in the reactor. Consequently, larger

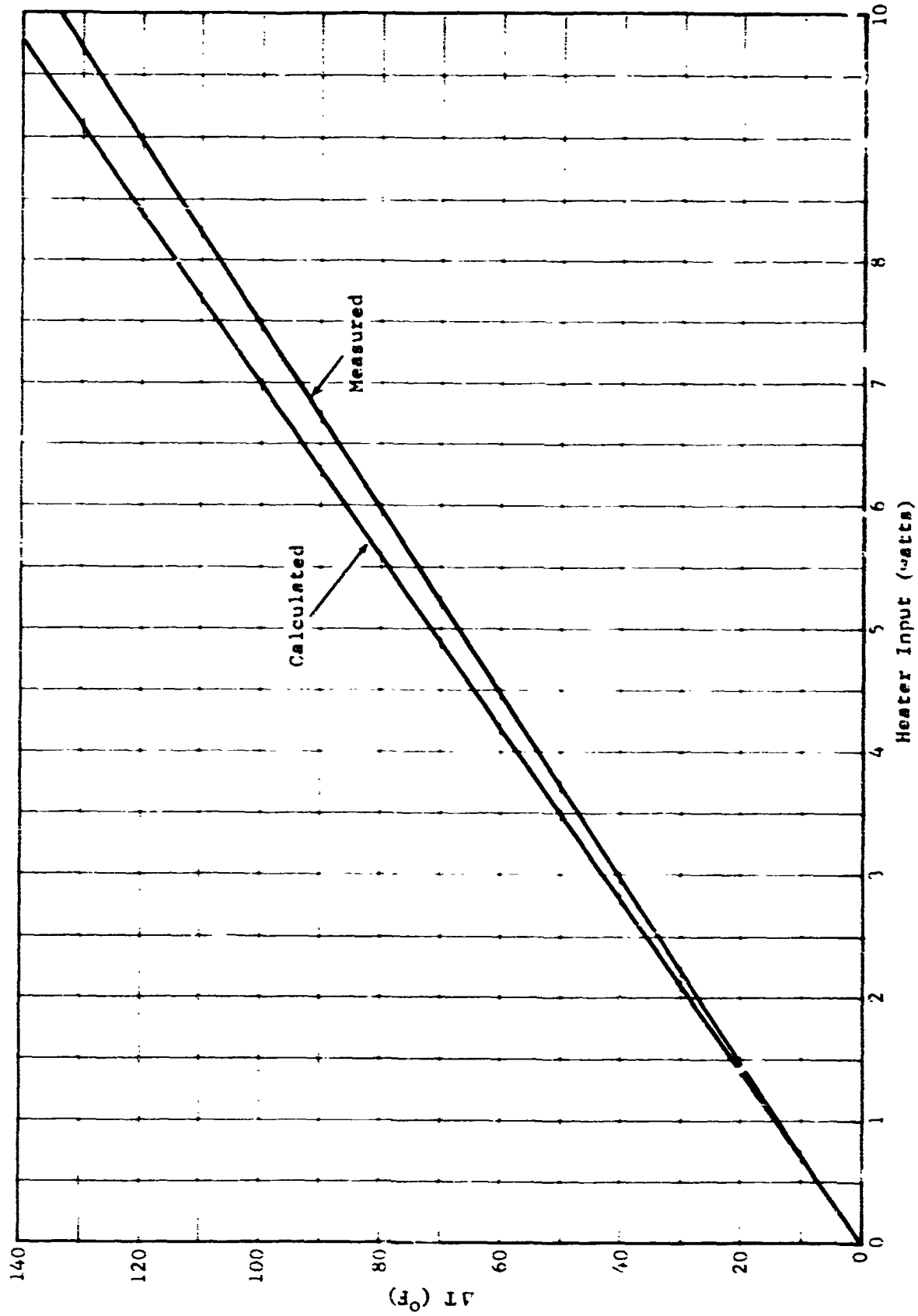


Figure 3 Measured and Calculated Calorimeter Calibration Curves

temperature differentials are developed between the heater-probe unit and its container. In addition, the hollow aluminum cylinder used to couple the probe and the heater together had an unpolished, dull finish, as did the larger aluminum cylinder required to contain the bulkier unit, so that radiation emissivity would be considerably increased. Thus, the net heat loss through radiation in the laboratory would be greatly increased over that in the reactor through both a larger emission from the probe-heater unit, because of increased surface area and emissivity, and a relatively smaller return emission from the walls of the containing cylinder, which are essentially at room temperature.

If one were able to accurately calculate the heat losses in the laboratory and in the reactor, H_L and H_R , respectively, then the calibration curve could still be used to calculate nuclear heating rates from

$$q^* = \frac{0.239 P_0 - H_L + H_R}{m} \frac{\text{cal}}{\text{g-sec}} \quad (34)$$

This would essentially be a calibration only for the thermal conductivity, however, since all other quantities in the theory, corrected for heat losses, are directly measurable constants, and the conductivity of pure aluminum is known with much greater accuracy than are the heat losses.

Therefore, unless heat losses can be made roughly the same in the laboratory and in the reactor, then, after satisfying oneself that the calorimeter operates properly in the laboratory for lower power levels, where heat losses are negligible, and that heat losses will be small in the reactor for all power levels, one might just as well use Equation 7 to calculate loss-free gamma dose rates rather than trying to calibrate the probe. Equation 7 is obtained by solving Equation 32 for P_0 and substituting into Equation 33, so that when one plots the calculated curve of ΔT vs P_0 from Equation 32 and compares this to the curve measured in the laboratory, as in Figure 3, then the difference in these curves indicates heat losses in the laboratory if all input data to the theory are correct, and apparently they are since the lower-power parts of the curves agree when heat losses are negligible.

A brief review of calibration attempts is in order before discussing the final calibration curve of Figure 3 in greater detail. Heat losses measured in the first calibration attempt are shown in the left-hand side of Table 2, and calculations required to explain these losses are shown in the right-hand side of the table. The measured heat-loss percentages are determined for various electrical power inputs by comparing thermocouple temperature differentials to calculated values from Equation 32. The average probe-heater temperatures necessary for explaining these measured heat losses are calculated from the Stefan-Boltzmann radiation law and are listed in the T_b column, where it is assumed that the emissivity of the dull aluminum coupling, having a surface area of 27.9 cm^2 , might be as high as 0.5, and that the side walls of the containing cylinder are maintained at a constant temperature of 297°K . The heat losses themselves, Q_r , are then shown for these temperatures, and percentage losses are calculated from $100 Q_r/P_o$.

Table 2
HEAT LOSSES IN INITIAL CALIBRATION
OF THE CALCRIMETER

P_o (watts)	$\Delta T(^{\circ}\text{F})$		Measured Heat Loss (%)	T_b ($^{\circ}\text{K}$)	Q_r (watts)	Calculated Heat Loss (%)
	Exp.	Calc.				
0.51	6.2	7.3	15.1	306	0.079	15.5
1.05	12.9	15.1	14.5	314	0.156	14.8
2.02	24.7	29.0	14.8	328	0.304	15.1
3.95	48.6	56.7	14.3	349	0.565	14.3

The temperatures needed to explain the results above through radiation losses are quite reasonable and only require temperature differentials over the probe-heater unit of 18° , 29° , 45° , and 53°F , from lower to higher powers, where the measured temperatures on the stem at the base of the bob are 82° , 91° , 108° , and

142°F, respectively. The temperature at the point where the wire entered the heater element was monitored for the higher 4-watt power and was found to reach 260°F. It is thought that the temperature of the hot end of the outer aluminum coupling would be considerably less than this, but it might well approach 195°F as suggested by the rough calculations above.

Thus, we have now shown that the discrepancies in the initial calibration attempt can be largely explained through radiation losses (Table 2), and that radiation losses should be about thirty times as great in the laboratory as in the reactor (Table 1). Hence, if it can be demonstrated that the calorimeter will operate properly in the laboratory for low-power levels where heat losses can be restricted, then the probe can be used with considerable confidence in the reactor without regard to the actual calibration data obtained in the laboratory under different conditions.

In order to restrict heat losses in this final calibration to something on the order of those expected in the reactor, the probe-heater unit was wrapped in a bright aluminum foil having a low emissivity and the inside of the containing cylinder was lined with asbestos paper. The measured temperature differentials under these conditions are compared to values calculated from Equation 32 in Table 3, and the results are plotted in Figure 3. If the heater power corresponding to a measure ΔT in the reactor is found from the calculated curve of Figure 3 and is substituted into Equation 33, then one obtains the theoretical dose rates of Equation 7 for the case where no heat is lost. Using the measured curve in the same manner corrects for heat losses if reactor conditions are simulated by the specially insulated probe-heater unit. Neither of these conditions is expected to hold exactly, but the true calibration curve is expected to fall somewhere between the two curves of Figure 3, and it should probably be closer to the calculated curve.

Table 3

**HEAT LOSSES IN FINAL CALIBRATION
OF THE CALORIMETER**

P_0 (watts)	$\Delta T(^{\circ}F)$		Heat Loss (%)	Non-Wire Heat Loss (%)
	Exp.	Calc.		
1.02	14.2	14.6	2.7	1.2
2.03	27.7	29.1	4.8	3.3
4.15	56.0	59.6	6.0	4.5
7.73	103.4	110.9	6.8	5.3
10.17	135.5	145.9	7.1	5.6

The percentage of heat lost through the copper heater wires at a power of P_0 is approximated by $0.03 \Delta T/P_0$, where ΔT is the temperature difference over the length of the wire. This temperature difference has been measured to be $185^{\circ}F$ at a heater power of 4 watts, so that the heat loss through the wires is about 1.5%. This is expected to hold roughly for all electrical powers, since $\Delta T/P_0$ changes slowly with power. Therefore, by adjusting the powers of Table 3 for a constant heat loss of 1.5% through electrical wires, one can recalculate ΔT for the probe and obtain still better agreement between theory and measurement, as recorded in the final column of the table. Thus, Table 3 indicates that the calorimeter would be accurate to within about 1% or better if all heat losses could be prevented, and, coupled with the data of Tables 1 and 2, this completes the verification of calorimeter operation in the reactor, i.e., Table 1 implies that radiation heat losses are small in the reactor; Table 2 implies that heat losses are mostly through radiation; Table 3 implies good accuracy is obtained when heat losses are small. Consequently from Tables 1, 2, and 3, it may be concluded that the calorimeter will provide accurate measurements in the reactor field.

In summary, the calibration technique, as outlined, cannot be used to correct for calorimeter errors because of the large difference in heat losses in the two applications. It does indicate, however, that the calorimeter is operating properly and that the input data to the theory are correct to within a percent or so. Moreover, it indicates that the corrections for heat losses in the reactor as made in Equations 11, 12, and 13 should be roughly valid. Hence, the final formulas of Equations 29 and 31 will be used to calculate the carbon heating rate and the gamma dose rate in the ASTR.

2.2 Ion Chamber

2.2.1 Characteristics

The 4-cc carbon ion chamber is designed to measure large gamma-ray doses in the presence of neutrons in a reactor field. It operates by the action of gamma rays knocking electrons from an outer electrode; these electrons, in turn, ionize the gas between the outer electrode and an inner one. The ions thus formed are drawn to their respective electrodes and the resulting current is measured by means of a suitable current-measuring device. By exposing the chamber in a known gamma-ray field of suitable intensity, the relationship between exposure dose rate and output current is established.

The ion chamber used in this experiment has electrodes of nuclear graphite and is filled with CO₂ at a pressure of 760 mm-Hg; the active volume is approximately 4 cc. The outer electrode is 0.25 in. thick, sufficient to provide electron equilibrium for reactor radiation. Ion chambers of this type have been investigated extensively (Ref. 5), and their principal characteristics are summarized as follows:

<u>Parameter</u>	<u>Value</u>
Dose-rate range	10 to 5×10^7 R/h
Neutron sensitivity	2.5%
Directionality	Response substantially flat with angles from 0° to 140°
Temperature sensitivity	0.1% per °F between 75° and 120°F
Current output	10^{-11} to 10^{-6} amp

<u>Parameter</u>	<u>Value</u>
Linearity	+ 3% or better on all ranges with re- corder readout
Precision	+ 1%
Accuracy	+ 10%

2.2.2 Neutron Sensitivity

The measured sensitivity of the ion chamber per unit neutron flux is given as a function of incident energy in Reference 5. If this response is numerically integrated over a neutron fission spectrum, normalized to give a neutron flux per watt above 1 MeV of 3.8×10^6 n/cm²-sec-watt, then one obtains a neutron sensitivity at the core centerline of

$$N_s = 2.7 \text{ R/h-watt}$$

Based on the calorimeter data, this amounts to a correction of 2.5% for neutron response in the ion chamber. This correction is applicable to all core positions.

2.2.3 Calibration

The gamma sensitivity of the ion chamber was determined by putting it in the known field of a cobalt-60 irradiator and monitoring the chamber output with a picoammeter. The sensitivity was checked over a period of three days to verify the stability of the detector and instruments. (The same picoammeter, power supply, and cables were used in the irradiation.) In a field of 2.09×10^5 R/h, the current was 8.60×10^{-8} amp, giving a sensitivity of 2.43×10^{12} R/h-amp.

The cobalt irradiator source consists of seven vertical pencil sources, 6.5 in. long by 0.5 in. in diam, equally spaced to form a cylindrical geometry. The diameter of the source array can be varied from 1.42 in. to 7.45 in. The source strength at the time of calibration was about 980 Ci.

In the calibration procedure, the ion chamber was positioned at the center of the source array. The diameter of the source array was 5 in., so that the dose-rate variation over the detector was slight. The center position has been

calibrated by several methods: an absolute ion chamber, a ceric chemical dosimeter, and a Victoreen R-Meter that was calibrated at NBS using an intermediate source and ion chamber. The values agree to within $\pm 3\%$. Dose rates are reproducible to $\pm 1\%$.

2.3 Dosimeters

2.3.1 Cobalt Glass

When cobalt glass is exposed to gamma radiation, it undergoes an increase in optical density that is proportional to the exposure dose. This property is utilized by reading the density at selected wavelengths with a Beckman DK spectrophotometer both before and after irradiation.

Because of its high sensitivity to the thermal neutrons in a reactor field, cobalt glass is enclosed in thermal-neutron shields of borated epoxy. The sensitivity to fast neutrons is less than 1%.

The usable dose range of cobalt glass is from about 10^4 to 2×10^6 R. The dosimeters are calibrated by exposing the plates in the known field of the cobalt-60 irradiator and reading the light transmission both before and after irradiation. Exposures are normally made for several time durations so as to provide calibrated dosimeters for the usable dose range.

2.3.2 Thermoluminescent

These dosimeters make use of the thermoluminescent properties of calcium fluoride (manganese activated) and lithium fluoride. When these materials are exposed to ionizing radiation, electrons are raised to metastable states. Upon the addition of energy in the form of heat, the electrons return to their ground states with the emission of visible light. The light output is read and related to the exposure through a calibration in the known gamma-ray field.

Since these dosimeters can be reused many times, the ones used in this experiment were given a low exposure (~ 100 R) and read out in the usual manner. These data were then used

(by AGC) to correct for variations in response (up to 25%) among the individual dosimeters. The dosimeters were then baked out prior to exposure in the reactor field.

Data reported in this document were obtained by use of calcium fluoride and lithium fluoride microdosimeters ($\text{CaF}_2\text{:Mn}$ and Li^7F), miniature lithium fluoride dosimeters (mLi^7F), and hot-press calcium fluoride dosimeters ($\text{HP CaF}_2\text{:Mn}$).

The calcium fluoride microdosimeters consist of $\text{CaF}_2\text{:Mn}$ power hermetically sealed in very small glass tubes (0.9 mm by 6.0 mm). The exposure range is 1 R to 10^5 R. According to the manufacturer, fast-neutron response is 1×10^{-9} R per n/cm^2 .

The lithium fluoride microdosimeters are constructed in a manner similar to the calcium fluoride dosimeters. The response of lithium fluoride as a function of gamma-ray energy is about 10^5R . Lithium-7 dosimeters have a very low neutron response, whereas lithium-6 dosimeters have a high sensitivity to thermal neutrons.

The miniature lithium fluoride dosimeters contain 10 mg of Li^7F in a glass capillary 1.4 mm in diameter and 12 mm long.

The hot-press calcium fluoride dosimeters, formed at high temperature and pressure, are rectangular pellets with dimensions of 1/8 by 1/8 by 1/16 in. The dose range is given as 5 mR to 3×10^5 R.

2.4 Foils

2.4.1 Types

Neutron-flux measurements were made by foil-activation techniques. Foils or pellets of selected radioactants were exposed in the in-pile tube and the level of radioactivity was subsequently determined by counting beta-particle emission. From the measured count rate, the saturated activity was computed, and this information, when combined with the activation cross section and number of atoms of radioactant, was used to determine the flux of neutrons in specific energy regions.

The procedures are well established and need not be elaborated on here; however, detailed discussions of the theory and practice of neutron-flux measurements in reactor fields may be found in References 6 through 8.

The radioactivants used in this experiment are described in Table 4. The most numerous measurements were made with sulfur pellets and copper and aluminum foils; the additional foils and pellets (two sets of each) were exposed for the purpose of roughly defining the neutron spectrum.

2.4.2 Calibration

The efficiency of a particular counter for counting a particular type of foil is defined as the ratio of the count rate of the foil on the specific counter to its absolute disintegration rate. Since the foils used for routine flux measurements are frequently not suitable for absolute counting, and the counters used for routine counting are not absolute counters, it is necessary to determine the counter efficiency; hence, the absolute disintegration rate must be determined.

The efficiencies of the routine counters for counting the various types of foils have been determined by calibration procedures which are repeated periodically. In these calibrations, the foils are irradiated to a suitable activation level and then counted on the routine counter and also by an absolute method. The absolute disintegration rates are usually measured by one or both of two methods. 4π counting or beta-gamma coincidence counting. Thermal-neutron detectors having a sufficiently large capture cross section are also irradiated in the known thermal flux of a standard pile, and the unknown thermal-neutron flux can then be obtained by a direct comparison of count rates on a routine counter.

The 4π technique consists of dissolving an activated foil in a common acid, depositing an aliquot of this solution containing a known fraction of the foil on a thin sample holder, and counting this sample in a 4π counter.

The beta-gamma coincidence technique can be employed for radioactivants having simple decay schemes - ideally a single beta particle accompanied by a single gamma ray. From a measurement of the number of beta counts, the number of gamma

Table 4

SUMMARY OF DATA FOR NEUTRON DETECTORS

Element	Stable Isotopes	Purity of Isotopes (%)	Res. or Thresh. Energy (Nominal)	Reaction Type	Product Half-Life	Foil Composition	ID Code NARF	Total Foil Weight (g)	Isotopic Foil Weight (g)	λ_1 (m^{-1}) ^a	$T_{1/2}^b$ (h)	λ_2 (m^{-1})	$T_{1/2}^b$ (h)	λ_3 (m^{-1})	$T_{1/2}^b$ (h)
Lutetium	Lu-175 Lu-176	97.4 2.6	1/V 0.142 eV	n, γ n, γ	3.7 h 6.8 d	10 wt-% Lu ₂ O ₃ Al Matrix	LU	0.500	1.143(-3) ^a	7.08(-5)	6.8 d	7.70(-4)	15 h	3.12(-3)	3.7 h
Europium	Eu-151 Eu-153	47.77 52.23	0.327 eV 1/V	n, γ n, γ	9.2 h 16 y	1 wt-% Eu ₂ O ₃ Al Matrix	EU	0.500	2.07 (-3)	1.24(-3)	9.2 h	7.70(-4)	15 h	9.09(-8)	16 y
Indium	In-113 In-115	4.23 95.77	1/V+Misc 1.457 eV	n, γ n, γ	49 d 54.2 m	1 wt-% In ₂ O ₃ Al Matrix	IO	0.500	4.134(-3)	1.28(-2)	54.2 m	7.70(-4)	15 h	---	---
Gold	Au-197	100	4.906 eV	n, γ	2.7 d	Thin Au on Ni-Mn	AB	---	1.00	1.78(-4)	2.7 d	1.78(-6)	270 d	---	---
Samarium	Sm-152 Sm-154	26.63 22.53	8.01 eV 1/V	n, γ n, γ	46.2 h 24 m	1 wt-% Sm ₂ O ₃ Al Matrix	SO	0.500	1.156(-3)	2.50(-4)	46.2 h	7.70(-4)	15 h	2.89(-2)	24 m
Tungsten	W-184 W-186	30.6 28.4	1/V 18.8 eV	n, γ n, γ	73 d 24 h	2 mil x 1 cm ² Foil	WB	0.100	2.84(-2)	4.81(-4)	24 h	6.59(-6)	73 d	---	---
Lanthanum	La-139	99.911	73.5 eV	n, γ	40 h	25 wt-% La ₂ O ₃ Al Matrix	LO	0.500	1.065(-1)	2.88(-4)	40 h	7.70(-4)	15 h	---	---
Cadmium	Cd-106 Cd-114	1.22 28.86	1/V 120.2 eV	n, γ n, γ	6.7 h 53 h	50 wt-% CdO Al Matrix	CO	0.500	6.30(-2)	2.18(-4)	53 h	7.70(-4)	15 h	1.12(-5)	43 d
Manganese	Mn-55	100	337 eV	n, γ	2.58 h	Ag-Mn Foil	AZ	0.045	6.75(-3)	4.47(-3)	2.58h	1.78(-4)	2.7 d	1.78(-6)	270 d
Copper	Cu-63 Cu-65	69.1 30.9	580 eV 1/V+Misc	n, γ n, γ	12.8 h 5 m	2 mil x 1 cm ² Foil	CA	0.046	3.14(-2)	9.01(-4)	12.8 h	2.48(-7)	5.3 y	---	---
Phosphorus	P-31	100	0.1 MeV	n, γ	14.3 d	1 cm ² Al Metaphosphate	PM	0.500	1.75(-1)	3.37(-5)	14.3 d	4.47(-3)	2.58h	7.70(-4)	15 h
Indium	In-115	95.77	0.85 MeV	n, n'	4.5 h	20 mil x 1 cm ²	IA	0.38*	3.65(-1)	1.28(-2)	54.2 h	2.56(-3)	4.5 h	9.82(-6)	49 d
Sulfur	S-32	95.018	2.9 MeV	n, p	14.3 d	125 mil x 1 cm ²	SK	0.585	5.56(-1)	3.37(-5)	14.3 d	4.47(-3)	2.58h	---	---
Aluminum	Al-27	100	8.1 MeV	n, α	15 h	Al Matrix	AO	0.500	5.00(-1)	1.70(-4)	15 h	---	---	---	---

^a λ = Decay Constant^b $T_{1/2}$ = Half-life^c (-1) = 10⁻¹

counts, and the number of coincident beta and gamma counts, the absolute disintegration rate can be computed (Ref. 6).

Many of the foils listed in Table 4 are not amenable to calibration by 4 π counting (relatively insoluble), coincidence counting (complex and/or not well-known decay schemes), or irradiation in the standard pile (cross section small and/or half-life long). Therefore, the actual calibrations in these cases were by one of the following methods (Ref. 8):

1. A relative method employing 4 π counting of special detectors manufactured with aluminum sulfate instead of aluminum powder. Since these foils are readily soluble in acid, they could be calibrated by the 4 π technique. By irradiating the standard and special foils simultaneously in the same neutron flux, a direct comparison of count rates on a routine counter was obtained.
2. A comparison method requiring activation in a known thermal flux. In order to obtain sufficiently high flux levels, irradiations were made in the pneumatic tube of the Ground Test Reactor, and the thermal-neutron flux was measured with gold foils that could be calibrated independently.
3. A relative method employing similar foils having known counting efficiencies.

The calibration method and the estimated calibration accuracy for the various foils are given in Table 5.

Table 5
FOIL CALIBRATION METHOD

Element	Calibration Method	Estimated Accuracy (\pm %)
Lutetium	Relative 4π ^a	5
Europium	Relative 4π ^a	5
Indium (n, γ)	Known flux ^b	13
Gold	Standard flux; β - γ coincidence	4
Samarium	Relative 4π ^a	5
Tungsten	Known flux ^b	23
Lanthanum	Known flux ^b	16
Cadmium	Relative 4π ^a	5
Manganese	4π	5
Copper	4π	5
Phosphorus	4π	5
Indium (n,n')	4π	5
Aluminum (Al matrix)	Relative	5
Aluminum (Al foil)	β - γ coincidence	3

^aSpecial pellets made with aluminum sulfate

^bIn pneumatic tube of Ground Test Reactor

BLANK PAGE

3. EXPERIMENTAL EQUIPMENT

3.1 Aerospace Systems Test Reactor

The ASTR is a heterogeneous, enriched, light-water-moderated and -cooled thermal reactor. The design is roughly that of a right-circular cylinder 76 in. in length and 34 in. in diameter. The core is composed of twenty-nine fuel elements containing 155 g each of uranium-235, four elements containing 104 g each of uranium-235, and three control-rod assemblies. The fuel elements are arranged in a 7 x 7 matrix with the three elements in each corner missing. Aluminum grid plates support the core at each end. The grid plates are bolted inside a cylindrical pressure vessel constructed of 3/8-in. stainless steel.

The ASTR lift-tilt mechanism has a 12.5-in.-diam 15-ft-stroke hydraulic ram with a yoke attached to the top of the ram. The reactor is supported by trunnion fittings in the yoke and can be positioned either forward-end up or forward-end down by means of two hydraulic jacks on the yoke. The reactor can also be rotated 180° in either direction.

The ASTR tank is 17.5 ft in diameter and 17 ft deep, 16.5 ft of which is below grade level. The top of the tank is flanged to accept a variety of upper-tank configurations. For the experiments reported here, the upper tank was a 3-ft extension, open at the top but crossed by two heavy, parallel I-beams.

3.2 ASTR In-Pile Tube

The ASTR in-pile tube, located in core lattice position 0-3 (Figs. 4 and 5), is 4 in. in outer diameter with a nominal wall thickness of 0.125 in. It is constructed of 304 stainless steel. The bottom of the tube is closed by a 0.125-in.-thick welded plug, and the top closure or attachment is made by a Marmon V-clamp with an O-ring seal. The tube is held in the reactor by an O-ring flange and two captive bolts.

The tube extends approximately 1.5 ft through the core into the aft plenum chamber. The upper, or forward, end of the tube extends 10 in. through the pressure plate. An aluminum extension tube 42 in. long was attached to the upper end by means of a Marmon clamp.

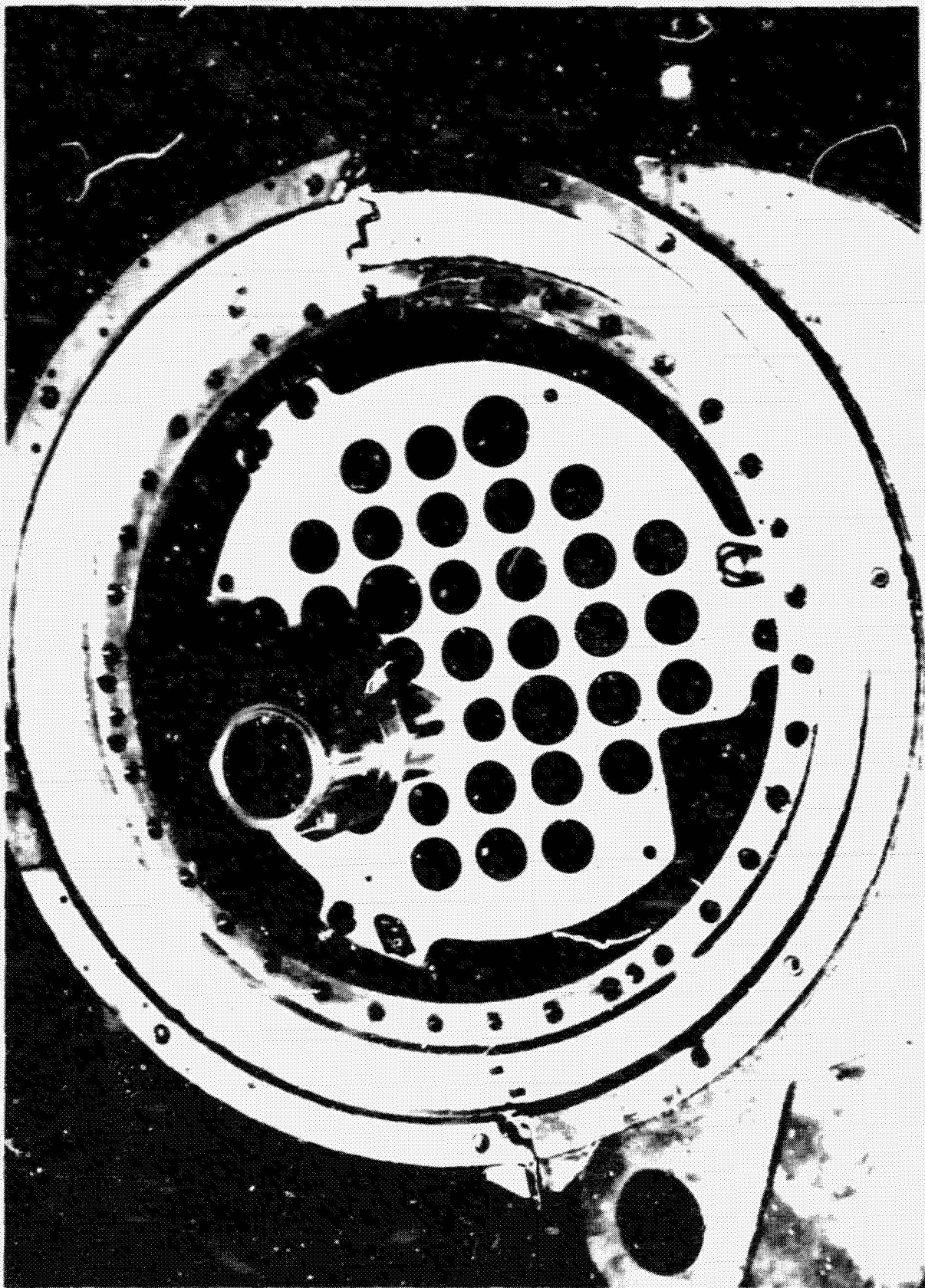


Figure 4 In-Pile Tube Inserted in Reactor Grid Plate

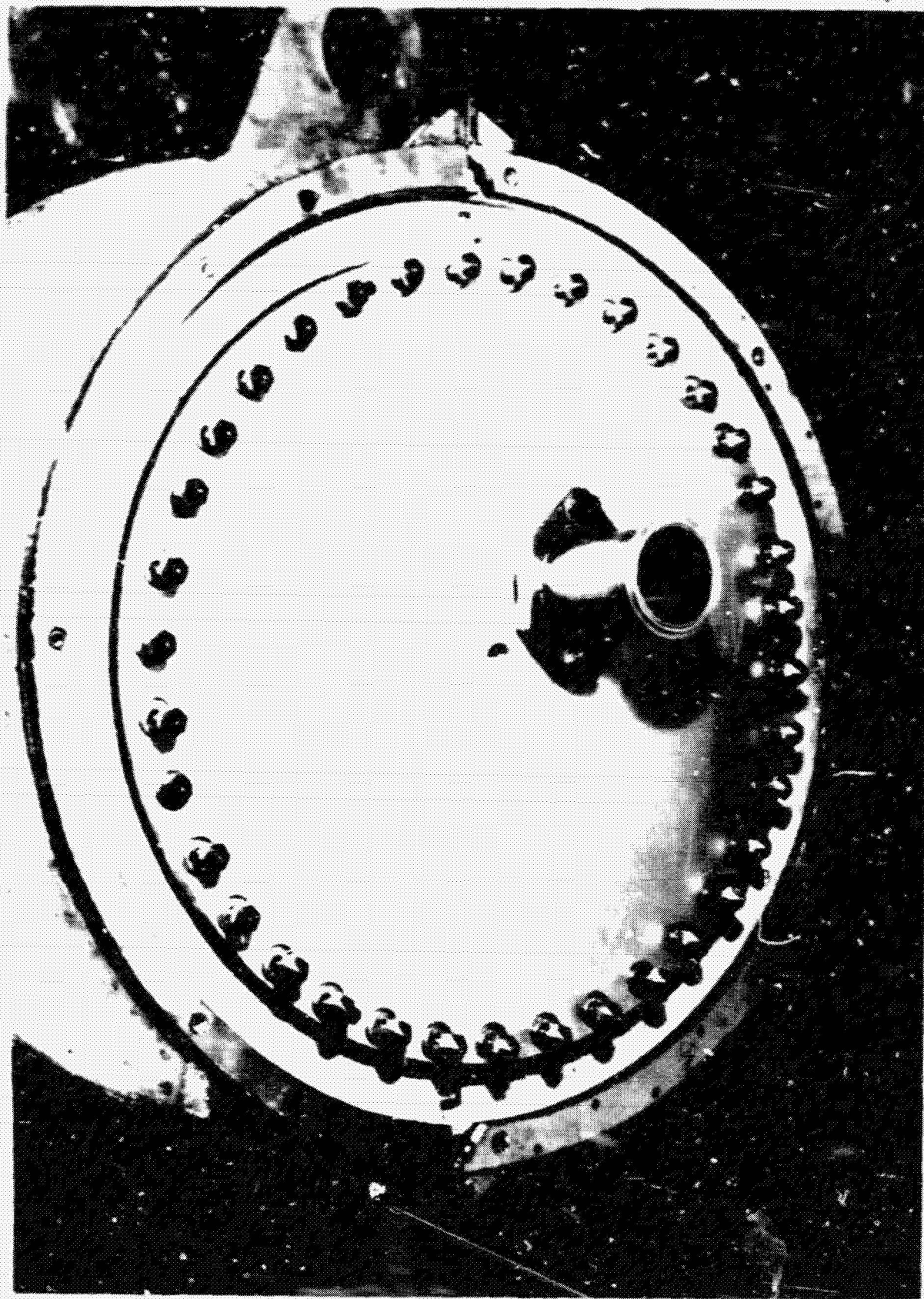


Figure 5 In-Pile Tube Extending Through Forward Pressure Plate

For these experiments the ASTR was in the fully lowered position with the forward-end up. The extension tube extended upward and terminated 3 ft below the water level of the extension tank. The test fixtures were installed by raising the reactor until the extension tube was above the water line; the test fixture was then inserted and fastened with a Marmon clamp and the reactor lowered to the full-down position. Removal of the test fixtures was achieved in the reverse sequence.

3 3 Calorimeter

The calorimeter (Figs. 6 and 7) employs an aluminum probe mounted on a water-cooled heat sink and otherwise thermally isolated by vacuum. Thermocouples were mounted in the stem at the bob and near the heat sink to measure the temperature gradient required in Equations 5, 6, and 7 (Sec. 2.1.1).

The calorimeter section proper is about 6 ft long and consists of the detector head supported by three cooling-water lines, a vacuum line (spot-welded to one of the cooling-water lines), and two thermocouple extension cables. Each line terminates with a fitting and each cable with a plug. The extension cables are stainless-steel-jacketed and each contains four 24-gage wires insulated by magnesium oxide.

The probes (several were made) were machined from both 1100 aluminum and from bar stock cast at the Metallurgical Laboratory from an ingot of Reynolds aluminum. The analysis provided with the ingot showed a composition of 99.79% Al, 0.07% Si, 0.13% Fe, and 0.01% Ga. The bar-stock castings were x-rayed (two angles) and tested ultrasonically; those showing defects were rejected.

After machining, the probes were again x-rayed, weighed to 1 mg on a microbalance, and the dimensions obtained. The dimensions were measured with a micrometer to the nearest mil and with a traveling microscope calibrated to 0.0001 in. From the dimensions and weight, the density of the probe used in these experiments was computed to be 2.71 g/cm³.

The thermocouples were mounted in drilled holes 0.013 in. in diameter and 0.020 in. deep. After insertion of the thermocouple lead, the walls of the hole were pressed in to hold the wire in place. Four thermocouples were initially mounted in the probe, but because of a break in one of the feedthrough

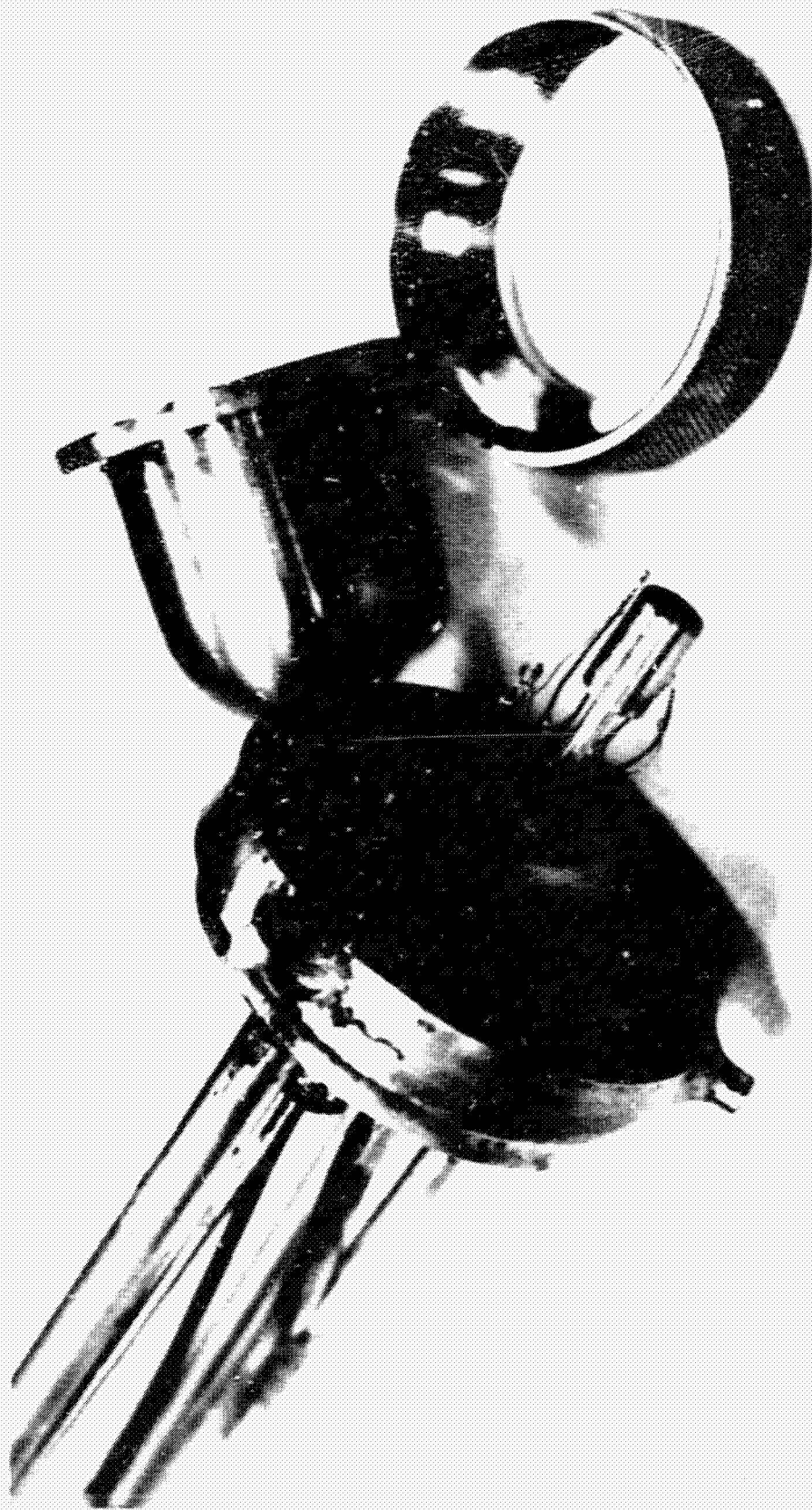


Figure 6 Calorimeter with Vacuum Dome Used in Irradiation

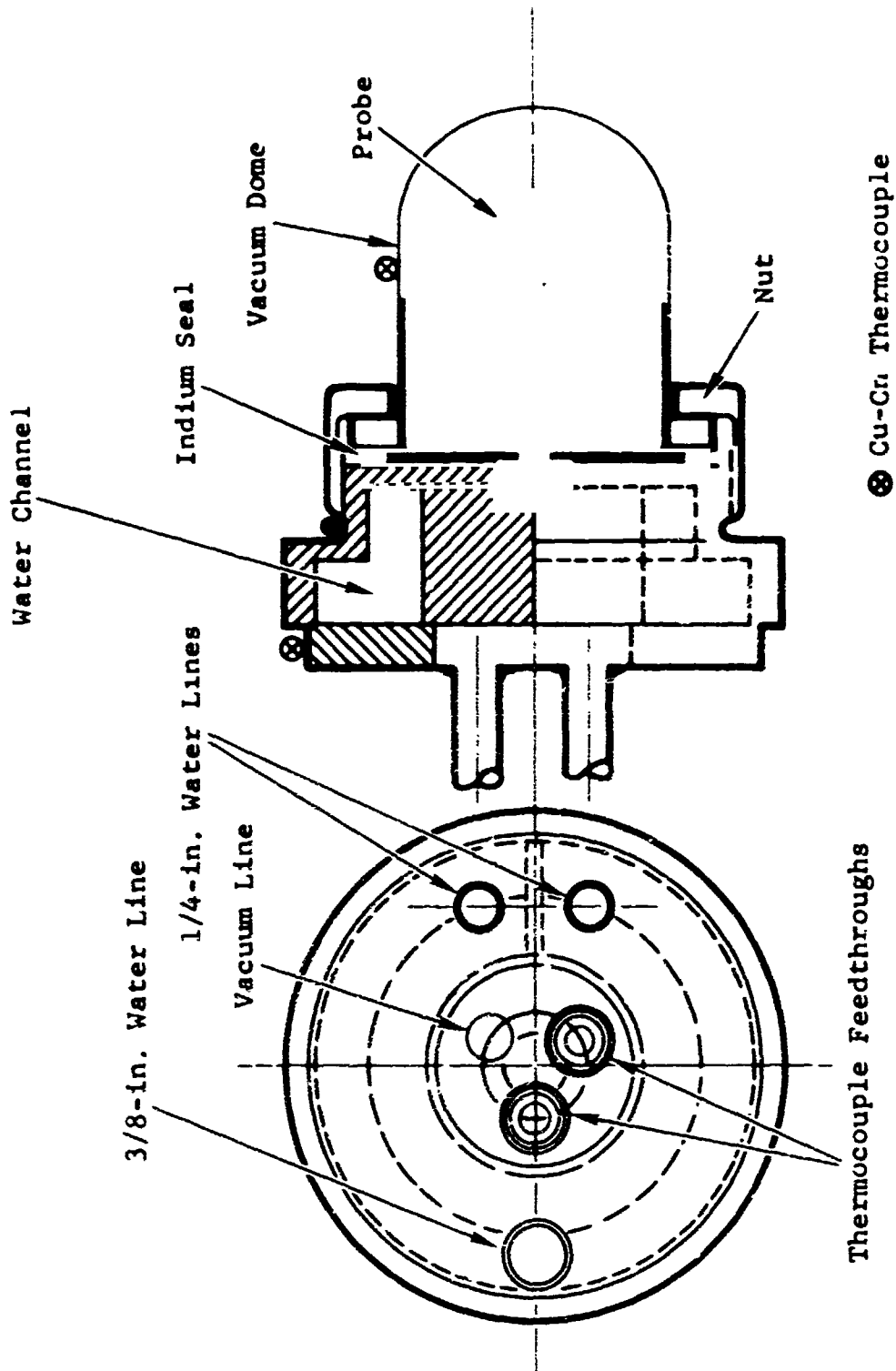


Figure 7 Sketch Showing Details of Calorimeter

wires which could not be repaired, one pair of thermocouples was removed prior to the irradiation test.

The thermocouples were made by spot-welding crossed wires of 36-gage (0.0050-in.-diam) chromel and alumel. The 36-gage wires were wrapped around and soldered to the 24-gage (0.020-in.-diam) wires extending into the vacuum chamber (Fig. 6) from the two thermocouple extension cables. The two sheathed cables were passed through the heat sink by means of Swagelok fittings. Thermocouple plugs were attached to the free end of the sheathed cables. The leads from the plugs to the reactor control room were made of 17-gage chromel-alumel extension wires (2 conductor) with polyvinyl insulation.

Six of the 36-gage chromel-alumel thermocouples were prepared and calibrated at the General Dynamics Standards Laboratory. The resulting correction curve, based on six temperature points, is shown in Figure 8. There was no appreciable difference in output among the six thermocouples. At the highest heating rate encountered in the irradiation experiment, the error in the differential temperature was 0.6°F in 93°F, or 0.65%.

Provisions were made for investigating the performance of the calorimeter by use of an electric heater and an oversize vacuum dome. With the calorimeter in irradiation configuration, a 30-W cartridge-type electric heater was mounted on the bob of the probe by means of a length of split aluminum tubing (see Fig. 9). The large vacuum dome with the heater wires entering through a vacuum feedthrough was then screwed down against an O-ring seal.

Figure 10 shows the calorimeter in the checkout configuration with an early instrumentation setup. In checking out the final probe assembly, the thermocouple outputs were read with a Leeds & Northrup K-4 Potentiometer Facility, heater current and voltage were read with Hewlett-Packard 412-B meters, and the thermocouple reference was a Joseph Kaye Labs Reference Junction. Pressure in the vacuum system was measured with a thermocouple gage at a point in the vacuum line about 5 ft from the chamber.

3.4 Ion Chamber

The ion-chamber fixture can be used interchangeably with the calorimeter by removing one and attaching the other

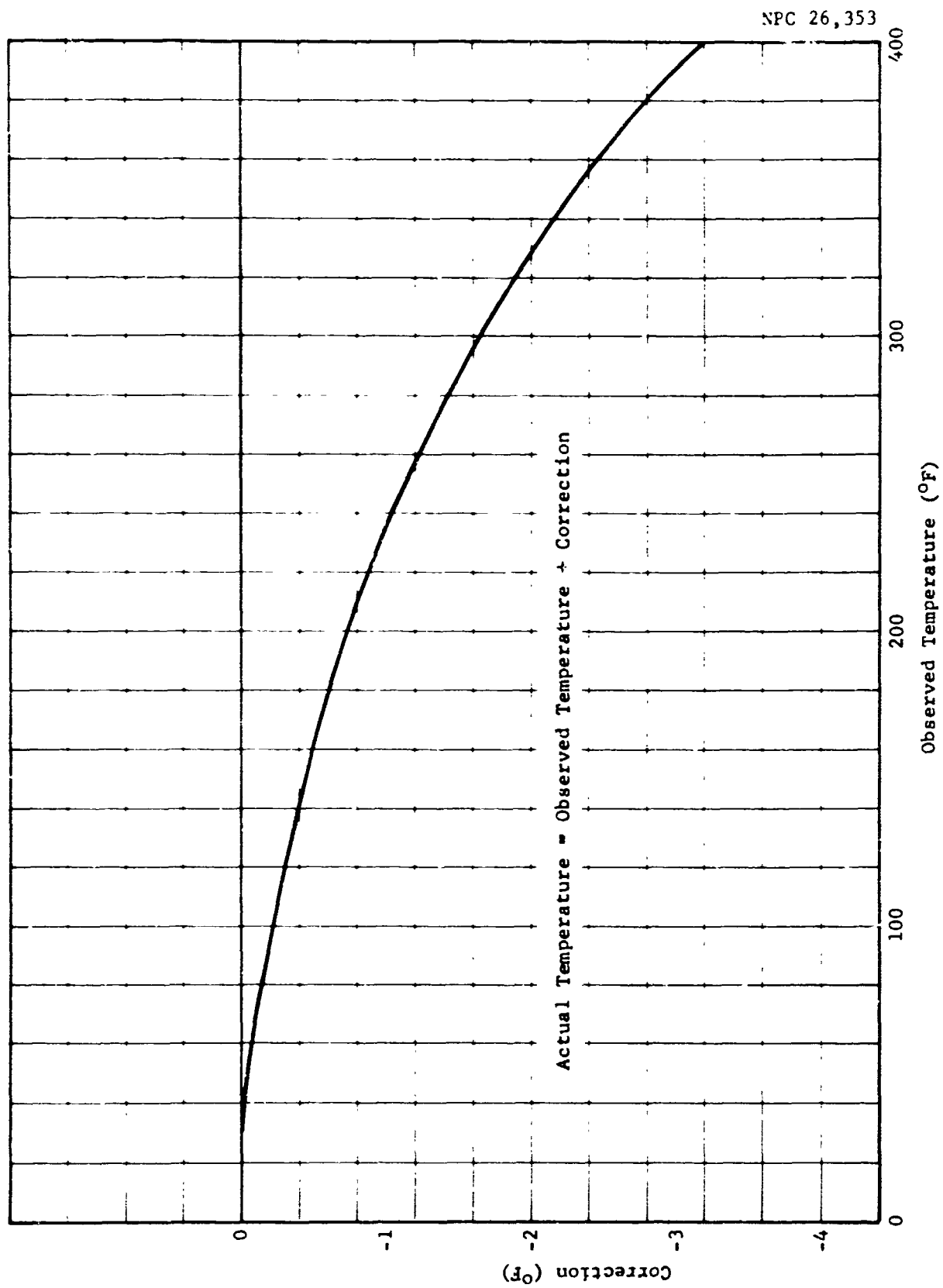


Figure 8 Chromel-Alumel Thermocouple Error Curve



Figure 9 Calorimeter with Calibration Heater Installed

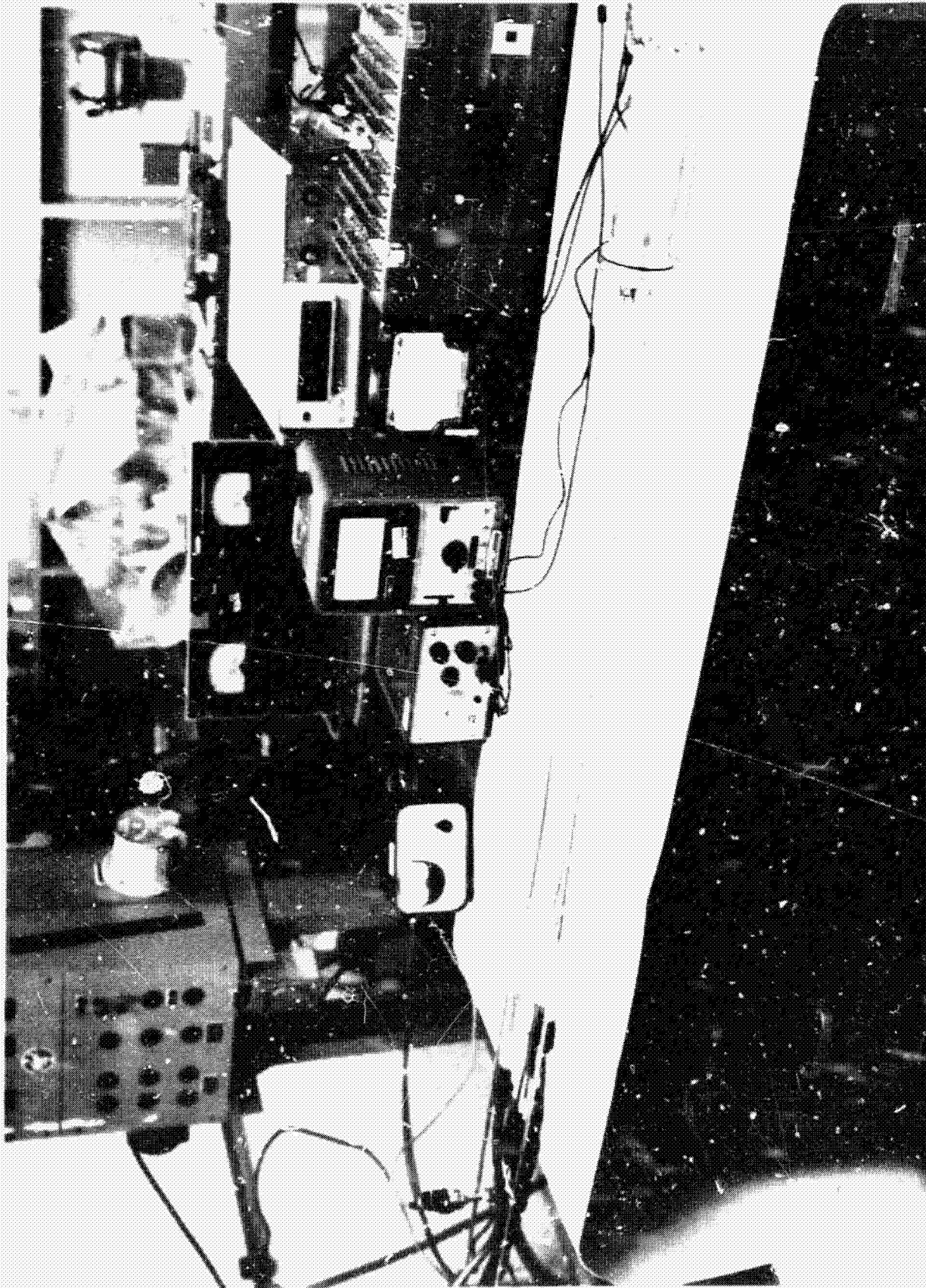


Figure 10 Calorimeter Calibration Setup

to the traversing mechanism. The ion chamber is supported by a mounting bracket attached to three aluminum rods, as shown in Figure 11. A 0.25-in.-copper water line coiled around the ion-chamber dome provides a heat sink. The coaxial cables plug into Microdot 32-31 cable connections on the base of the ion chamber.

The 4-cc ion chamber is based on a flow-chamber design by R. K. Able of Oak Ridge National Laboratory (Ref. 9). The chamber is modified from the original design in that it is a static chamber, being filled with CO_2 at a pressure of 1 atmosphere, and has an aluminum dome 0.025 in. thick instead of a plastic shell. The electrode arrangement has been retained - the outer graphite high-voltage electrode is 0.25-in. thick and is separated from the signal electrode by a 0.125-in. gap, resulting in a CO_2 -filled volume of 4 cc.

The ion-chamber current was read by means of a precision picoammeter driving a 0-10-mV recorder.

3.5 Traversing Mechanism

In order to map axially along the in-pile tube, a rack-and-pinion traversing mechanism with a servo position indicator was used. A 3-phase motor was used to drive the rack in either direction at 146 in./min; a continuous traverse through the 24-in. reactor core could be made in approximately 10 sec. The position indicator allowed the detector to be stopped at any position between full-up and full-down, with position read-out to 0.1 in. on a digital counter. Full travel of the rack was 22.3 in.

In order to keep gases in the in-pile tube from escaping to the atmosphere, the connection between the rack and the calorimeter (or ion chamber) fixture was made by means of a 1.5-in. diam tube sliding through a double O-ring seal in a flange; the flange was attached to the extension tube with a Marmor clamp. The water lines, vacuum line, thermocouple wires (four chromel-alumel and five copper-constantan), and coaxial cables were run through the tube and potted.

3.6 Foil and Dosimeter Fixtures

The irradiation fixture for the foil and gamma-dosimeter mapping, as shown in Figure 12, comprises a cage and an

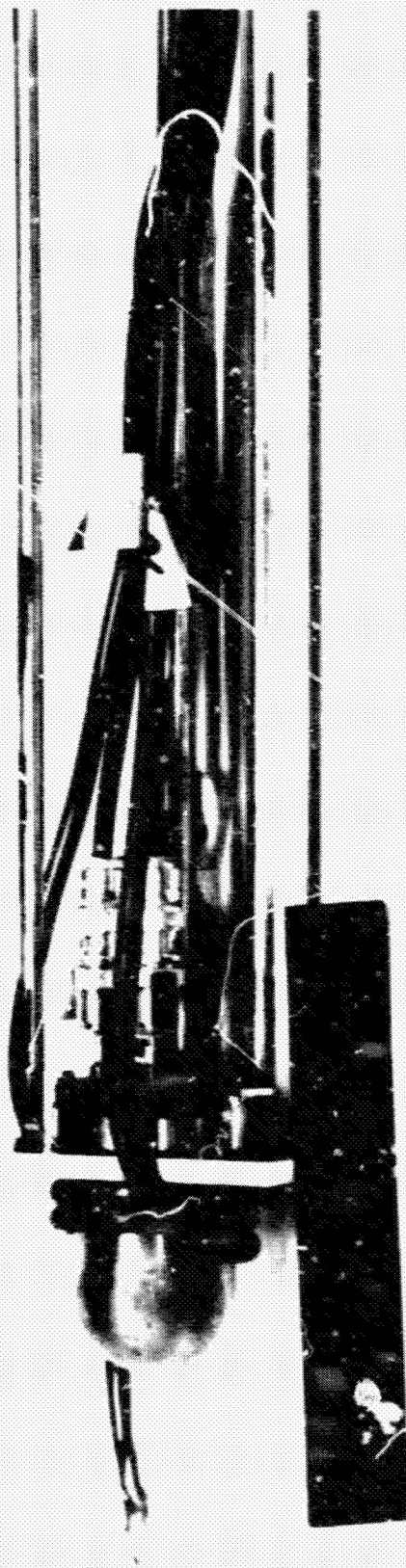


Figure 11 Ion Chamber in Irradiation Configuration

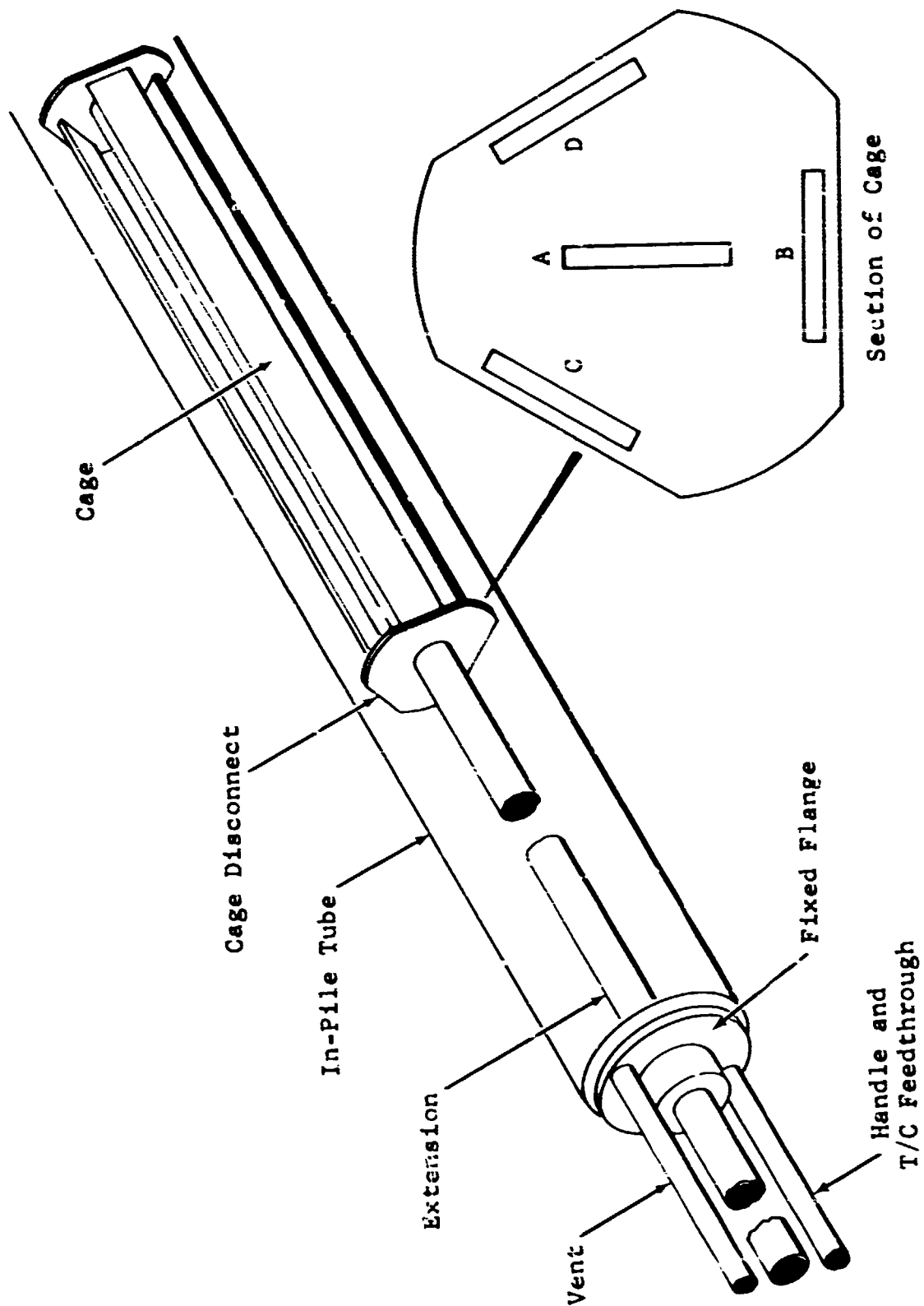


Figure 12 Sketch of Foll and Dosimeter Fixture

extension assembly. The cage consists of end plates joined by four stringers ($1/8 \times 1\frac{1}{2} \times 36$ in.) of perforated aluminum. One of the stringers is positioned along the centerline and the other three are spaced 120° apart on a circle of 1.25-in. radius. The foils and dosimeters were attached directly to the stringers with tape.

The extension assembly, to which the cage was attached by means of three studs and wing nuts, mates to the top of the extension tube by means of a flange and Marmon clamp. A tube welded to and extending through the flange served as a handle and thermocouple feedthrough. Another tube welded to the flange served as a vent line which doubled back under water.

A separate fixture, called the perturbation fixture, was fabricated to simulate the transducer test fixture (Ref. 1). This fixture (Fig. 13), which was interchangeable with the foil and dosimeter cages, was constructed of a spare aluminum manifold block and two tubes and a channel to simulate gaseous-coolant passages.

The detector positions on the foil and dosimeter fixture were defined by designating the stringers as A, B, C, and D, as shown in Figure 14. Since the transducer manifold boss positions were 2.5 in. apart, detector positions were made 2.5 in. apart and numbered starting at the bottom. Position No. 6 was made to correspond to the reactor centerline. The transducer manifold was also centered in the reactor core so that positions corresponded on both fixtures. For example, position 6A was at the center of the in-pile tube and on the centerline of the reactor core.

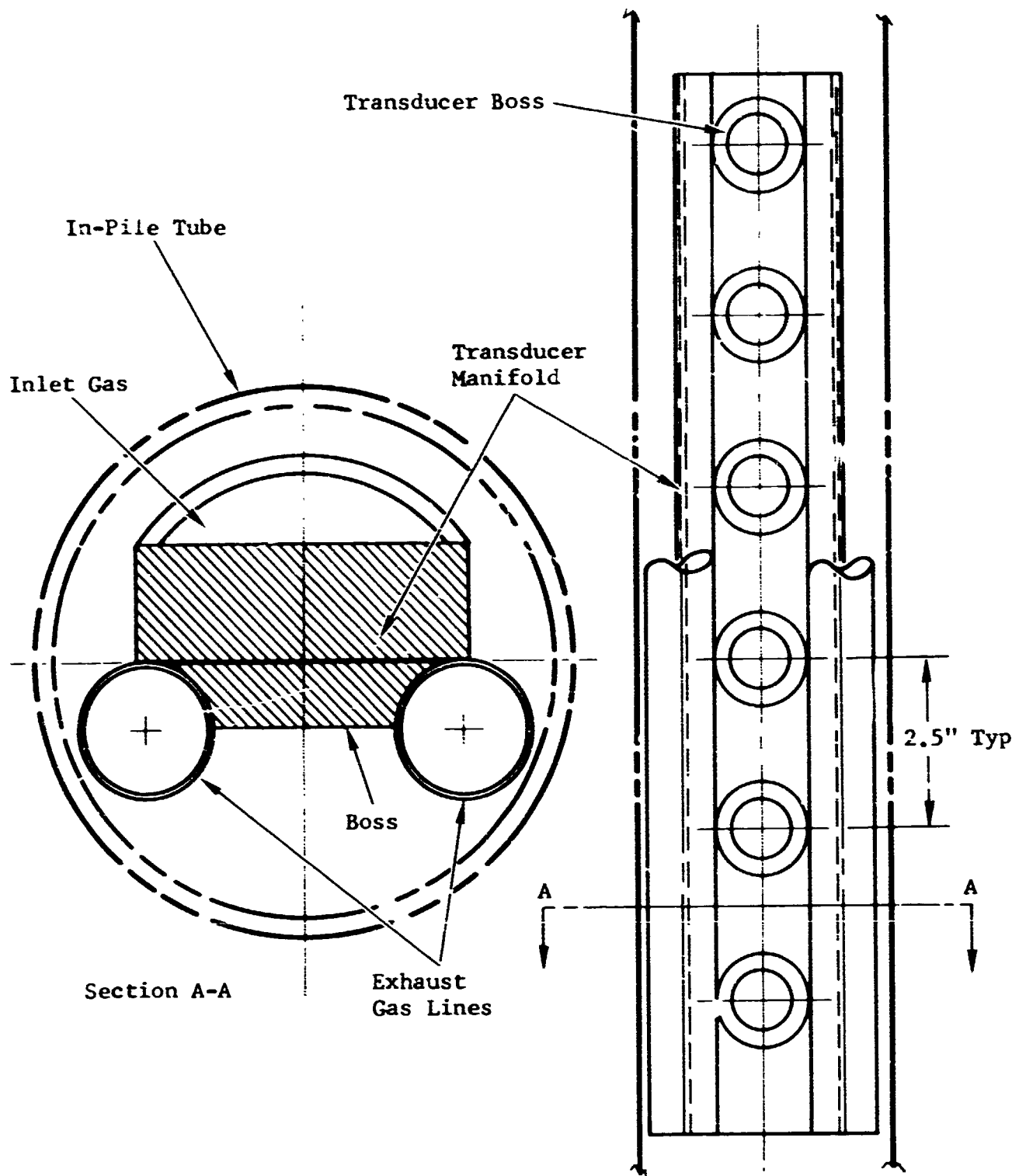


Figure 13 Sketch of Perturbation Fixture

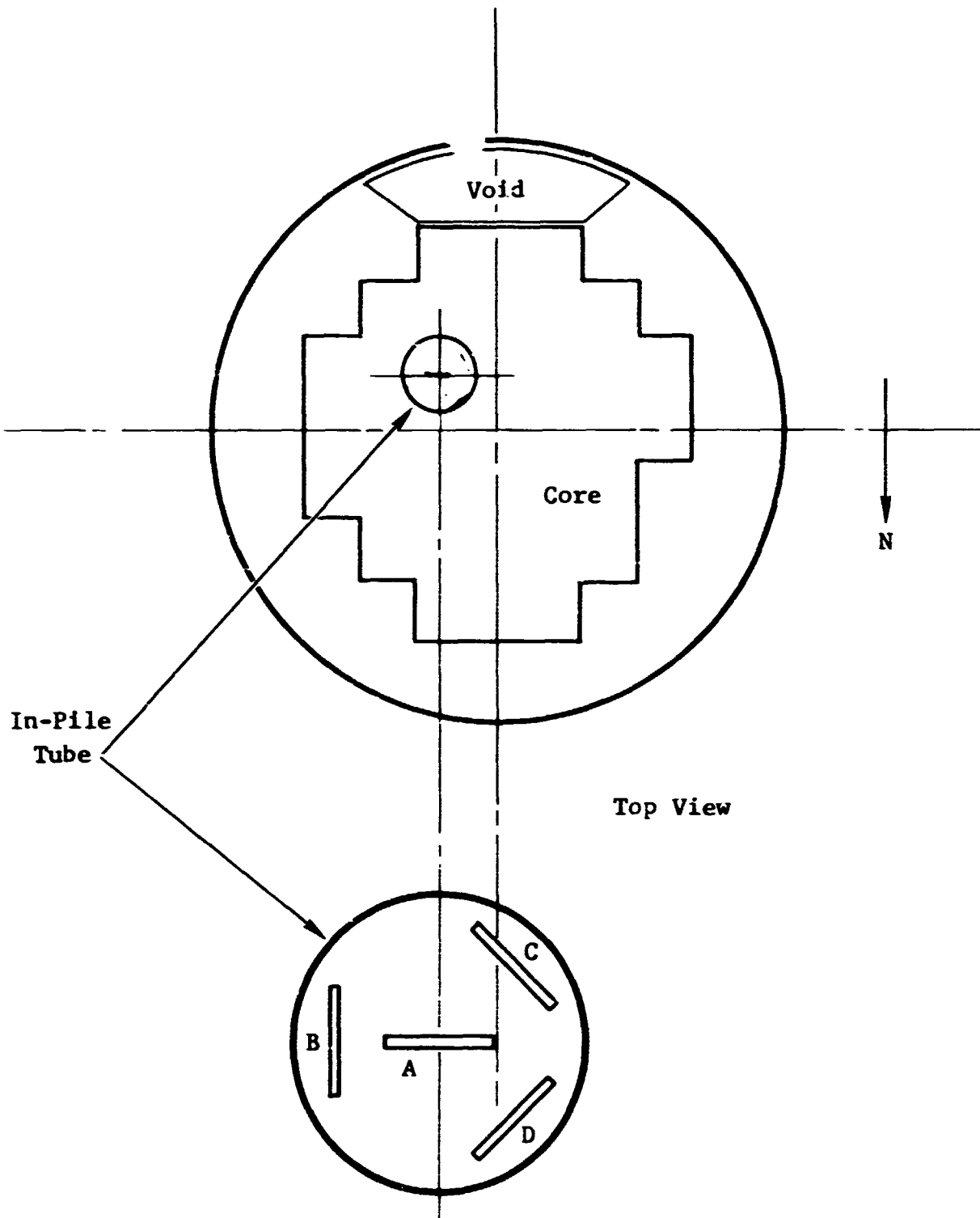


Figure 14 Sketch Showing Orientation of Foil and Dosimeter Fixtures in the Reactor Core

4. IRRADIATION PROCEDURES

The irradiations are described in the sequence in which they were conducted, namely, foils and dosimeters, ion chamber, and calorimeter. This sequence proceeded from the highest to lowest detector sensitivity so that the power levels could be ordered from lowest to highest.

4.1 Foils and Dosimeters

Six 30-min irradiations of neutron-detecting foils and gamma dosimeters were conducted on May 23 and 24, 1967. Reactor power levels were zero (core background), 45.5 W, 455 W, and 1.65 kW (three times). With the exception of zero power run, the time between insertion and removal of the detectors from the reactor ranged from 1.2 to 1.8 h. Orientation of the fixture in the reactor core was as sketched in Figure 14.

Temperatures were monitored at five locations during each irradiation, but only slight temperature rises occurred.

The reactor power levels are based on a calibration performed on 31 May 1967 in which a heat balance at 3 MW was correlated with the ion-chamber settings used during the irradiations.

4.2 Ion Chamber

The ion-chamber experiment was performed on 25 May 1967. Several traverses were made through the core at each of the following power levels (again based on the 31 May calibration): 0.455 W, 1.65 kW, 16.5 kW, 33 kW, 91.1 kW, 122 kW, and 165 kW. At 165 kW, the maximum dose rate approached the nominal upper limit of the ion chamber.

Cooling water for the ion chamber was supplied by a small gear pump mounted at the edge of the reactor pool. A suction line drew water from the pool, and the discharge line from the test fixture returned the water to the pool.

Temperatures were monitored at five locations - two on the ion chamber dome, two on the base, and one on the coaxial

cables. Ambient temperature in the in-pile tube before irradiation was about 80°F; the maximum temperature recorded was 102°F during the 165-kW run.

4.3 Calorimeter

The calorimeter measurements were made on 22 June 1967. Because of the time to reach temperature equilibrium (10-15 min), data were obtained only at selected locations in the tube, mainly near the center of the core. The power levels and positions at which data were obtained are shown below:

<u>Time</u>	<u>Power Level</u>	<u>Position</u> <u>(in. from top of core)</u>
1056	0.273	11.3
1109	0.455	11.3
1121	0.909	11.3
1135	1.89	0.2, 2.4, 4.6, 7.5, 11.3, 14.5, 18.4, 20.5, 22.6
1353	4.52	11.3
1422	6.78	0.2, 11.3, 22.6
1517	9	None
1518	0	None

Pressure in the vacuum system was monitored throughout the irradiation. The thermocouple gage was located in the 0.25-in. vacuum line above the water level, or about 12 ft from the calorimeter head. Approximately 12 ft of 0.50-in. tube extended from the gage to the vacuum pump, a 140 liter/min Welch 1402. Indicated pressure at the beginning of the irradiation was 35 microns and stayed at about that value through the 0.909-MW run. At 1.89 MW the pressure initially increased to 48 microns but rather quickly reduced to 40 microns and, after about one hour, decreased to 34 microns. At 4.52 MW the pressure was 58 microns, and at 6.78 MW the pressure varied between 40 and 80 microns, depending upon the position of the calorimeter in the core. When the power level was increased to approximately 9 MW, a rather rapid increase in pressure indicated a leak in the vacuum system and the test was terminated.

A subsequent inspection of the calorimeter indicated that the leak was probably around the Swagelok fittings used as the thermocouple feedthroughs. Because these fittings could not be made vacuum tight, they had been potted with epoxy; at 9 MW the epoxy apparently softened enough to allow the leak to develop.

Three copper-constantan thermocouples were placed on the outside of the calorimeter - one (T/C 1) was wired to the side of the dome, one (T/C 2) was clamped between the heat sink and dome nut, and one (T/C 3) was wired to the base of the heat sink (see Fig. 7). The maximum temperatures recorded at each of these locations are given in Table 6.

Table 6

MAXIMUM EXTERNAL CALORIMETER TEMPERATURES^a

Power Level (MW)	Maximum Temperature (°F)		
	T/C 1	T/C 2	T/C 3
0	90	90	90
0.273	94	91	97
0.455	98	94	100
0.909	106	97	103
1.89	124	101	116
4.52	158	103	123
6.78	166	108	128
9	201	113	124

^aAt position of maximum heating rate

Cooling water was supplied at approximately 40 psi by a small gear pump drawing water from the reactor tank.

BLANK PAGE

5. RESULTS

5.1 Calorimeter

Most of the calorimeter data were obtained by positioning the probe near the centerline of the reactor core and measuring the equilibrium temperature differentials between thermocouples on its stem for various reactor power levels. In addition, a profile of the temperature differential in the in-pile tube was obtained during a 1.89-MW run from nine different probe positions. Measurements were also made at the centerline and two extreme positions for reactor powers near 7 MW.

The calorimeter data for the different reactor powers and probe positions are listed in Table 7. These data consist of the electromotive forces developed by the chromel-alumel thermocouples, their equivalent temperatures (obtained through use of the thermocouple reference tables in Reference 10), and the resulting steady-state temperature differentials. These are the fundamental input data for all calorimeter calculations and will be used for reporting results in terms of both nuclear heating rates (in aluminum and carbon) and gamma dose rates.

5.1.1 Nuclear Heating Rate

5.1.1.1 In Aluminum

The nuclear heating rates in the aluminum probe are shown in Table 8 for the various reactor powers and probe positions. The uncorrected rates were obtained by substituting the ΔT 's from Table 7 into Equation 5. These were then divided by the reactor power in MW to obtain the heating rate per unit power. The corresponding rates corrected for heat losses were obtained from Equation 11, with slight additional corrections being made for convective heat losses at the three highest powers. These heating rates in aluminum are the most fundamental results from the calorimeter experiment and require interpretation only with respect to corrections for heat losses through means other than conduction down the stem of the probe.

It is felt that heat losses through radiation for reactor power levels of 1.89, 4.52, and 6.78 MW might be as high as 1, 1.7, and 3.2%, respectively, at the centerline of the reactor.

Table 7
CALORIMETER ΔT DATA

Reactor Power (MW)	Distance ^b (in.)	EMF ₁ ^a (mV)	EMF ₂ ^a (mV)	T ₁ ^a (°F)	T ₂ ^a (°F)	T (°F)
0.273	11.3	1.3435	1.2495	92.45	88.32	4.13
0.455	11.3	1.4546	1.2948	97.22	90.24	6.98
0.909	11.3	1.6968	1.3884	107.84	94.42	13.42
1.89	0.2	1.7417	1.4170	110.06	95.57	14.49
	2.4	1.9402	1.4942	118.51	99.14	19.37
	4.6	2.0756	1.5372	124.52	100.86	23.66
	7.5	2.2065	1.5872	130.22	103.24	26.98
	11.3	2.2464	1.6061	131.82	103.87	27.95
	14.5	2.1428	1.5798	127.42	102.98	24.44
	18.4	1.9961	1.5358	120.87	100.78	20.09
	20.5	1.8672	1.4909	115.36	99.03	16.53
	22.6	1.6737	1.3965	106.79	94.83	11.96
4.52	11.3	3.5938	2.1157	190.22	126.29	63.93
6.78	0.2	3.0188	1.9370	165.47	118.40	47.07
	11.3	4.6608	2.5062	236.54	143.21	93.33
6.94	22.6	2.9742	1.9726	163.67	120.09	43.58

^aThese results are averages of at least three independent readings of slight fluctuations about the equilibrium temperature, so that there is little chance for a significant reading error.

^bFrom top of core

Table 8

NUCLEAR HEATING RATES IN ALUMINUM

Reactor Power (Mw)	Distance ^a (in.)	Heating Rate (uncorrected)		Heating Rate (corrected)	
		(W/g Al)	(W/g Al-MW)	(W/g Al)	(W/g Al-MW)
0.273	11.3	0.073	0.267	0.073	0.267
0.455	11.3	0.124	0.273	0.124	0.273
0.909	11.3	0.238	0.262	0.239	0.263
1.89	0.2	0.256	0.135	0.258	0.137
	2.4	0.343	0.181	0.346	0.183
	4.6	0.419	0.222	0.423	0.224
	7.5	0.478	0.253	0.438	0.256
	11.3	0.495	0.262	0.500	0.265
	14.5	0.433	0.229	0.437	0.231
	18.4	0.356	0.188	0.359	0.190
	20.5	0.289	0.153	0.291	0.154
	22.6	0.217	0.115	0.218	0.116
	22.6	0.217	0.115	0.218	0.116
4.52	11.3	1.132	0.250	1.166	0.258
6.78	0.2	0.833	0.123	0.858	0.127
	11.3	1.652	0.244	1.735	0.256
6.94	22.6	0.771	0.111	0.794	0.114

^aFrom top of core

These estimates were obtained by multiplying the rough results of Table 1 by a factor of 6: 3 for the uncertainty in the emissivity of the probe ($0.1 \leq \epsilon \leq 0.3$) and 2 for neglect of the temperature distribution over the probe and its surrounding dome, that is, $C = 2$ in Equation 11. Moreover, the pumping system was not able to maintain as high a vacuum during the 4.52- and 6.78-MW runs, so that the pressure increased from a near constant level of 35 microns to 60 and 80 microns, respectively. Thus, convection losses might well amount to 1.2 and 1.7%, respectively, during these runs. Therefore, one might account for total heat losses of something like 1, 3, and 5% at the core centerline for reactor powers of 1.89, 4.52, and 6.78 MW, respectively.

These estimated heat losses of 1, 3, and 5% at the reactor centerline were plotted against the temperature differentials given in Table 7 for the powers in question, and the resulting curve, in conjunction with measured ΔT 's, was used to estimate heat losses at other probe positions during the 1.89-MW and 6.78-MW runs. These heat losses were then used to obtain the corrected heating rates of Table 8. The uncorrected and corrected heating rates of Table 8 for a probe position of 11.3 in. below the top of the core (near the reactor centerline) are plotted as Curves A and B in Figure 15.

It has long been thought that the nuclear heating rate in the in-pile tube of the ASTR should increase linearly in direct proportion with the reactor power. Curve C shows such a dependence based on data from low-power operations where heat losses are negligible. Since the uncorrected data of Curve A are too low for the higher powers, where heat losses are significant, it is thought that Curves A and C should bracket the true heating rate in the ASTR. Curve B, incorporating corrections for heat losses, represents an attempt to see how close Curve A can be made to approach Curve C if one assumes heat losses to be as large as can reasonably be justified from theory.

Curve B comes within about 3% of Curve C, and because of the uncertainty in estimating heat losses, particularly the convective component, it is quite possible that Curve C gives the best estimate of the true heating rate in the reactor. While one cannot rule out the possibility that the heating rate might increase less rapidly than Curve C at higher powers, it will be

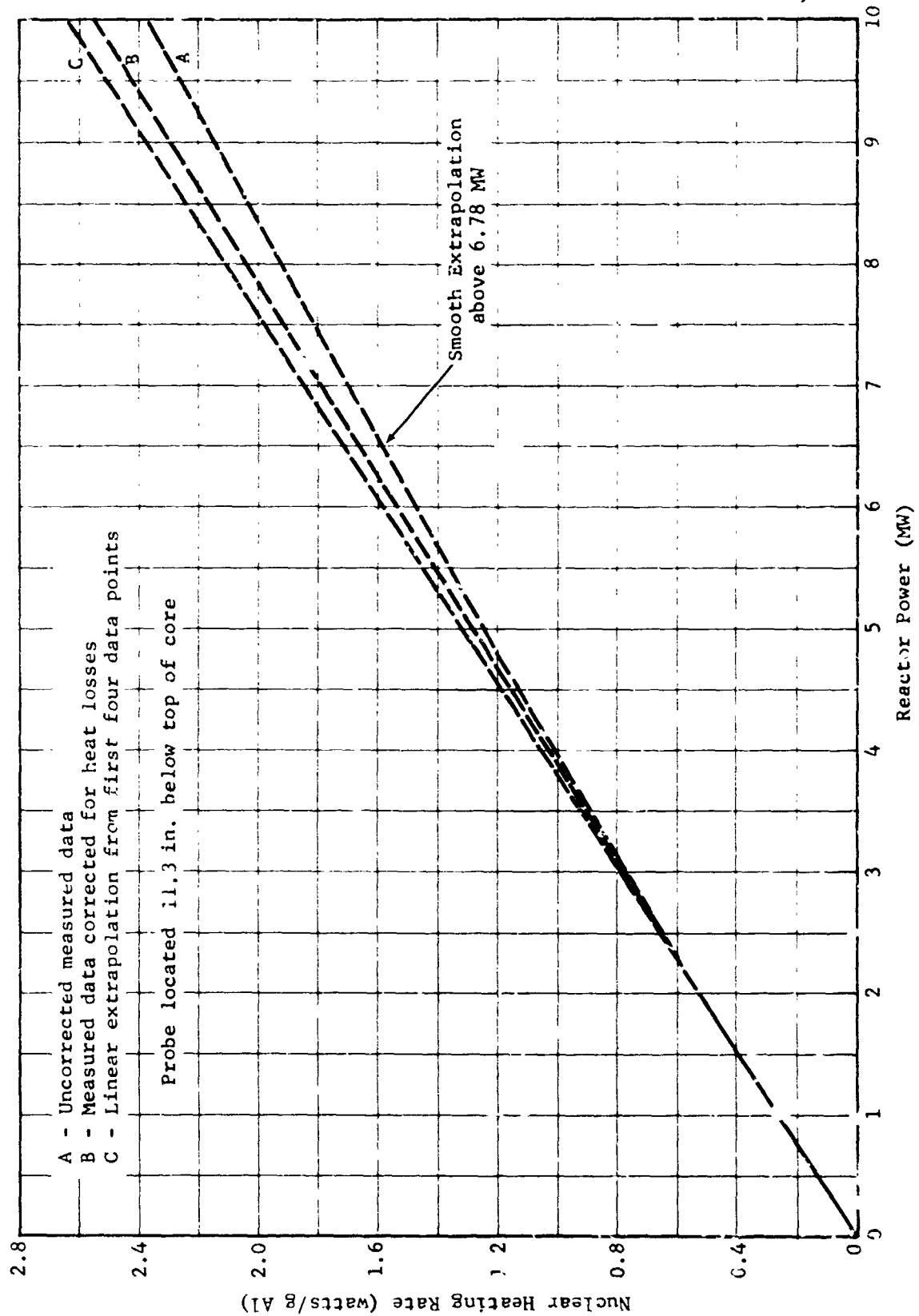


Figure 15 Heating Rate in Aluminum as a Function of Reactor Power Level

assumed for convenience hereafter that the centerline heating rate in aluminum can be obtained for any reactor power by multiplying the power in question by 0.265 watt/g Al-MW, the slope of Curve C in Figure 15

Therefore, the centerline data of Table 8 for any reactor power level of P (in MW) can be written in the compact form

$$q^*/P = 0.265 \text{ watt/g Al-MW}$$

and when converted to a dose rate this can be compared directly with ion-chamber and dosimeter data obtained at much lower power levels. Moreover, the corrected data of Table 8, giving $q^*(y)/P$ as a function of probe position y for a reactor power of 1.89 MW, can be multiplied by any other power to obtain a profile curve of $q^*(y)$ for that power, and these curves can be compared to strip-chart recordings of ion-chamber data obtained from continuous traverses through the core. These comparisons will serve to reinforce the assumption of a linear proportionality between heating rates and reactor power for all core positions, at least for powers below 2 MW. Hence, in summary, all of the corrected data of Table 8, as well as data for any other reactor power below 10 MW, can essentially be obtained from Curve A of Figure 16, which is a plot of $q^*(y)/P$ for aluminum.

5.1.1.2 In Carbon

The equivalent heating rates for a carbon sample, uncorrected for heat losses or differences in neutron heating, are obtained by substituting the ΔT 's from Table 7 into Equation 6, and, according to Equation 28, these heating rates can be corrected by multiplying the corrected heating rates in aluminum from Table 8 by a constant factor of 1.064. This latter multiplication adjustment is essentially equivalent to obtaining corrected results by substituting into Equation 29. These corrected and uncorrected heating rates for carbon are listed in Table 9, and the corrected rate per unit reactor power, $q_c^*(y)/P$, is plotted against core position as Curve B of Figure 16. The shapes of the heating curves for carbon (B) and aluminum (A) are the same, of course, since they differ only by the constant factor above.

The curves connecting the measured points of Figure 16 are the fourth-order, least-squares curve fit to the data, and coefficients for second, third, and fourth-order fits, along with

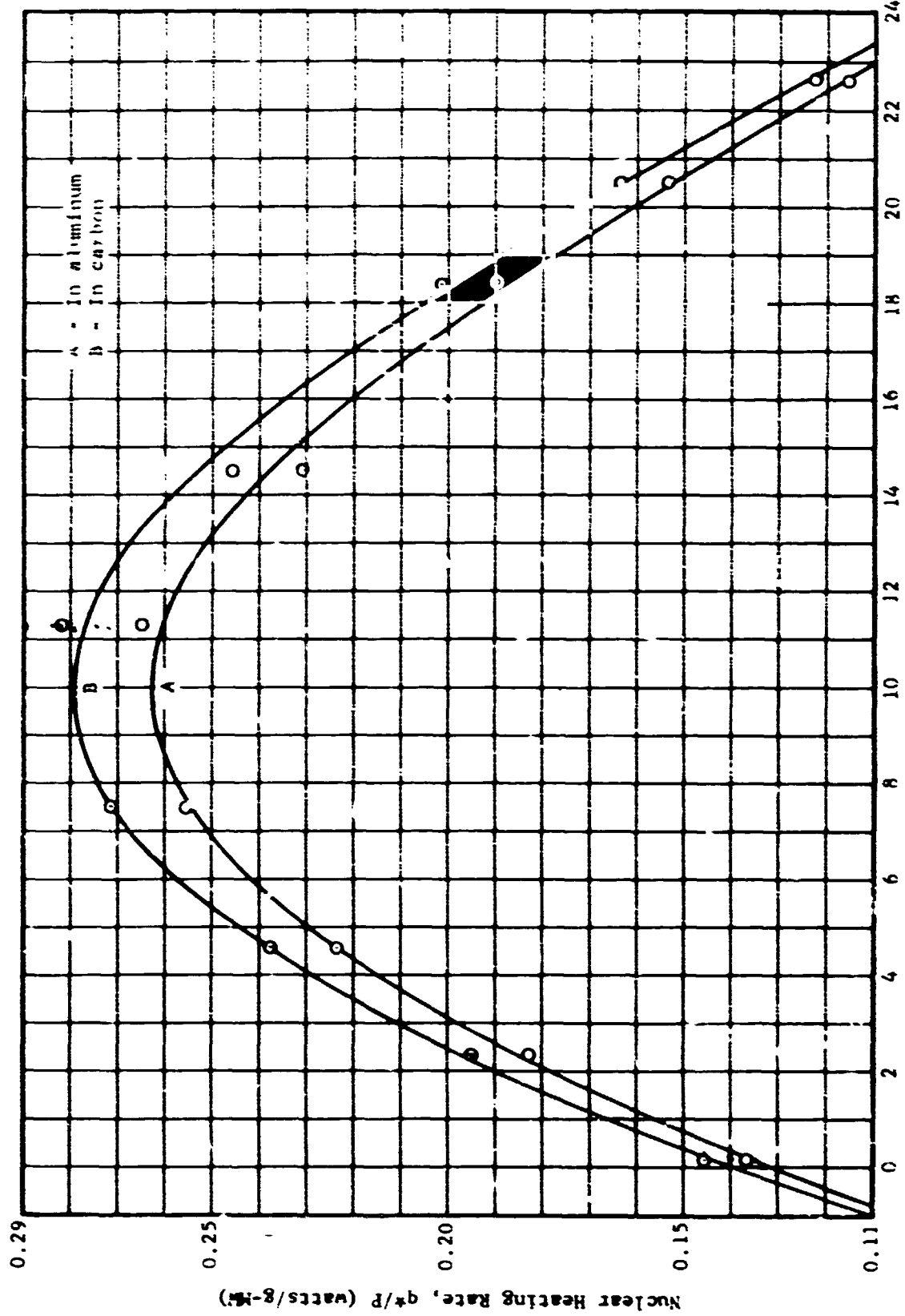


Figure 16 Heating-Rate Profile Through the ASTR Core

Table 9

NUCLEAR HEATING RATES IN CARBON

Reactor Power (MW)	Distance ^a (in.)	Heating Rate (uncorrected)		Heating Rate (corrected)	
		(W/g C)	(W/g C-MW)	(W/g C-MW)	(W/g C-MW)
0.273	11.3	0.076	0.278	0.078	0.284
0.455	11.3	0.128	0.281	0.132	0.290
0.909	11.3	0.247	0.272	0.254	0.280
1.89	0.2	0.267	0.141	0.275	0.146
	2.4	0.356	0.188	0.368	0.195
	4.6	0.435	0.230	0.450	0.238
	7.5	0.496	0.262	0.514	0.272
	11.3	0.514	0.272	0.532	0.282
	14.5	0.450	0.238	0.465	0.246
	18.4	0.370	0.196	0.382	0.202
	20.5	0.300	0.159	0.310	0.164
	22.6	0.220	0.116	0.232	0.123
	11.3	1.176	0.260	1.241	0.275
4.52	11.3	1.176	0.260	1.241	0.275
6.78	0.2	0.866	0.128	0.913	0.135
	11.3	1.717	0.253	1.846	0.272
6.94	22.6	0.802	0.116	0.845	0.121

^aFrom top of core

their standard deviations from the measured data, are given in Appendix B. In Figure 16, one observes a maximum normalized heating rate in carbon of 0.28 watt/g at a position 10 in. into the core. It is thought that the measured point at 14.5 in. into the reactor might be somewhat low, as will be discussed later, and this causes the least-squares curve to dip below the largest measured point at 11.3 in. Disregarding this doubtful point, the least-squares curve would reach a peak value of

$$q_c^*/P = 0.283 \text{ watt/g C-MW}$$

at 10.5 in., so that the maximum heating rate for 10-MW operation is expected to be 2.83 watt/g C.

5.1.2 Gamma Dose Rate

The dose rates in the ASTR, uncorrected for heat losses or neutron heating, are obtained by substituting the temperature differentials from Table 7 into Equation 7. These dose rates can be corrected, according to Equation 30, by multiplying the corrected aluminum heating rates (in watt/g) from Table 8 by a constant factor of 4.1×10^8 , with the results of this multiplication equivalent to a substitution into Equation 31. These corrected and uncorrected dose rates are listed in Table 10, and the dose rate per watt of reactor power is plotted against core position in Figure 17. The corrected and uncorrected dose rates do not differ by too much at the higher reactor powers because heat losses are just about offset by neutron heating.

The alteration in the profile curve brought about by omitting the questionable 14.5-in. point is shown by the dashed curve of Figure 17, which amounts to a correction of no more than 2% at any position. Here, the corrected dose rate per unit power reaches a peak of 109.5 R/h-watt, so that a maximum dose rate of 1.095×10^9 R/h is indicated for full-power ASTR operation of 10 MW. The coefficients for the least-squares curves of Figure 17 are listed in Appendix B. A full discussion of possible distortions in the dose-rate profile of Figure 17 will be reserved until similar data have been presented for continuous traverses of the ion chamber. The final dose-rate profile for the ASTR will be determined from a comparison of these data.

Table 10

GAMMA DOSE RATES COMPUTED FROM CALORIMETER DATA

Reactor Power (MW)	Distance ^a (in.)	Dose Rate (uncorrected)		Dose Rate (corrected)	
		(R/h $\times 10^{-6}$)	(R/h-W)	(R/h $\times 10^{-6}$)	(R/h-W)
0.273	11.3	31.1	113.9	29.9	109.5
0.455	11.3	52.6	115.6	50.8	111.6
0.909	11.3	101.2	111.3	98.0	107.8
1.89	0.2	109.3	57.8	105.8	56.0
	2.4	146.0	77.2	141.9	75.1
	4.6	178.4	94.4	173.4	91.7
	7.5	203.4	107.6	198.0	104.8
	11.3	210.7	111.5	205.0	108.5
	14.5	184.3	97.5	179.2	94.8
	18.4	151.5	80.1	147.2	77.9
	20.5	123.1	65.1	119.3	63.1
	22.6	90.2	47.8	89.4	47.3
	11.3	482.0	106.6	478.1	105.8
4.52	11.3	482.0	106.6	478.1	105.8
6.78	0.2	354.9	52.3	351.8	51.9
	11.3	703.7	103.8	711.4	104.9
6.94	22.6	328.6	47.3	325.6	46.9

^aFrom top of core

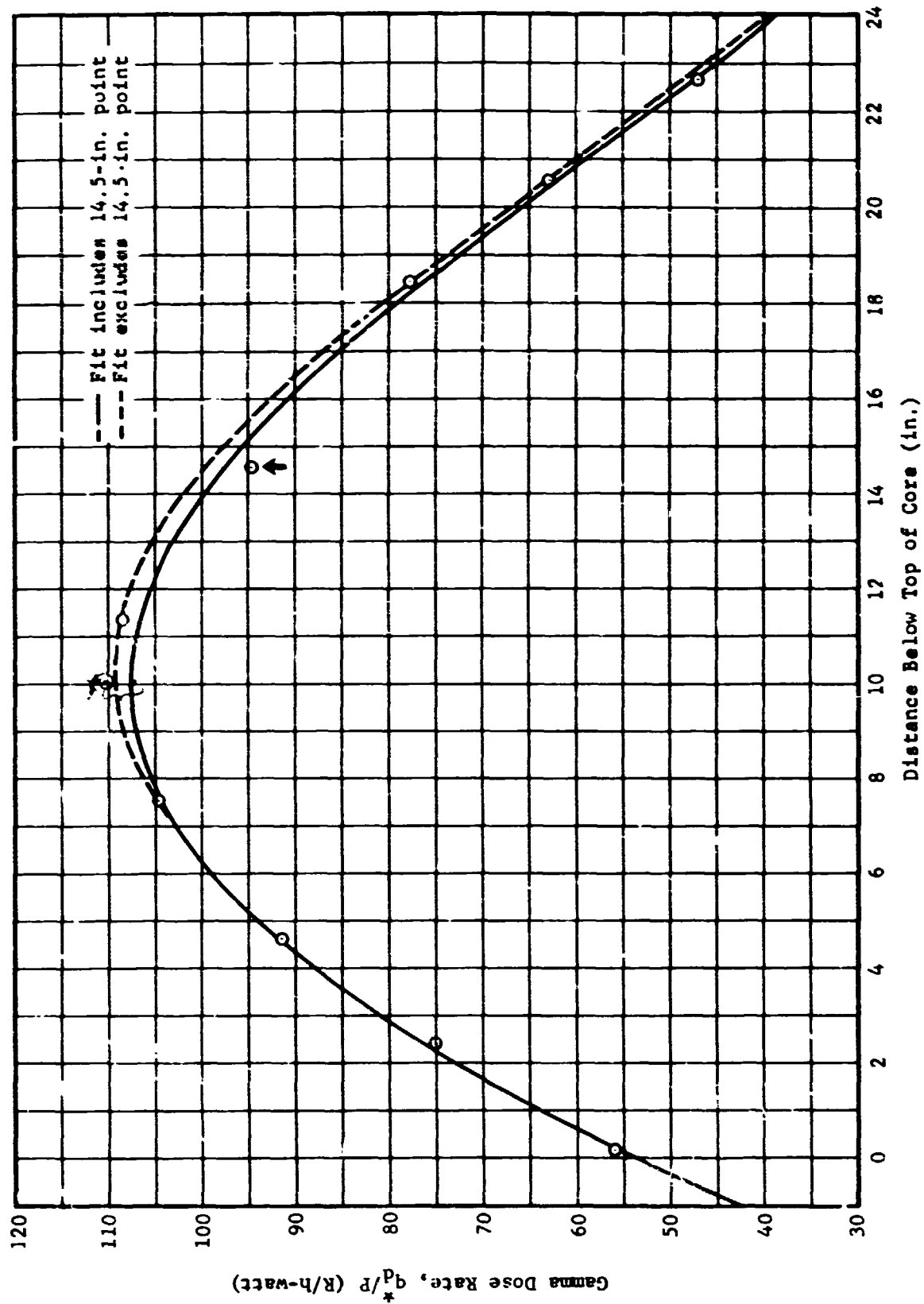


Figure 17 Gamma-Dose-Rate Profile as Determined from Calorimeter Data

5.1.3 Error Analysis

The various sources of error in the calorimeter measurements of nuclear heating rates and the maximum assigned uncertainties for a nuclear heating rate at the centerline of the core of about 1.8 watt/g Al, corresponding to a reactor power of 6.78 MW, are as follows:

<u>Source of Error</u>	<u>Uncertainties (+ %)</u>
Thermocouple accuracy	1.0
Distance between T/C's	0.2
Area of stem	0.5
Thermal conductivity of Al	1.5
Position in core	1.0
Correction for heat losses	3.0
Reactor power	3.0
Gamma attenuation	0.5
Spatial flux distribution	Negligible

$$\text{One standard deviation} = \sqrt{\sum \epsilon_i^2} = \pm 4.8\%$$

$$\text{Two standard deviations (95\% confidence level)} = \pm 9.6\%$$

The physical dimensions of the calorimeter probe were measured to the nearest 0.001 in.; an error of 1 mil in the critical dimensions, i.e., the area of the stem and the distance between the thermocouples, would result in the uncertainties given above.

The thermal conductivity of aluminum used in the calculations was taken from the NBS recommended curve (Ref. 2) for pure aluminum and has been arbitrarily assigned the uncertainty of 1.5%. The thermal conductivity of the actual piece of aluminum used for the probe was not independently determined; however, the probe was of high-purity aluminum and carefully prepared to avoid defects.

The detector position was indicated on a digital counter reading to 0.1 in. Since the indicated position at both the full-up and full-down stops was very reproducible, the error in position measurement should have been less than 0.1 in. Near the ends of the in-pile tube, where the flux gradient is greatest, an error of 0.1 in. in position would result in about 1.6% error in heating rate. At positions near the center of the tube

negligible error would result. The flux variation over the detector volume was small, and since the center of detection was taken as the center of the bob, the variation in flux should be effectively averaged.

The reactor power level computed from heat balances over many operations is considered to be within $\pm 3\%$, at least for megawatt power levels. For the calorimeter experiment, power levels for the 1.89-MW and higher power levels were computed from the reactor heat-balance measurements. The 0.909-MW and lower power levels, while set by reactor ion-chamber readings, were corrected (by 5%) on the basis of the ion-chamber readings and the heat balance at 1.89 MW. In other words, the experiment itself was used to calibrate the reactor ion chambers by the heat-balance method.

Accuracy of the thermocouples was determined largely by the conversion of output voltage to temperature and by the error in thermocouple output. The latter, which depends only on the temperature differential between the pair of thermocouples, was about 0.5% at the highest heating rate and decreased at the lower heating rates (see Fig. 8). The thermocouple output was read with an L & N type K-4 potentiometer to the nearest 0.1 μV (five significant figures). Of course, the lower the heating rate, the smaller the temperature differential to be determined. At the lowest heating rate employed, the difference in output between the thermocouples was 0.1940 mV.

As the reactor power level is decreased below a megawatt the uncertainty in the thermocouple accuracy will increase by only a few percent, thanks to the pedestal design of the calorimeter which gives relatively large temperature differentials for low heating rates. This loss of thermocouple accuracy along with a slightly increased uncertainty in reactor power at lower levels will just about be offset by a reduction of heat losses, so that the combined uncertainty above is not expected to change by very much over the whole range of heating rates. For a given power level, the uncertainty in heating rate measurements will increase somewhat for positions near the bottom of the reactor core because of gamma ray attenuation through the base of the calorimeter. At the full-down position, the combined uncertainty for a 6.78-MW operation might reach 12% at the 95% confidence level.

5.2 Ion Chamber

5.2.1 Gamma Dose Rate

The ion-chamber data were obtained mostly by continuous traverses of the detector through the core while recording the output of the picoammeter on a strip-chart recorder running at 1 in./sec. Several traverses of the core, from top to bottom and bottom to top, were made at each reactor power level. In addition, at each power level the detector was stopped 1 in. above the core center, the approximate location of the peak gamma dose rate, and a reading was obtained for a sufficient length of time to ensure a steady reactor power and to eliminate effects of lag in the chamber readout due to the relatively rapid rate of traverse; this procedure was used by approaching the center position from both the top and bottom of the core. Table 11 gives the dose rates, in R/h-W, measured with the chamber stationary at the full-up position (0.4 in. outside the core), 1 in. above the center of the core, and at the full-down position (2.1 in. from the bottom of the core). The data in Table 11 are corrected by 2.5% for neutron contributions to the dose rate (Sec. 2.2.2).

Examination of the data from the continuous scans revealed that the lag in readout introduced a shift of about 0.5 in. in the apparent position of the detector; this was corrected for in the following manner. Ion-chamber current output was tabulated from the charts for 1-in. increments for each of the power levels except 0.455 and 1.65 kW; tabulations were made for both top-to-bottom traverses and bottom-to-top traverses. The current readings were then converted to dose rate in R/h-W and averaged (see Appendix C).

The averaged data were then curve-fitted to a fourth-degree equation by use of a computer, and the coefficients of each term for the top-to-bottom and bottom-to-top traverses were averaged to obtain the equation for the gamma dose rate as a function of position in the core (see Appendix E). Finally, this fourth-degree equation was used to compute the dose rate as a function of position; the results appear in Figure 18. (Note that the average ion-chamber curve of Figure 18 does not include the 0.455- and 1.65-kW data.)

The gamma dose rate corrected for a 2.5% neutron contribution to the ion-chamber response is shown as the solid curve of

Table 11

GAMMA DOSE RATES MEASURED WITH ION CHAMBER^a

Power (kW)	Dose Rate (R/h-W)		
	Full Up	Maximum	Full Down
0	729 ^b	1980 ^b	842 ^b
0.455	53.5 ^c	113.1 ^c	61.0 ^c
1.65	50.6 ^c	111.0 ^c	58.4 ^c
16.5	50.0	108.9	56.0
33	51.7	108.8	57.7
91.1	52.7	109.2	58.5
122	51.5	110.5	58.7
165	49.7	107.4	56.3
Avg	51.4	110.2	58.1

^aCorrected for neutron contribution^bR/h^cCorrected for background

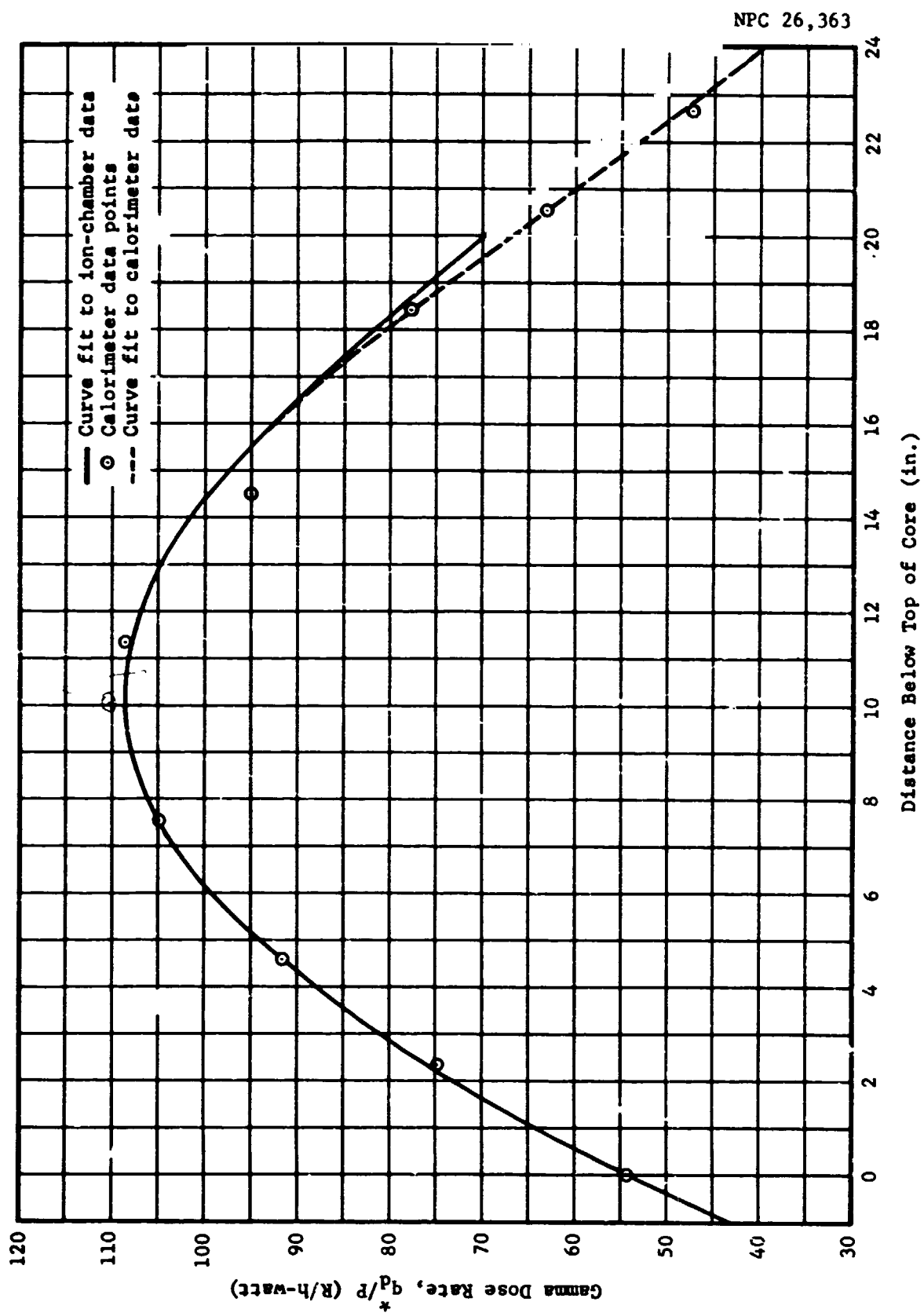


Figure 18 Final Gamma-Dose-Rate Profile for the ASTR Core

Figure 18, and the data points for the calorimeter (Table 10) are plotted on this figure for comparison. The ion-chamber curve is observed to duplicate the dashed curve fit of Figure 17 for the calorimeter (which does not include the 14.5-in. point) almost exactly out to 16 in. The fit to the calorimeter data beyond this point is shown as the dashed curve of Figure 18. Thus, agreement is obtained between independent calorimeter and ion-chamber measurements, with a slight increasing discrepancy being found toward the full-down position.

As the calorimeter probe is traversed toward the bottom of the core, more and more of the gammas must penetrate the extra thickness of the water-cooled base before striking the probe. A rough estimate of the gamma rays attenuated by the base in the worst case (full-down position) indicates that the effective gamma flux would be reduced by about 5%. Hence, one should expect the calorimeter dose rates at the full-down position to be roughly 5% lower than the ion-chamber rates because of gamma attenuation in the base.

Now, with reasonable adjustments for position, all but two of the calorimeter data points of Figure 18 will fall on the ion-chamber curve. The low points at calorimeter positions of 14.5 and 22.6 in. were the first two measurements taken after the 1.89-MW power level was attained, and by comparing the dose rates at common positions for 1.89 MW and for 6.78 MW (Table 10), one obtains ratios of 1.08 and 1.01 for the full-up and full-down positions, respectively. If the reactor power level had not yet stabilized at 1.89 MW in the full-down ratio above, as might be indicated, and if one assumes that this ratio should have the 1.08 value of the full-up position, then the dose rate per unit reactor power at 22.6 should be raised to 50.6 R/h-W. This, then, will give a corrected full-down dose rate which is 5.5% below the ion-chamber reading, in agreement with the attenuation estimate. Applying this same correction to the 14.5-in. value yields a dose rate per unit power of 101.4 R/h-W, which agrees very well with the ion-chamber value of Figure 18.

In summary, the excellent agreement between the calorimeter and ion-chamber measurements for positions above the reactor centerline lends considerably more confidence to the ion-chamber results, which depend on a calibration in a known radiation field, but, once independently and identically calibrated in two different

ways, the continuous ion-chamber measurements are more accurate for defining the dose-rate profile through the reactor core. Thus, the first two calorimeter measurements at 14.5 and 22.6 in. are believed to be low by about 5.5%, due perhaps to a slow stabilization of reactor power at 1.89 MW, and this seems to be verified by a comparison with calorimeter data at ~ 7 MW. Once these corrections are made, the last three calorimeter measurements toward the bottom of the reactor can be brought into line with the ion-chamber curve of Figure 18 by attenuation corrections with position of from 2 to 6%.

The final dose-rate profile from combined calorimeter and ion-chamber results will then be considered to be given by the solid curve of Figure 18, and the less accurate dosimeter results to be presented in Section 5.3 will be shown to be in substantial agreement with this curve.

5.2.2 Gamma Background

Before initiating reactor operation for the dose-rate mapping, measurements of the core background level were obtained. Several continuous traverses were made in order to ensure reproducibility of results. A step-wise scan, in which the chamber was stopped every inch or so, was also made; the results of this traverse are presented in Figure 19.

The reactor core was relatively "cold" at the time (May 25) the background measurements were made, the total history consisting of less than 100 MW-h of operation. The most recent operation had been on the two previous days, May 23 and 24 (foil and dosimeter mapping), and consisted of only 5.5 kW h. The reactor had not been operated for several months prior to the mapping experiments.

5.2.3 After-Shutdown Dose Rate

Upon completion of the dose-rate measurements at 165 kW, the ion chamber was positioned 1.5 in. above the core center. The reactor was then shut down by manual scram, and the dose rate was recorded as a function of time. The results of this measurement appear in Figure 20.

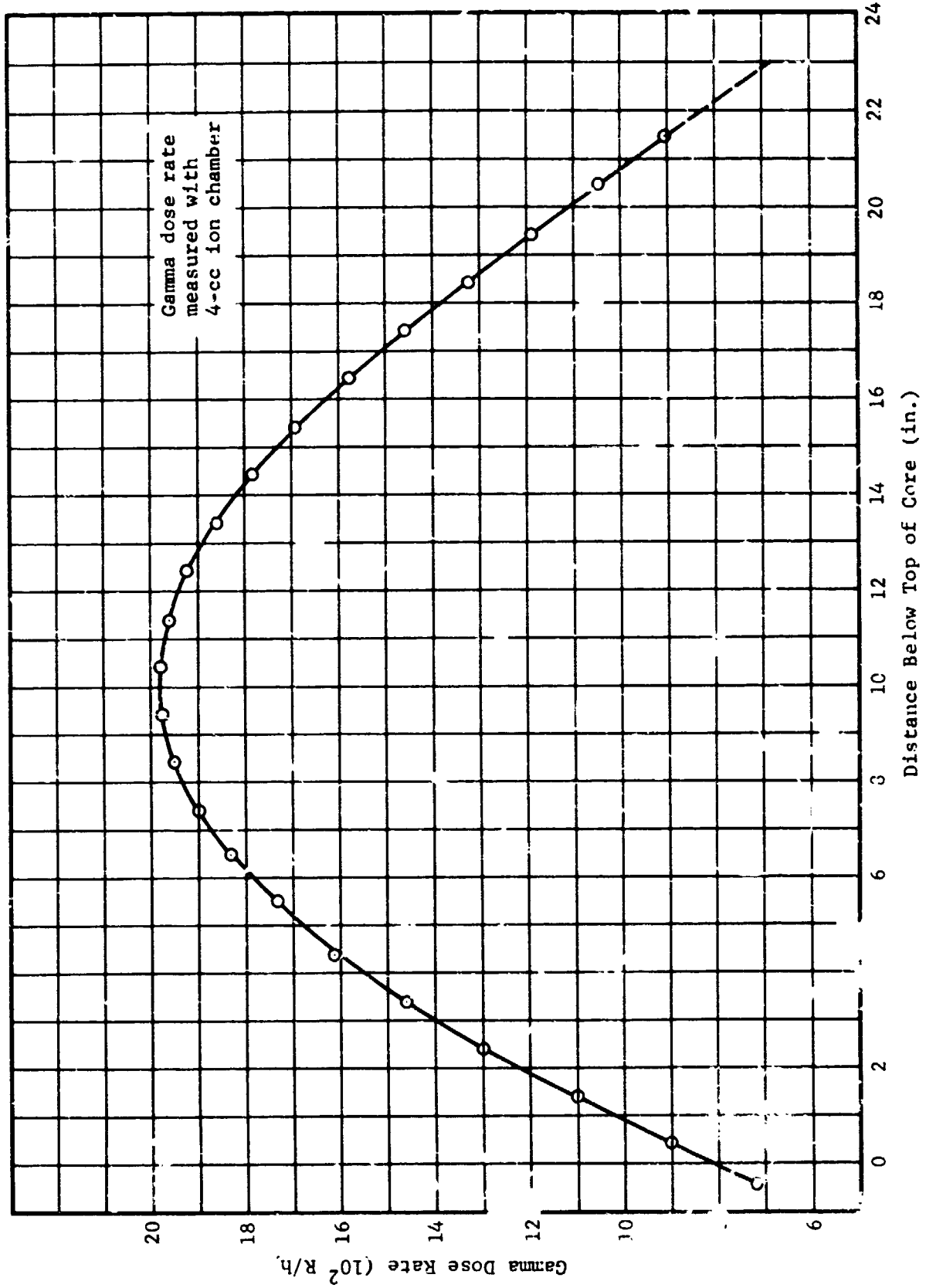


Figure 19 Background Gamma Dose Rate in the In-Pile Tube

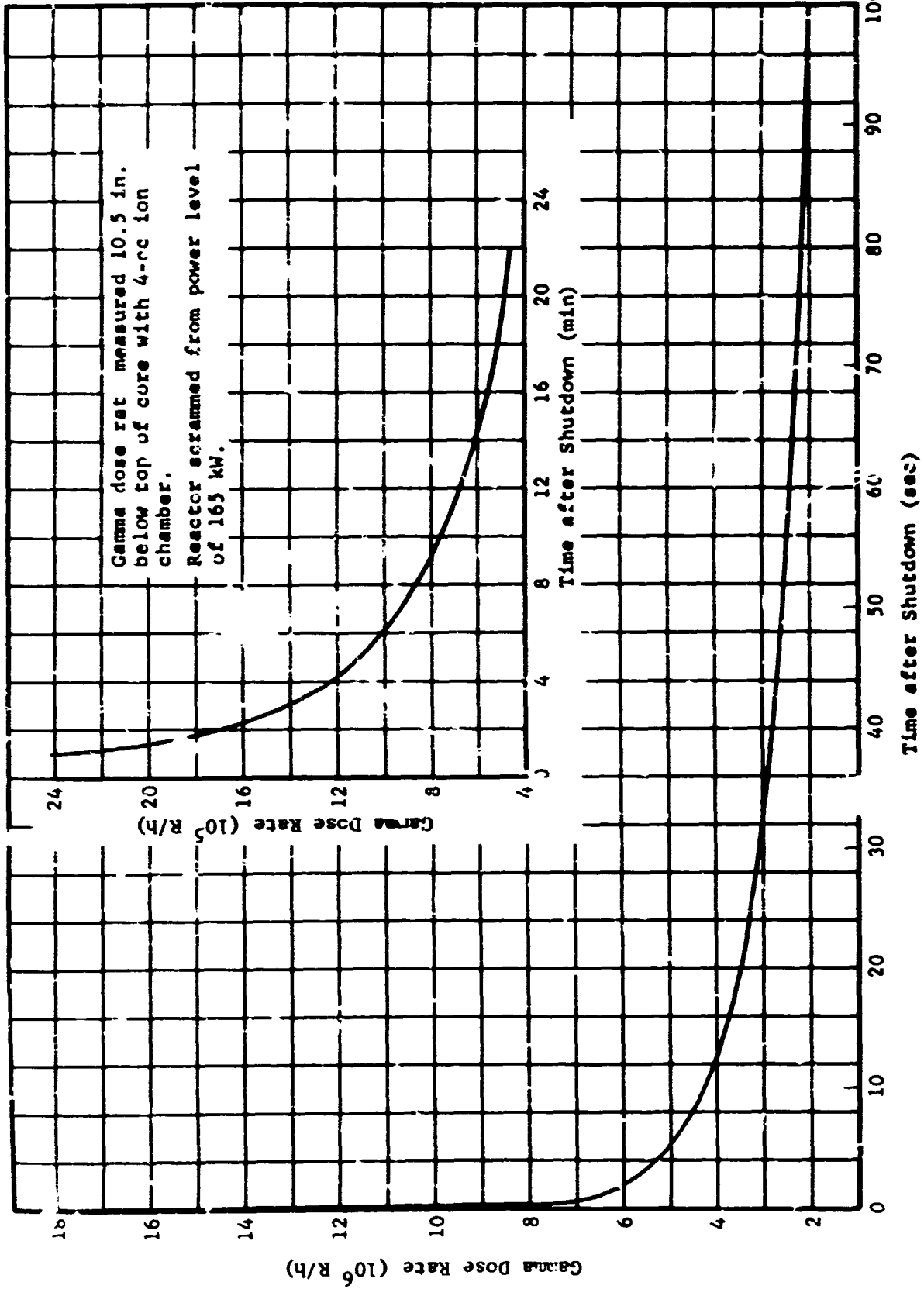


Figure 20 After-Shutdown Gamma Dose Rate in the In-Pile Tube

5.2.4 Error Analysis

The potential errors in the ion-chamber measurements and the assigned maximum percent uncertainties are as follows:

<u>Source of Error</u>	<u>Uncertainties (+%)</u>
Calibration:	
Dose Rate	3
Current	Negligible
Experiment:	
Linearity	1
Current	2
Temperature response	Negligible
Neutron response	1
Position	1
Power level	4

$$\text{One standard deviation} = \sqrt{\sum_1^2} = \pm 5.66\%$$

$$\text{Two standard deviations (95\% confidence level)} = \pm 11.3\%$$

The dose rate in the cobalt-60 irradiator is based on several independent calibrations, one of which is a comparison with an NBS standard. The error in current measurement while making the ion-chamber calibration is considered negligible because it is an average of readings taken over a three-day period.

The linearity of the type of ion chamber used in this experiment has been previously investigated by an indirect method which involved determining the voltage at which ion collection decreased below 99% and at which multiplication increased no more than 1%. The results indicated chamber linearity to dose rates well above those encountered in this experiment.

The 2% uncertainty assigned the current measurement is for the picoammeter with recorder readout and includes the linearity over a range from 10^{-10} to 10^{-5} amp.

The temperature response of the ion chamber is roughly 0.1% per °F; however, the response time is a matter of hours. The calibration temperature in the irradiator was approximately

90°F, and the temperature range in the reactor experiment was from about 80° to 100°F. Because of the small temperature range and the short time required to obtain the data, no significant error should be introduced by this factor.

The neutron response of the ion chamber constitutes a computed correction of 2.5%, which has been assigned an uncertainty of 1%.

The position of the ion chamber was indicated to the nearest 0.1 in. As discussed in Section 5.1.3, this would result in an error in dose rate of 1.6% near the extremities of the reactor core, but small error near the center of the core. The position of the ion chamber was taken to be the center of detection so that the spatial variation of the field would tend to be averaged.

At the reactor power levels used in the ion-chamber mapping, temperature rises were too small to obtain accurate heat balances. Power levels were therefore set by ion chambers calibrated in a separate 3-MW reactor operation.

5.3 Gamma Dosimeters

5.3.1 Cobalt Glass

The gamma dose in the in-pile tube was measured with cobalt-glass dosimeters in three separate irradiations. The results are tabulated in Table 12 along with gamma dose rates based on a reactor power level of 1.65 kW for a 30-min irradiation. No correction for core background has been applied to these data.

Figure 21 shows the average of all the measurements at each position plotted on the ion-chamber curve of Figure 18. While there is some scatter in the data points, the general agreement with the ion-chamber dose rates is apparent.

The dose rates with the perturbation fixture in the core (Run 6) are not appreciably different from those without the fixture. The scatter in the three measurements at each of the distances of 9.5, 14.5, and 19.5 in. is due at least in part to the normal variation encountered in multiple exposure of cobalt glass.

Table 12

GAMMA DOSE AND DOSE RATE FROM COBALT-GLASS DOSIMETERS

Position	Distance ^a (in.)	Run No.	Dose (10 ⁴ R)	Dose Rate (R/h-W)
1A	24.5	4	4.0	49
3A	19.5	4	6.2	75
5A	14.5	4	8.9	108
7A	9.5	4	8.8	107
9A	4.5	4	7.4	90
11A	-0.5	4	4.1	50
1A	24.5	5	3.6	44
3A	19.5	5	6.7	81
6A	12.0	5	8.6	104
9A	4.5	5	7.7	93
11A	-0.5	5	4.1	50
3A	19.5	6	4.7	57
3B	19.5	6	6.2	75
3D	19.5	6	6.7	81
5A	14.5	6	8.2	99
5B	14.5	6	8.7	105
5D	14.5	6	8.9	108
7A	9.5	6	8.6	104
7B	9.5	6	9.6	116
7D	9.5	6	9.4	114

^aFrom top of core

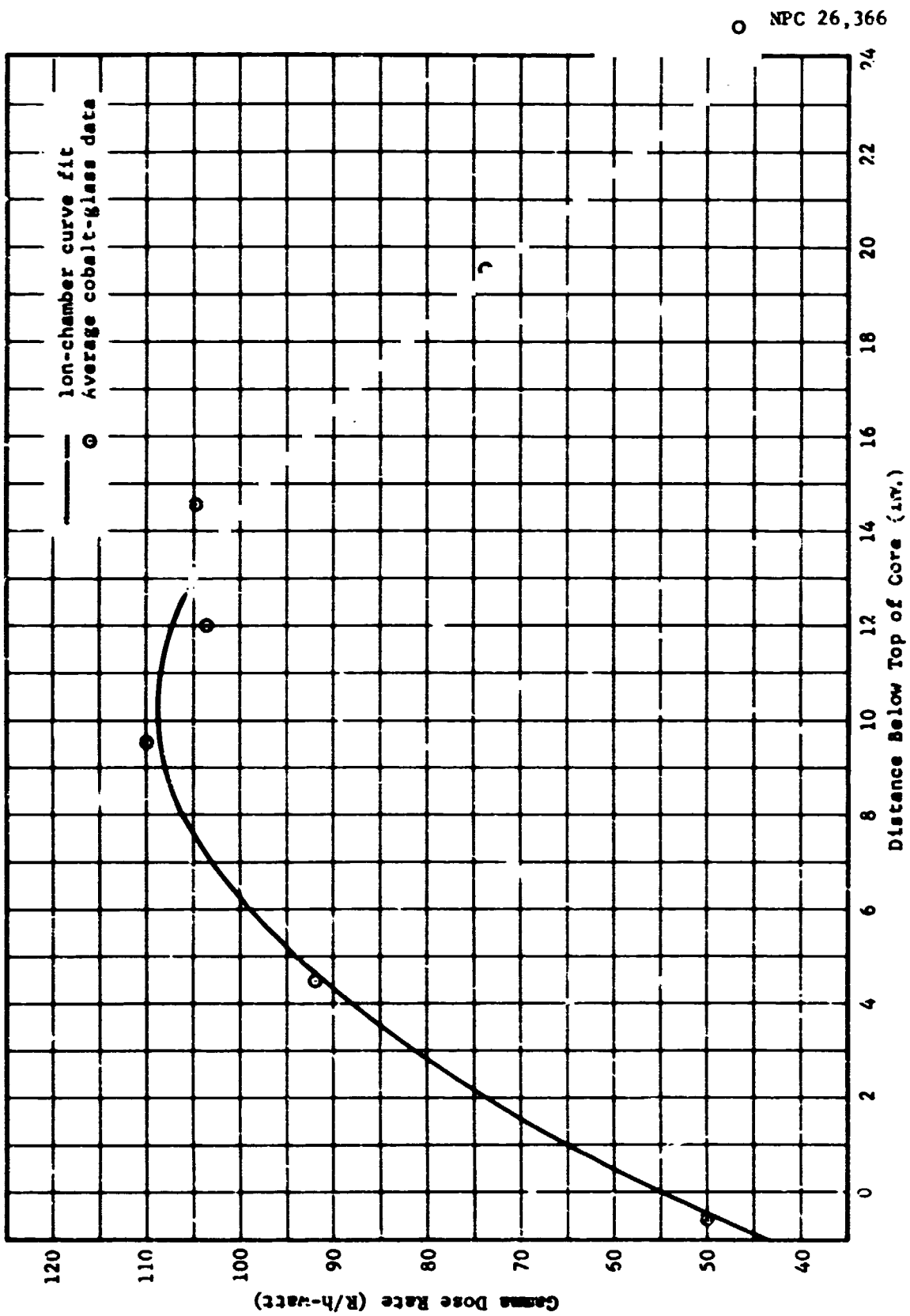


Figure 21 Gamma-Dose-Rate Profile as Determined from Cobalt-Glass Dosimeters

5.3.2 Thermoluminescent Dosimeters

Thermoluminescent dosimeters were irradiated at 45.5 W, 455 W, 1.65 kW, and 1.65 kW with the perturbation fixture (Runs 2, 3, 4, and 6). An exposure was also made at zero power in order to obtain the core background level for use in correcting the data obtained at the lowest power levels.

Table 13 and Figure 22 present a summary of the data as received from AGC. While the dose rates near the center of the in-pile tube are somewhat higher than those presented earlier, the general agreement in profile is apparent. Complete details of this and additional data will be reported by AGC (Ref. 11).

5.4 Neutron-Detecting Foils

5.4.1 Fast-Neutron Flux

The neutron flux above an energy of 2.9 MeV was measured with sulfur pellets during Runs 3, 4, 5, and 6, and the flux above 8.1 MeV was measured with aluminum foils in Runs 4, 5, and 6. The measured fluxes, in n/cm^2 -sec-W, are tabulated in Table 14; Figure 23 is a plot of the sulfur-pellet data from Run 4. The average sulfur-to-aluminum ratio is 33.9.

The sulfur-pellet data show the flux to be quite uniform across the tube except in the direction toward the center of the reactor core (Stringer D). Also, the effect of the perturbation fixture appeared to be to increase somewhat the flux measured with the sulfur. For all practical purposes, however, the difference is inconsequential.

5.4.2 Thermal-Neutron Flux

The thermal-neutron flux ($E < 0.48$ eV) was measured with copper foils in Runs 3, 4, and 6. Bare and cadmium shielded foils were placed at alternate positions (2.5 in. apart) along the center of the tube (Stringer A) and also on the perturbation fixture at positions approximately equivalent to Stringers A, B, and D. Table 15 gives the saturated activities, in disintegrations per minute-gram-watt; the averages of these data for each position are plotted in Figure 24. From the plots of bare-foil saturated activity and cadmium-covered-foil saturated activity, the cadmium-difference activity (bare-foil saturated activity

Table 13

AGC THE K. L. WYNOFF

[illegible]

^aDistance from top of core
Run 3 thermal neutron data are incorrect because of saturation of the L167

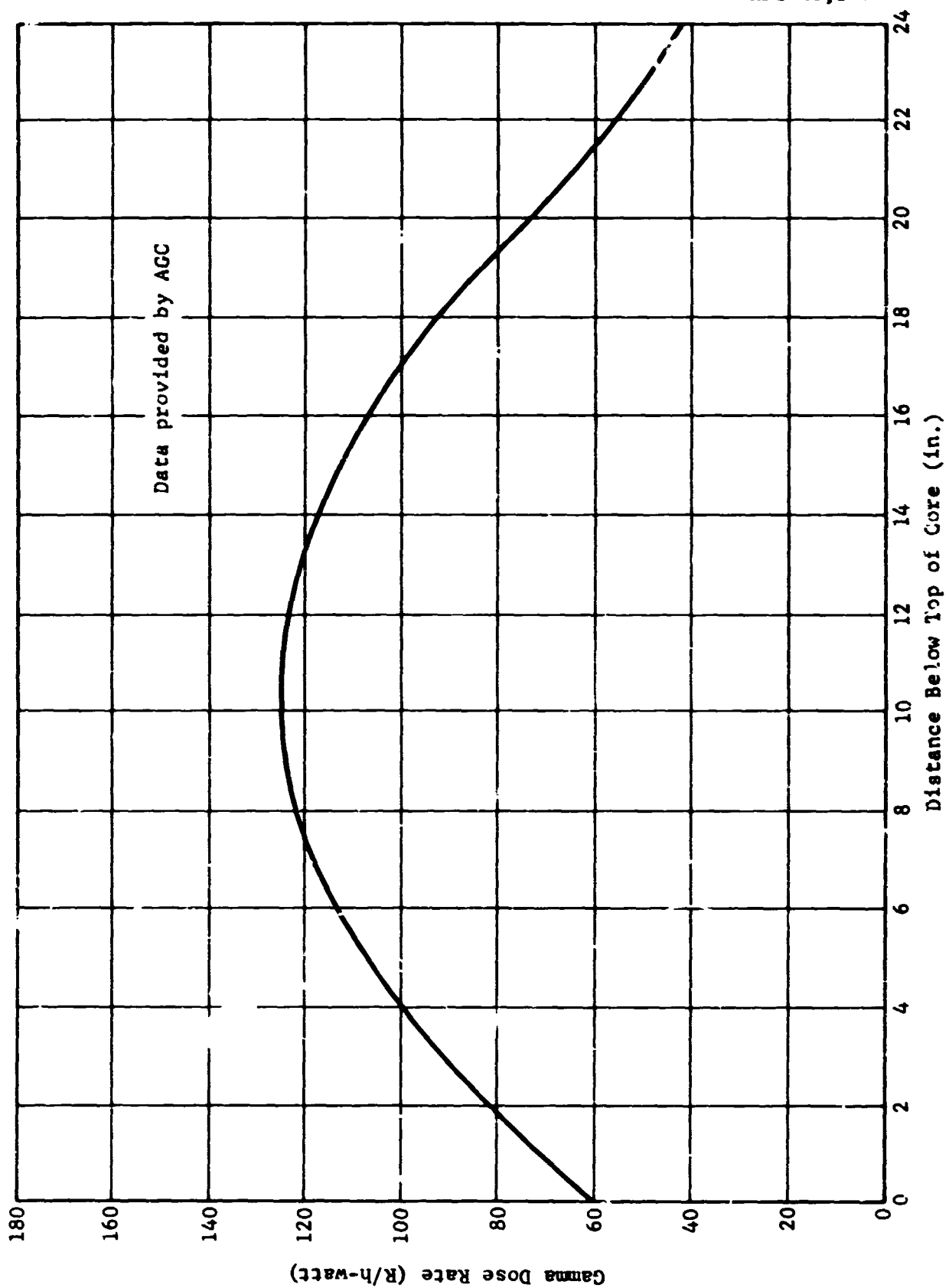


Figure 22 Gamma-Dose-Rate Profile as Determined from the Average AGC Mapping Data

Table 14

NEUTRON FLUX FROM SULFUR AND ALUMINUM DETECTORS

Position	Distance ^a (in.)	Neutron Flux (10^5 n/cm ² -sec-W)							
		Run 3		Run 4		Run 5		Run 6	
		S	Al	S	Al	S	Al	S	Al
2A	22	6.16	0.217	6.00	0.381	9.06	0.305	10.1	0.307
B			0.141	5.78	0.297			11.1	0.332
C			0.164	5.71	0.363			-	-
D			0.189	5.90	0.345			11.9	0.332
3A	19.5								
4A	17	11.2	0.381	10.7	0.451			13.0	0.367
B			0.297	10.4	-			14.0	0.392
C			0.363	10.3	0.370			-	-
D			0.345	11.5	0.379			15.0	0.430
6A	12	14.0	0.451	13.6	0.415			12.6	0.362
B			-	13.0	0.395			13.2	0.363
C			0.370	13.5	0.370			-	-
D			0.379	14.7	0.420			14.6	0.411
8A	7	13.2	0.415	12.9	0.395				
B			0.395	12.8	0.370				
C			0.370	12.7	0.420				
D			0.420	14.0					
9A	4.5					11.7	0.393		
10A	2	8.56	0.254	7.97	0.254				
B			0.245	7.94	0.245				
C			0.214	7.89	0.214				
D			0.230	8.73	0.230				

^aFrom top of core

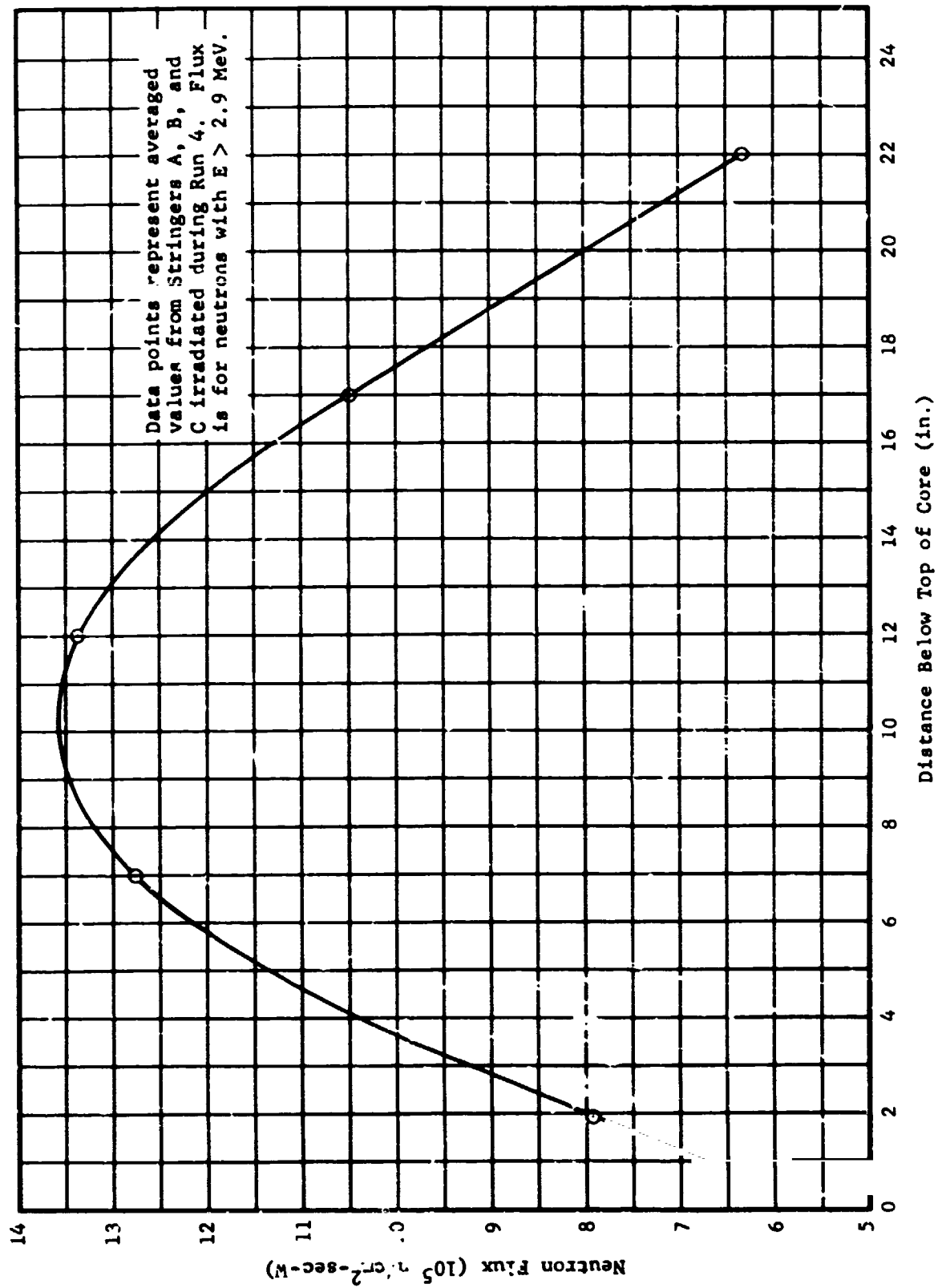


Figure 23 Fast-Neutron-Flux Profile as Determined from Sulfur-Pellet Data

Table 15
COPPER-FOIL SATURATED ACTIVITIES

Position	Distance ^a (in.)	Saturated Activity (dpm/g-W)											
		Run 3			Run 4			Run 6			Run 6		
		Stringer A	Bare	Cd	Stringer A	Bare	Cd	Stringer A	Bare	Cd	Stringer B	Bare	Stringer D
1	24.5						0.529						
2	22.0	8.51			8.06								
3	19.5		1.14				1.10			0.902			0.964
4	17.0	13.1			12.5			12.0				12.5	
5	14.5		1.56				1.47			1.26			1.46
6	12.0	14.1			16.3			15.3				15.9	
7	9.5		1.67				1.64			1.54			1.57
8	7.0	15.5			15.1			15.1				14.9	
9	4.5		1.29				1.23						
10	2.0	11.5			10.7								
11	-0.5						0.603						

^aDistance from top of core

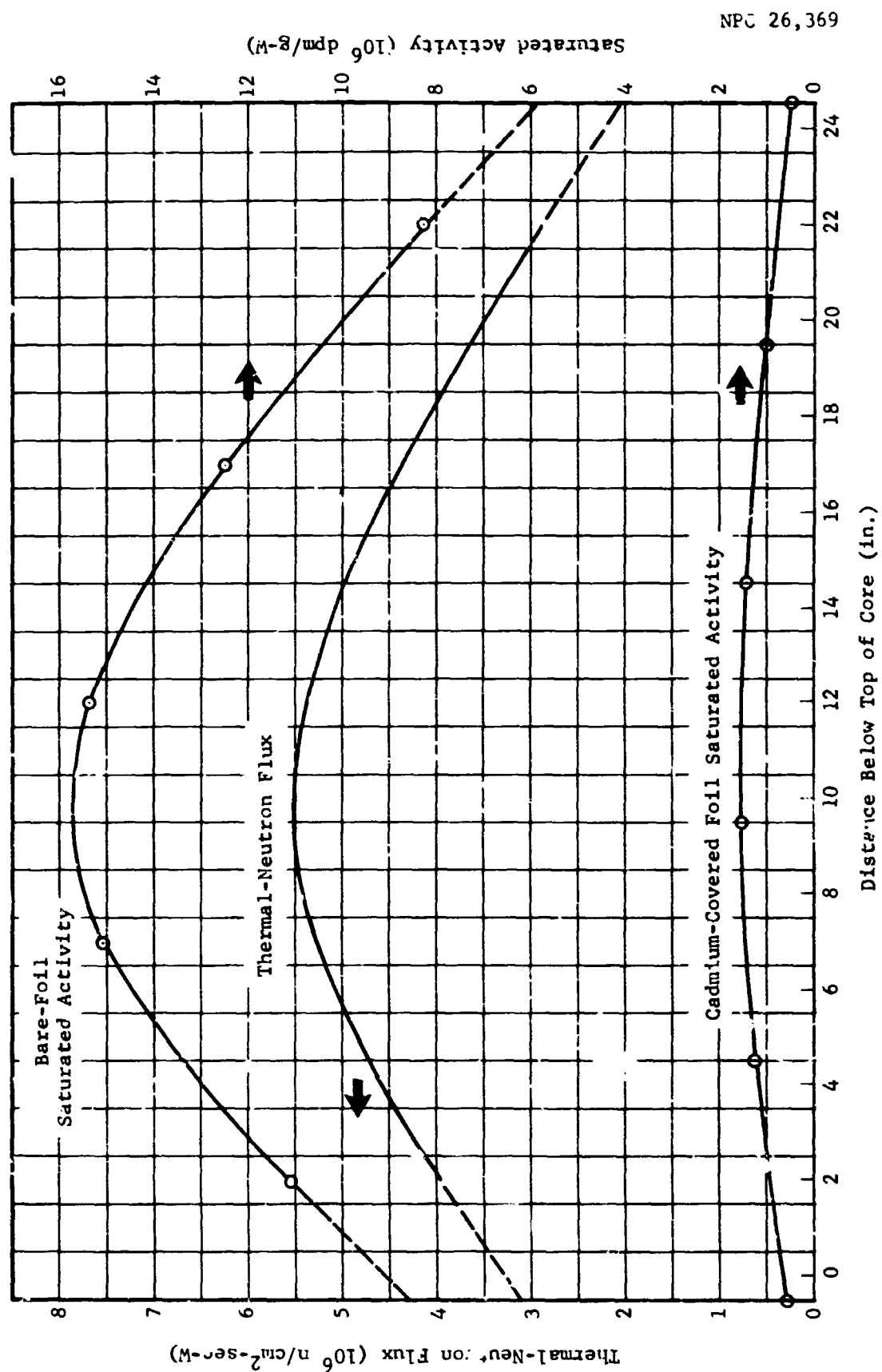


Figure 2- Thermal-Neutron-Flux Profile as Determined from Copper-Foil Data

minus cadmium-covered-foil saturated activity) is obtained as a function of position. This cadmium-difference activity converts directly to thermal-neutron flux, which is also plotted in Figure 24.

Figure 25 presents a profile of thermal-neutron flux as determined by AGC from thermoluminescent dosimeters. This technique involves the use of pairs of dosimeters, one enriched in lithium-7 and the other enriched in lithium-6; the former have a low sensitivity to neutrons while the latter have a high sensitivity to thermal neutrons. Both dosimeters have approximately the same sensitivity to gamma rays, so the lithium-7 dosimeter response is used to correct for the gamma portion of the response in the lithium-6, thereby giving that portion of response due only to thermal neutrons. A suitable calibration in a known thermal-neutron flux permits a direct conversion of dosimeter response to neutron fluence. A comparison of Figures 24 and 25 shows very close agreement of results by the two methods of measurement.

5.4.3 Neutron Spectrum

Two sets of spectral detectors (Table 4) were exposed in Run 5 for the purpose of obtaining an approximate neutron spectrum for the in-pile tube. The foil-method for specification of neutron spectra is detailed in Reference 12; the procedures and results are outlined in the following sections.

The neutron spectrum given in Figure 26 for the ASTR in-pile tube is believed to represent a fairly good first-order approximation to the true spectrum. It is emphasized that, because of the nominal amount of data obtained, the energy range below about 1 MeV is the most uncertain. Nevertheless, the given spectrum agrees with expectations in that the relative thermal-to-fast component is less than that in an extremely moderated region, e.g., water reflector, and the epithermal component has not achieved the 1/E distribution in moderation.

5.4.3.1 Thermal-Neutron Spectrum

The thermal spectrum includes that portion of the neutrons that are in equilibrium with the surrounding medium. The true differential thermal flux $\phi_M(E)$ is defined adequately in the

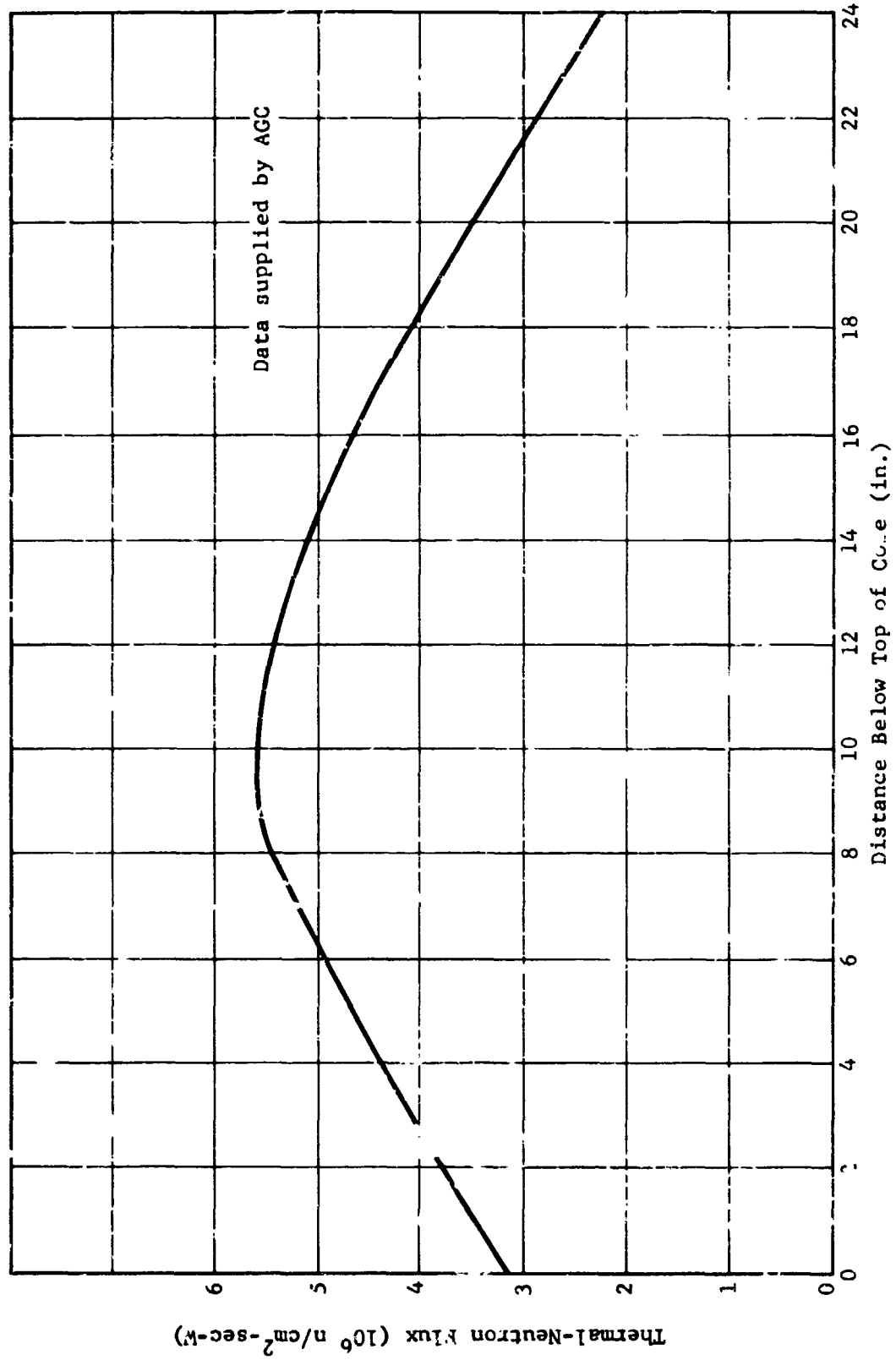


Figure 25 Thermal-Neutron-Flux Profile as Determined from the Average AGC Mapping Data

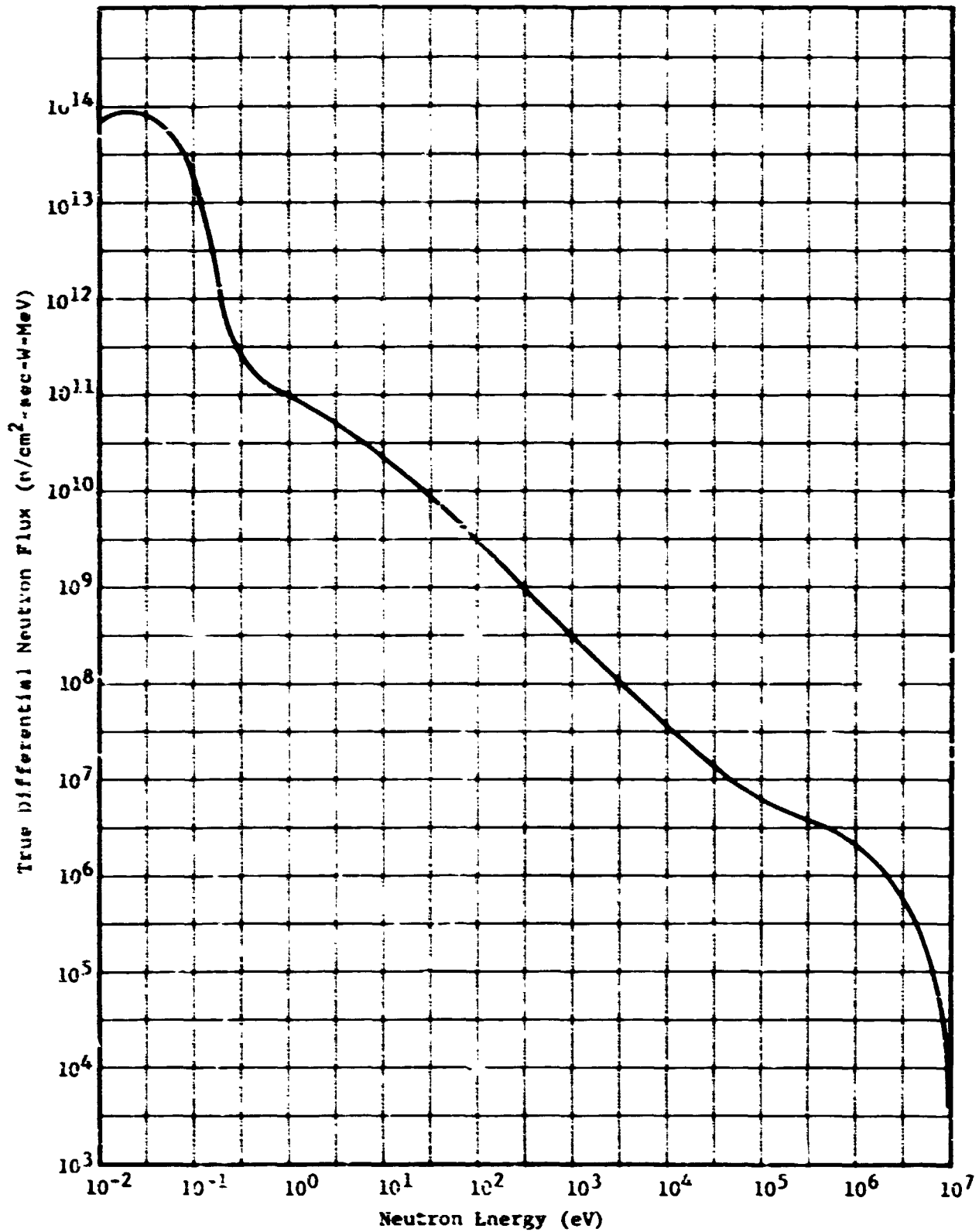


Figure 26 Approximate Neutron Spectrum in the ASTR In-Pile Tube

neutron energy range $0 \leq E \leq 5.6 E_0$ by the Maxwellian distribution function

$$f_M(E) = n_M (8/\pi E_0^3)^{1/2} E e^{-E/E_0} \quad (35)$$

where n_M is the total density of thermal neutrons and $E_0 = kT_0$ is the kinetic energy of the neutrons at the temperature T_0 °K of the distribution.

The true thermal (integrated) flux F_M is given by

$$F_M = \int_0^{\infty} f_M(E) dE \quad (36)$$

The "conventional" thermal flux (2200m/sec flux) is related to F_M by

$$\phi_M = F_M (\pi T_0/4T)^{1/2} \quad (37)$$

where $T_0 = 293.6^\circ\text{K}$.

The above relations were used to derive the thermal flux distribution of Figure 26, which is normalized so that the average integral neutron flux obtained from foil measurements at 6.5 in. above and below core centerline is 5.15×10^6 n/cm²-sec-W.

5.4.3.2 Epithermal-Neutron Spectrum

The epithermal flux includes all neutrons above thermal energies and is defined in the energy interval $5.6 E_0 \leq E \leq 10^{-3}$ MeV as the resonance flux. In thermalizing unperturbed media the resonance component commonly follows a $1/E$ distribution, and is defined in terms of a constant and the true thermal flux by the relation

$$f_r(E) = \beta F_M/E = F_{\ln E}/E \quad (38)$$

where β is the epithermal flux per unit interval of $\ln E$ per unit true thermal flux.

In terms of "measurable" quantities,

$$F_{\text{prE}} = K \phi / (CR-1)(1 + \alpha) \quad (39)$$

where $K = \frac{1}{2}(E_C/E_{2200})^{\frac{1}{2}} = 2.18$ for a Maxwellian distribution at a given temperature, CR is the cadmium ratio, and α is the ratio of the resonance to 1/V components of the epithermal cross sections of the particular foil used.

For a temperature of 303°K (reasonably close to the ASTR in-pile tube conditions) and $E_C = 0.48$ eV (for 20-mil cadmium-covered foils),

$$\beta = 1.90 / (CR-1)(1 + \alpha) \quad (40)$$

Values of β were determined from the average cadmium ratios of indium, gold, copper, and phosphorous reactions in the spectral packets. The results are given in Table 16 along with the cadmium ratios and α values.

Table 16

RESONANCE-NEUTRON SPECTRAL FUNCTIONS

Detector	Main Resonance Energy (eV)	Thin-Foil Cd Ratio	α	1/ β
Indium	1.46	5.7 \pm 10%	20.1	52.2
Gold	4.91	2.36 \pm 2%	36.2	26.6
Copper	580	14.1 \pm 5%	1.62	18.1
Phosphorus	1.58(10 ⁵)	25.0 \pm 9%	0.11	14.0

For a true $1/E$ spectrum, the values of $1/\beta$ should be equal and independent of the detector. Since the values obtained indicate that F_{1nF} is not constant but increases with increasing energy, a modified resonance spectrum was constructed from the different values of F_{1nF} obtained for the four reactions.

5.4.3.3 Fast-Neutron Spectrum

The measurement of the fast-flux spectrum by foil activation employs the use of threshold reactions: (n,p) , (n,α) , and (n,n') . An effective threshold energy E_{eff} is defined such that

$$\sigma_s \int_{E_{eff}}^{\infty} f(E) dE = \sigma_s F_{eff} = \int_{E_T}^{\infty} \sigma(E) f(E) dE \quad (41)$$

where σ_s is the saturation value of the cross section (maximum mean value); $f(E)$, the differential neutron flux; F_{eff} , the total fast flux above E_{eff} ; $\sigma(E)$, the cross section for the particular reaction at an energy E ; and E_T , the true threshold energy.

For each of the three threshold reactions used, viz., $In^{115}(n,n')$, $S^{32}(n,p)$, $Al^{27}(n,\alpha)$, a fast-flux component above the nominal effective threshold energies of 0.85, 2.9, and 8.1 MeV, respectively, is defined. For a GTR-type spectrum (Refs. 8 or 12), the ratios of the fast flux components are known and the differential flux is defined. For other than GTR-type spectra, use is made of the defining equation of threshold energy and integral flux measurements to generate the true modified spectrum.

Fortunately, the flux ratios obtained for the ASTR in-pile tube test locations verified the existence of the GTR-type spectrum in the fast region and no further iteration was required.

APPENDIX A
CALORIMETER MEASUREMENTS OF NUCLEAR
HEATING RATES

APPENDIX A

CALORIMETER MEASUREMENTS OF NUCLEAR
HEATING RATES

A-1 Steady-State Theory

Assuming that heat is produced uniformly throughout the small probe at a rate of q cal/cm³-sec, one can write the steady-state temperature equation for one-dimensional heat flow along the stem of the probe as

$$\frac{d^2T}{dx^2} = -\frac{q}{k} \quad (A-1)$$

where k is the thermal conductivity. The boundary conditions, as stated in Section 2.1.1, are

$$\begin{aligned} T(x) &= T_1 \quad \text{at } x = 0 \\ T(x) &= T_2 \quad \text{at } x = L \\ 0 &= \frac{qV'}{A} = -k \left(\frac{dT}{dx} \right)_{x=0} \end{aligned} \quad (A-2)$$

The general solution to Equation A-1 is given by

$$T(x) = \frac{-qx^2}{2k} + Ax + B \quad (A-3)$$

where the constants of integration, A and B , can be specified from the first two boundary conditions:

$$\begin{aligned} B &= T_1 \\ A &= \frac{T_2 - T_1}{L} + \frac{qL}{2k} \end{aligned} \quad (A-4)$$

Therefore, Equation A-3, giving the steady-state temperature at any point x between the thermocouples on the stem of the probe (Fig. 1), becomes

$$T(x) = \frac{-qx^2}{2k} + \left(\frac{T_2 - T_1}{L} + \frac{qL}{2k} \right) x + T_1 \quad (A-5)$$

Hence, the rate of change of temperature along the stem of the probe at the point x , in a direction perpendicular to the cross-sectional area A , is given by

$$\frac{dT(x)}{dx} = \frac{-qx}{k} + \frac{T_2 - T_1}{L} + \frac{qL}{2k} \quad (A-6)$$

and, according to the last boundary condition, the rate of change of temperature into volume V is

$$\left(\frac{dT}{dx} \right)_{x=0} = \frac{-qV'}{kA} = \frac{T_2 - T_1}{L} + \frac{qL}{2k} \quad (A-7)$$

so that

$$q \left(\frac{2V' + LA}{2kA} \right) = \frac{T_1 - T_2}{L} = \frac{\Delta T}{L} \quad (A-8)$$

Thus, the relationship between the heating rate in the probe and the temperature difference between the thermocouples on its stem is

$$q = \frac{2kA}{L} \frac{\Delta T}{2V' + V} \quad (A-9)$$

where $V = LA$ is the volume of that part of the cylindrical stem of length L and cross-sectional area A that lies between the thermocouples.

A-2 Transient Theory

The heat-rate input of q calories per unit volume to the large bob of the probe (Fig. 1) is divided into two components: (1) that which is stored and serves to raise the temperature of the bob, and (2) that which is conducted away through the stem

of the probe. The rate of heat storage per unit volume in the bob of the probe when its temperature increases by dT in a time interval of dt is given by

$$q(\text{gain}) = \rho C_p \frac{dT}{dt} = 0.3463 \frac{dT}{dt} \frac{\text{cal}}{\text{cm}^3\text{-sec}} \quad (\text{A-10})$$

where $C_p = 0.1278 \text{ cal/g-}^\circ\text{F}$ is the specific heat of the aluminum probe, which has a density of $\rho = 2.71 \text{ g/cm}^3$.

At the same time that this heat is being stored, the other part of the heat input to volume V' is being conducted away through the stem at a rate per unit volume of

$$q(\text{conducted}) = \frac{kA}{LV'} \Delta T = 1.222 \Delta T \times 10^{-2} \frac{\text{cal}}{\text{cm}^3\text{-sec}} \quad (\text{A-11})$$

where ΔT is the temperature differential in $^\circ\text{F}$ across the stem at time t . Therefore, the heat-balance equation for the case where heat is generated uniformly throughout volume V' of the probe at a rate of $q \text{ cal/cm}^3\text{-sec}$ is given by

$$\begin{aligned} q &= q(\text{gain}) + q(\text{conducted}) \\ &= 0.3463 \frac{dT}{dt} + 0.0122 \Delta T \end{aligned} \quad (\text{A-12})$$

Now, as it stands, Equation A-12 does not account for heat generation in the stem of the probe, but its solution will give a good approximation as to how ΔT increases with time for various uniform gamma heating rates throughout the probe.

Rearranging Equation A-12 and integrating the temperature differential between thermocouples on the stem of the probe from an initial value of ΔT_i at $t = 0$ up to a final value of ΔT_f at time t gives

$$t = 0.3463 \int_{\Delta T_i}^{\Delta T_f} \frac{d(\Delta T)}{q - 0.0122 \Delta T} = -28.34 \ln \left[\frac{q - 0.0122 \Delta T_f}{q - 0.0122 \Delta T_i} \right]$$

or

$$\exp(-t/28.34) = \frac{q - 0.0122 \Delta T_f}{q - 0.0122 \Delta T_i}$$

so that

$$\Delta T_f = 81.83 \left[q - (q - 0.0122 \Delta T_i) e^{-t/28.34} \right] \quad (A-13)$$

Now as t becomes infinitely large, one obtains the steady-state condition $\Delta T_f = 81.83$, which is independent of ΔT_i , so that if no heat were generated in stem volume V between the thermocouples one should find

$$q = \frac{\Delta T_f}{81.83} = 1.222 \Delta T_f \times 10^{-2} \text{ cal/cm}^3\text{-sec} \quad (A-14)$$

as opposed to $0.01146 \Delta T_f$ from Equation 4 (Sec. 2.1.1). If one assumes that quasi steady-state conditions are reached when t becomes large enough for the $\exp(-t/28.34)$ term in Equation A-13 to be equal to 0.01, then the time required to reach 99% of the steady-state temperature when no heat is generated in the stem would be given by

$$t = -28.34 \ln(0.01) = 131 \text{ sec} = 2.2 \text{ min} \quad (A-15)$$

Symbolically, the steady-state solution of Equation A-14 can be written as

$$q = \frac{kA}{L} \frac{\Delta T_f}{V'} \quad (A-16)$$

Comparing this to Equation 3, one sees in Figure A-1 that probe P_1 , in which heat is generated at a constant rate q in both the bob and the stem, can be replaced by probe P_2 , in which no heat is generated, and ΔT_f will be unchanged for the same heating rate if the volume of the bob V'_2 is replaced by $V'_1 + V_1/2$.

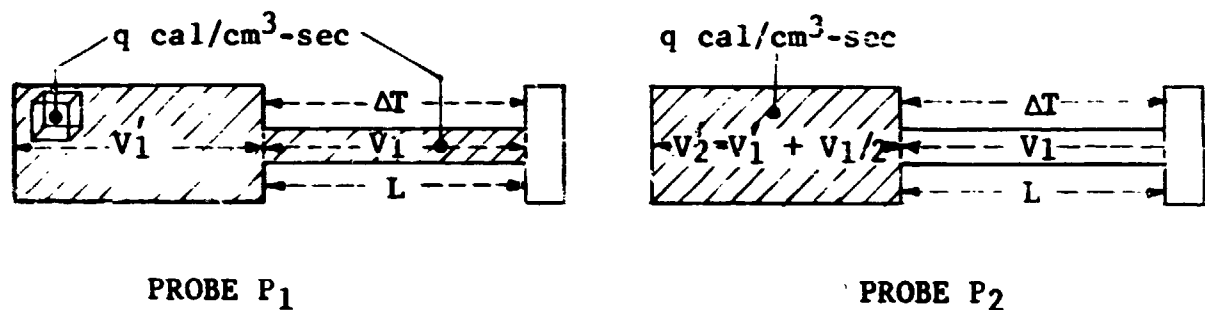


Figure A-1 Equivalent Heat Probes at Steady State

Physically, the equivalence of these probes can be made plausible by observing that heat generated uniformly in the stem of Probe 1 will, on the average, be conducted away over a stem of length $L/2$. Therefore, the entire rate of heat input to the stem, qV_1 , can be considered to be concentrated at its center. Hence, if the average path length for heat conduction is doubled in order to refer ΔT back to a standard stem of length L , then the total rate of heat input must be halved to maintain the same value for the product of the heat input and its path of flow. This balancing procedure, which requires shifting half of the heat sources concentrated at the center of the stem back into the large bob of the probe and discarding the other half, is accomplished by adding a volume of $V_1/2$ to the bob of Probe 1 and ignoring heat generation in its stem, thereby producing Probe 2.

Now by reproducing the previous solution for Probe 2, where no heat is generated in the stem, one obtains the solution for uniform heat generation throughout Probe 1 by replacing V_2 with $V' + V'/2$, where the subscripts of Probe 1 are dropped to make it agree with the notation in the main text. Hence, Equation A-12 becomes

$$q = 0.3463 \frac{dT}{dt} + 0.01146 \Delta T \quad (A-17)$$

and Equation A-13 becomes

$$\Delta T_f = 87.32 \left[q - (q - 0.01146 \Delta T_f) e^{-t/30.22} \right] \quad (A-18)$$

Thus, as $t \rightarrow \infty$, one now obtains a steady-state solution of $\Delta T_f = 87.32q$, or

$$q = 1.146 \Delta T_f \times 10^{-2} \text{ cal/cm}^3\text{-sec} \quad (A-19)$$

in agreement with Equation 4 of the text. If a quasi steady-state condition is again assumed to be reached when t of Equation A-18 becomes sufficiently large that

$$e^{-t/30.22} = 0.01 \quad (A-20)$$

then 99% of the equilibrium temperature for the case where the entire probe is being heated at a uniform rate will be attained in a time of

$$t = -30.22 \ln (0.01) = 139 \text{ sec} = 2.3 \text{ min} \quad (A-21)$$

APPENDIX B
LEAST-SQUARES CURVE FITS TO DATA

BLANK PAGE

APPENDIX B

LEAST-SQUARES CURVE FITS TO DATA

B-1 Calorimeter

The profile curves for heating rates and dose rates through the core of the ASTR were obtained from least-squares curve fits to the measured data, and coefficients were obtained for representing these curves as

$$q^*(y)/P = a_4y^4 + a_3y^3 + a_2y^2 + a_1y + a_0$$

where y is the distance into the reactor core.

The coefficients for the second-, third-, and fourth-order curve fits to the various data are listed in Table B-1, along with the standard deviations of the measured and computed values. The second and third sets of coefficients can be obtained by multiplying the first ones by constant factors of 1.064 and 410.04, respectively. The final set of coefficients gives the dose rate curve without the data point at $y = 14.5$ in., and this curve can be converted back into heating rates in aluminum and carbon by means of the constants above.

B-2 Ion Chamber

The equation for the solid curve in Figure 18, giving the dose rate per unit reactor power as a function of position y into the ASTR core, is

$$q_d^*/P = 5.9275 \times 10^{-4}y^4 - 1.8209 \times 10^{-2}y^3 - 0.3356 y^2 \\ + 10.0224 y + 54.4753$$

This equation can be evaluated to give the results in Table B-2.

Table B-1

LEAST-SQUARES COEFFICIENTS FOR HEATING AND DOSE RATES IN THE ASTR

Order of Fit	Least-Squares Coefficient					σ
	a ₄	a ₃	a ₂	a ₁	a ₀	
Heating Rate per MW in Aluminum (Curve B of Fig. 16)						
4th	1.040 (-6)	-2.608 (-5)	-1.116 (-3)	2.596 (-2)	1.304 (-1)	5.095 (-3)
3rd	0	2.109 (-5)	-1.785 (-3)	2.900 (-2)	1.281 (-1)	5.089 (-3)
2nd	0	0	-1.065 (-3)	2.279 (-2)	1.370 (-1)	8.310 (-3)
Heating Rate per MW in Carbon (Curve A of Fig. 16)						
4th	1.107 (-6)	-2.775 (-5)	-1.187 (-3)	2.762 (-2)	1.387 (-1)	5.421 (-3)
3rd	0	2.244 (-5)	-1.898 (-3)	3.086 (-2)	1.363 (-1)	5.415 (-3)
2nd	0	0	-1.133 (-3)	2.425 (-2)	1.458 (-1)	8.842 (-3)
Dose Rate per Watt (Solid Curve of Fig. 17)						
4th	4.264 (-4)	-1.069 (-2)	-4.576 (-1)	1.064 (1)	5.347 (1)	2.089 (0)
3rd	0	8.648 (-3)	-7.315 (-1)	1.189 (1)	5.253 (1)	2.087 (0)
2nd	0	0	-4.367 (-1)	9.345 (0)	5.617 (1)	3.407 (0)
Dose Rate Omitting One Point (Dashed Curve of Fig. 17)						
4th	7.110 (-4)	-2.521 (-2)	-2.300 (-1)	9.636 (0)	5.408 (1)	5.117 (-1)
3rd	0	3.209 (-3)	-5.814 (1)	1.102 (1)	5.322 (1)	1.271 (0)
2nd	0	0	-4.855 (-1)	1.033 (1)	5.400 (1)	1.338 (0)

Table B-2

DOSE RATES THROUGH THE ASTR CORE

y	q_d^*/P	y	q_d^*/P	y	q_d^*/P
0.5	59.40	8.5	107.33	16.5	90.61
1.0	64.14	9.0	108.11	17.0	87.90
1.5	68.70	9.5	108.61	17.5	85.08
2.0	73.04	10.0	108.85	18.0	82.16
2.5	77.17	10.5	108.83	18.5	79.16
3.0	81.08	11.0	108.55	19.0	76.09
3.5	84.75	11.5	108.02	19.5	72.98
4.0	88.18	12.0	107.24	20.0	69.84
4.5	91.36	12.5	106.22	20.5	66.70
5.0	94.29	13.0	104.97	21.0	63.58
5.5	96.96	13.5	103.50	21.5	60.50
6.0	99.36	14.0	101.81	22.0	57.49
6.5	101.50	14.5	99.92	22.5	54.57
7.0	103.36	15.0	97.85	23.0	51.77
7.5	104.96	15.5	95.59	23.5	49.11
8.0	106.28	16.0	93.17	24.0	46.63

APPENDIX C
ION-CHAMBER DATA

APPENDIX C

ION-CHAMBER DATA

Tables C-1 and C-2 contain the ion-chamber data used to construct the dose-rate profile through the in-pile tube. Since the rapid rate of traverse introduced an apparent shift of detector position of about 0.5 in., the traverses in opposite directions were treated separately in fitting coefficients to fourth-degree equations; these coefficients were then averaged to give the coefficients used to generate the curve of Figure 18. Appendix B contains the equation generated from these data.

Table C-1

GAMMA DOSE RATES MEASURED WITH THE ION CHAMBER,
TOP-TO-BOTTOM TRAVERSES

Distance ^a	Dose Rate (R/h-W)				
	16.5 kW	33 kW	91.1 kW	122 kW	Average
-0.4	51.1	53.0	54.7	53.2	53.0
0.4	58.2	57.7	60.3	59.8	59.0
1.4	67.8	65.4	69.6	69.7	68.1
2.4	77.7	75.1	78.7	77.9	77.3
3.4	85.7	83.3	86.7	85.7	85.3
4.4	92.2	90.4	93.4	92.2	92.0
5.4	97.9	96.1	98.7	98.0	97.7
6.4	102.5	100.5	103.0	102.8	102.2
7.4	105.9	104.3	106.7	106.6	105.7
8.4	108.2	107.1	109.4	108.8	108.7
9.4	109.7	108.7	110.7	110.7	110.0
10.4	110.5	109.6	111.0	111.6	110.7
11.4	110.2	109.8	111.0	111.3	110.6
12.4	108.5	109.4	110.5	110.6	109.8
13.4	106.6	107.6	108.3	108.1	107.7
14.4	103.1	105.1	105.1	104.9	104.5
15.4	99.1	101.4	99.8	101.6	100.5
16.4	94.2	96.1	95.0	96.2	95.4
17.4	88.7	90.6	90.2	90.2	89.9
18.4	82.2	83.9	84.1	84.0	83.5
19.4	75.4	77.3	76.8	77.7	76.8
20.4	68.4	71.1	70.4	69.9	70.0
21.4	61.1	63.6	63.5	63.1	62.8
21.9	58.2	59.4	61.1	61.3	60.6

^aFrom top of core

Table C-2

**GAMMA DOSE RATES MEASURED WITH THE
ION CHAMBER, BOTTOM-TO-TOP TRAVERSES**

Distance ^a (in.)	Dose Rate (R/h-W)					
	16.5 kW	33 kW	91.1 kW	122 kW	165 kW	Average
-0.4	51.8	51.7	54.2	53.2	51.3	52.4
0.4	58.9	60.8	60.7	60.7	56.7	59.6
1.4	68.9	69.8	70.8	70.1	65.7	69.1
2.4	78.1	80.4	80.2	79.7	75.1	78.7
3.4	86.2	88.4	88.8	88.6	84.2	87.2
4.4	94.4	95.4	95.7	97.4	92.1	95.0
5.4	100.1	101.8	103.2	103.0	98.5	101.3
6.4	105.0	106.7	107.7	107.5	103.8	106.0
7.4	108.2	110.0	111.1	109.9	107.5	109.3
8.4	110.9	111.8	113.3	113.0	110.2	111.8
9.4	111.2	112.2	114.4	113.5	110.5	112.4
10.4	110.5	111.3	112.2	113.0	110.5	111.5
11.4	109.0	109.8	112.2	111.2	109.4	110.3
12.4	106.5	107.1	110.0	108.8	107.5	108.0
13.4	103.8	103.8	108.0	106.0	104.5	105.2
14.4	100.1	99.0	104.3	104.2	101.0	101.7
15.4	96.0	94.3	98.9	98.0	97.2	96.9
16.4	90.5	89.7	94.1	92.6	92.5	91.9
17.4	86.0	84.4	88.2	87.6	86.3	86.5
18.4	80.1	78.4	82.3	82.1	79.2	80.4
19.4	73.6	72.9	76.2	75.7	73.6	74.4
20.4	67.0	67.4	69.5	68.7	67.0	67.9
21.4	61.9	62.1	62.8	62.1	60.1	61.8
21.9	58.2	59.2	61.5	59.9	57.6	59.3

^aFrom top of core

BLANK PAGE

REFERENCES

1. J. H. Lewis and J. S. Kunselman, NERVA Irradiation Program, ASTR In-Pile Tube Test 1: Pressure Transducers, GD Fort Worth Division Report FZK-344 (to be published).
2. R. W. Powell, C. Y. Ho, and P. E. Liley, Thermal Conductivity of Selected Materials, National Bureau of Standards Report NSRDS-NB58, November 1966.
3. C. G. Hogg, Gamma-Ray Dosage Rate Measurement, Idaho Nuclear Corporation Report IDO-16205, November 1954.
4. W. E. Austin, H. H. Nichols, and T. W. Ponder, Effect of Nuclear Radiation on Materials at Cryogenic Temperatures, Quarterly Progress Report 3, January 1961-March 1961, Lockheed Nuclear Products Report NR-122 pp. 85-94.
5. E. G. Bylander, "Ion-Chamber Response in High-Level Radiation Field," Nucleonics, Vol. 18, No. 5, 1960, pp. 102-104.
6. J. R. Bell and J. K. Miles, Calibration of Foils for Neutron Flux Measurements, Convair Fort Worth Report MR-N-279 (NARF-61-18T), 6 June 1961.
7. W. E. Dungan and J. H. Lewis, Nuclear Measurement Techniques for Radiation-Effects Environmental Testing, General Dynamics/Fort Worth Report FZK-9-175 (NARF-62-4T), 31 March 1962.
8. W. E. Dungan, J. K. Miles, and J. R. Bell, Developmental Studies and Reliability Control in Nuclear Techniques for Radiation-Effects Environmental Testing, Air Force Weapons Laboratory Report AFWL-TR-66-14 (FZK-276), August 1966.
9. J. D. Kington and R. K. Abele, "New Ion Chambers for Gamma-Ray Dose Measurements," Applied Physics Annual Progress Report for the Period Ending September 1, 1957, ORNL-2390, 1958.
10. H. Shenker, et al., Reference Tables for Thermocouples, U. S. Department of Commerce, National Bureau of Standards Circular 561, 27 April 1955.

REFERENCES (cont'd)

11. E. A. Warman and N. A. Hertelendy, Radiation Mapping of the ASTR In-Pile Irradiation Facility with Thermoluminescent Dosimetry, Aerojet-General Corporation Report RN-TM-0556 (to be published).
12. J. Romanko and W. E. Dungan, "Specification and Measurement of Reactor Neutron Spectra," Neutron Dosimetry, Vol. I, IAEA (Vienna, 1963).

BIBLIOGRAPHY

- Austin, W. E., et al., Effect of Nuclear Radiation on Materials at Cryogenic Temperatures, Quarterly Progress Report 1, December 1959-September 1960, Lockheed Nuclear Products Report NR-115, pp. 303-308; Quarterly Progress Report 2, October 1960-December 1960, NR-118, pp. 85-87; Quarterly Progress Report 3, January 1961-March 1961, NR-122, pp. 85-94; Quarterly Progress Report 4, April 1961-June 1961, NR-126, pp. 52-57.
- Azary, Z. P., et al., TCC Control Systems, Transducer Evaluation and Calorimetric Detector Development, EG&G Report S-245-R, March 1964.
- Burwell, D. L., Nuclear Heating Measurement Accuracy, Westinghouse Astronuclear Laboratory Report WANL-TME-1627, June 1967.
- Gunn, S. R., "Radiometric Calorimetry: A Review," Nuclear Instruments and Methods, Vol. 29, 1964, pp. 1-24.
- Herbst, D. A., and Talboy, J. H., A Steady-State Differential Calorimeter Used to Measure Gamma Heating in a Reactor Environment, Argonne National Laboratory Report ANL-7178, March 1966.
- Hogg, C. H., Gamma Heating Measurements in the MTR, Idaho Nuclear Corporation Report IDO-16093, September 1963.
- , Gamma-Ray Dosage Rate Measurement, Idaho Nuclear Corporation Report IDO-16205, November 1954.
- Weher, L. D., and Hogg, C. H., MTR Gamma Heat Generation Measurements, Idaho Nuclear Corporation Report IDO-16652, May 1961.